PERIODIC FLOW PHYSICS IN POROUS MEDIA OF REGENERATIVE CRYOCOOLERS

A Dissertation
Presented to
The Academic Faculty

by

Mihir Gaurang Pathak

In Partial Fulfillment
of the Requirements for the Degree
Doctor of Philosophy in the
School of Mechanical Engineering

Georgia Institute of Technology
August 2013

PERIODIC FLOW PHYSICS IN POROUS MEDIA OF REGENERATIVE CRYOCOOLERS

Approved by:

Dr. S. Mostafa Ghiaasiaan, Advisor
School of Mechanical Engineering
Georgia Institute of Technology

Dr. Mitchell Walker
School of Aerospace Engineering
Georgia Institute of Technology

Dr. Prateen Desai
School of Mechanical Engineering
Georgia Institute of Technology

Dr. Alan Wilhite
Aerospace Engineering
National Institute of Aerospace
Georgia Institute of Technology

Dr. Comas Haynes
School of Mechanical Engineering
Georgia Tech Research Institute
Georgia Institute of Technology

Dr. Ray Radebaugh
Cryogenics Technologies Group
National Institute of Standards and Technology

Date Approved: May 16, 2013

To my little brother, Munir Pathak

ACKNOWLEDGEMENTS

I am extremely fortunate to have worked under the guidance, mentorship, and advisement of Dr. S. Mostafa Ghiaasiaan. Professor Ghiaasiaan took a chance on me in 2009 to perform thermal physics and cryogenics research at the Georgia Tech Cryo Lab. With his guidance and support, I was able to achieve my goals and successfully complete my doctoral studies. Any future student or colleague who has the opportunity to work with Professor Ghiaasiaan is tremendously lucky. Georgia Tech and the G.W.W. School of Mechanical Engineering are very fortunate to have Dr. Ghiaasiaan as a dedicated and respected professor.

Dr. Prateen Desai, an emeritus mechanical engineering professor, has been a vital contributor to my research over the past several years, and I am thankful for having formed a lasting relationship with him. Dr. Ray Radebaugh at National Institute of Standards and Technology (NIST) deserves special thanks for his support and abundant advice, providing many solutions and new ideas to my research problems. His mentorship in cryogenic physics and cryocooler design offered a unique and unparalleled experience.

A special thank you goes to my great friend and lab partner, Mr. Tom Mulcahey. Tom and I have shared some special memories, and although times have definitely been tough for both of us, I would not trade our deep and developed friendship resulting from our stressful graduate student lives.

I have been fortunate to have great professional backing from experts in the cryogenics field. I would like to thank the Cryogenics Groups at NASA Ames Research Center (Ames), NASA/Caltech Jet Propulsion Lab (JPL), and NASA Goddard Space

Flight Center (Goddard). I want to acknowledge Dr. Bernardus Helvensteijn at NASA Ames and Atlas Scientific for guidance and the apprenticeship in experimental lab work, specifically regarding steady and periodic flow regenerator filler testing. Dr. Helvensteijn's expertise, support, and patience taught me a great deal and directly contributed to my doctoral dissertation. Thank you to Dr. Ali Kashani at NASA Ames and Atlas Scientific for his guidance, especially with experimental tests and regenerator fabrication advice. Another thank you goes to Dr. Jeff Feller at NASA Ames for his mentorship. Thank you to Dr. Jose Rodriguez at JPL for his mentorship and guidance. Another thank you goes to Dr. Eric Silk and Mr. Charles "Hudson" Delee at NASA Goddard for their support. I would also like to give special thanks to Dr. Carl Kirkconnell at Iris Technology, Dr. Ted Conrad at Raytheon, and Dr. Jeff Cha at Aerospace Corporation, along with the other GT Cryo Lab alumni. Their advice has been very helpful during my graduate tenure.

I would also like to thank my other committee members: Dr. Comas Haynes, Research Scientist at Georgia Tech Research Institute; Dr. Mitchell Walker, Professor of Aerospace Engineering; and Dr. Alan Wilhite, Professor of Aerospace Engineering, for sharing their breadth of expertise.

I am very thankful for being awarded the prestigious NASA Space Technology Research Fellowship (where "*this work was supported by a NASA Office of the Chief Technologist's Space Technology Research Fellowship"*), the Georgia Tech Presidential Fellowship, and the George W. Woodruff Presidential Fellowship. These fellowships, along with the funding provided by Professor Ghiaasiaan, enabled me to pursue and complete my graduate studies.

I also want to thank all of my graduate school friends and colleagues. We have gone through the tough Georgia Tech coursework, the stressful PhD quals, and other school requirements where we have aided each other greatly. I must also thank my mentee and undergraduate student, Mr. Vatsal Patel, who over the past year has been a tremendous help with data analysis. I also wish the best for the new students in the Georgia Tech Cryo Lab, Mr. Gilbran Alvarez and Mr. Olutobi Ogenleye. The torch is being passed to them!

Outside of research work, the support from Dr. Wayne Whiteman, mechanical engineering professor; Dr. Srinivas Garimella, mechanical engineering professor; Dr. Thomas Boston, economics professor and my minor area advisor; Ms. Glenda Johnson, advisor in the mechanical engineering department; and Ms. Segried Allen, administrative assistant in the mechanical engineering department has been incredible. Thank you all for your help over the past several years.

I must also thank the brothers of Sigma Beta Rho and my Georgia Tech and Atlanta-area friends, who have been my family during my tenure at Georgia Tech. I have felt a sense of love, compassion, and closeness, and I am very fortunate to have you all in my life.

Finally, I am extremely grateful to have the best parents in the universe, Gaurang and Sandhya Pathak. My motivation in life stems from their life stories. I dedicate my work and Georgia Tech life to them. Thank you for all the support and guidance. I am enormously appreciative for the support from my younger brother, Munir Pathak. Although younger than me, his guidance and advice is exemplary. I consider him my best friend and mentor, and thank him for all of his support and great Georgia Tech/Atlanta

and Chicago memories. A special thank you also goes to my wife, Praachi Pathak. She has been enormously helpful and a great friend. She kept my spirits high during tough and stressful times, constantly supporting me day in and day out. I look forward to our lives together outside of school! I love all of you and am very happy to have you in my life.

TABLE OF CONTENTS

LIST OF TABLES

LIST OF FIGURES

Page

NOMENCLATURE

a	Flow pulsation amplitude
a_f	Solid-fluid specific area (interfacial area concentration) [1/m^2]
A_{int}	Solid-fluid interface area [m^2]
b, C	Inertial resistance coefficient [1/m]
c_f	Forchheimer coefficient
c_P	Fluid specific heat [J/kg-K]
d	Diameter of regenerator [m]
D	Cylinder diameter [m]
D_h	Cylinder hydraulic diameter [m]
D_T	Thermal dispersion [W/m^2]
D_T^*	Dimensionless cell-average thermal dispersion [defined in Eq. (2.14)]
$\vec{n}$	Unit normal vector oriented outward from fluid side [m^2]
$\vec{n}$	Volume-average unit cell temperature gradient [W/m]
e	Fluid total specific energy per unit volume [J/m^3]
f	Pulsation frequency [Hz]
G_1, G_2	Integration constant

h	Specific enthalpy [J/kg]
h	Convective heat transfer coefficient [W/m^2-K]
$\bar{h}$	Cycle-average and unit cell-average heat transfer coefficient [W/m^2-K]
H	Unit cell lateral dimension [m]
H/L	Unit cell aspect ratio
$\bar{\bar{I}}$	Unit identity tensor
k	Fluid thermal conductivity [W/m-K]
K	Darcy permeability coefficient [m^2]
L	Unit cell longitudinal dimension [m]
n	Component of the unit vector
Nu_K	Permeability-based Nusselt number [defined in Eq. (4.13)]
Nu_L	Unit cell length-based Nusselt number [defined in Eq. (4.14)]
$Nu_{L,computational}$	Simulation-based cycle-average Nusselt number
$Nu_{L,correlation}$	Correlation-based cycle-average Nusselt number
$\dot{m}$	Mass flow rate [kg/s]
P	Static fluid pressure [N/m^2]
Re_K	Pore- or permeability-based Reynolds number [defined in Eq. (2.13)]
Re_L	Unit cell length-based Reynolds number
t	Time [s]

T	Temperature [K]
$\langle T \rangle^f$	Volume-average fluid temperature [K]
$\langle T \rangle^s$	Unit cell-average solid surface temperature [K]
U	Velocity [m/s]
$\vec{u}$	Local instantaneous velocity, volume average intrinsic velocity [m/s]
$\left\langle \vec{u} \right\rangle$	Volume-average fluid velocity [m/s]
U_{in}	Inlet velocity [m/s]
U_m	Mean fluid velocity [m/s]
$U_{\max}$	Unit cell average maximum velocity [m/s]
V	Volume [m^3]

Greek Characters

$\bar{\bar{\beta}}$	Viscous resistance permeability tensors [m^2]
ε	Porosity
η_s	Solid tortuosity
μ	Fluid dynamic viscosity [kg/m-s]
ν	Fluid kinematic viscosity [m^2/s]

θ	Macroscopic flow angle
ρ	Fluid density [kg/m^3]
ϕ	Fluid property
$\tilde{\phi}$	Spatial deviation of fluid property
σ	Uncertainty
$\bar{\bar{\tau}}$	Stress tensors
φ	Phase angle [rad]
ω	Angular frequency [rad/s]
∇	Gradient operator

Super/Subscripts

axial	Axial direction
disp	Dispersion
f	Fluid
i	1,2
in	Inlet location
j	Direction
L	Unit cell length
max	Maximum

n	1
out	Outlet location
s	Solid
T`	Transpose

Other Notation

$\langle\ \rangle$	Volume average quantity
$\langle\ \rangle^f$	Fluid volume average quantity
$\lvert\ \rvert$	Magnitude (absolute value) of the quantity
CHX	Cold heat exchanger
HX1	Compressor side warm heat exchanger
HX2	Buffer volume side compressor heat exchanger
P_1	Regenerator inlet pressure measurement location
P_2	Regenerator outlet pressure measurement location

Abbreviations

CFD	Computational fluid dynamics

UDF	User defined function

SUMMARY

Pulse tube cryocoolers (PTCs) are a class of rugged and high-endurance refrigeration systems that operate without moving parts at their low temperature ends, and are capable of reaching temperatures down to and below 123 K. These devices can also be configured in multiple stages to reach temperatures below 4 K. PTCs are particularly suitable for applications in space, guiding systems, cryosurgery, medicine preservation, superconducting electronics, magnetic resonance imaging, weather observation, and liquefaction of gases. Applications of these cryocoolers span across many industries including defense, aerospace, biomedical, energy, and high tech. Although various designs of PTCs have been in use for a few decades, they represent a dynamic and developmental field. Intense research competition is underway worldwide, and newer designs are continuously introduced. Some of the fundamental processes that are responsible for their performance are at best not fully understood, however, and consequently systematic modeling of PTC systems is difficult. Among the challenges facing the PTC research community include the improvement of overall system efficiency, which is a direct function of the regenerator component performance.

The operating characteristics of a PTC are significantly different from the conventional refrigeration cycles. A PTC implements the theory of oscillatory compression and expansion of the gas within a closed volume to achieve desired refrigeration. Regenerators and pulse tubes are often viewed as the two most complex and essential components in cryocoolers. An important deficiency with respect to the state of art models dealing with PTCs is the limited understanding of the hydrodynamic

and thermal transport parameters associated with periodic flow of a cryogenic fluid in micro-porous structures. This is particularly troubling with regards to the regenerator, where friction and thermal non-equilibrium between the fluid and the structure play crucial roles. While limited studies dealing with friction have been performed, little has been achieved with respect to the potential thermal non-equilibrium issue primarily because of the difficulty of experimental measurements. This investigation attempts to quantitatively and qualitatively determine the friction associated hydrodynamic resistance parameters, namely the Darcy permeability and Forchheimer inertial terms.

In view of the above, the goals of this investigation include: 1) experimentally measuring and correlating the steady and periodic flow Darcy permeability and Forchheimer's inertial hydrodynamic parameters for available rare-Earth ErPr regenerator filler; 2) employing a CFD-assisted methodology for the unambiguous quantification of the Darcy permeability and Forchheimer's inertial hydrodynamic parameters, based on experimentally-measured steady and periodic flow pressure drops in porous structures representing recently-developed regenerator fillers; and 3) performing a direct numerical pore-level investigation for steady and periodic flows in a generic porous medium in order to elucidate the flow and transport processes, and quantify the solid-fluid hydrodynamic and heat transfer parameters.

For the regenerator filler study, experiments were conducted in which steady and oscillatory flows of helium were imposed on $Er_{50}Pr_{50}$ rare-Earth regenerator filler material and mass flow and pressure drop data were recorded under ambient temperature conditions. A filler material composed of 63 to 75 μm diameter $Er_{50}Pr_{50}$ spheres was used based on currently available particle geometries. The flow parameters in the experiments were in the laminar flow range. A computational fluid dynamic (CFD)-assisted method

was applied for the analysis and interpretation of the experimental data, with sinusoidal time variations of inlet and exit boundary conditions for the periodic flow cases. The permeability and inertial coefficients that led to agreement between the experimental data and computational simulations were iteratively obtained. A constant permeability value for all steady and periodic flow tests was found to correlate well to experimental data. The Forchheimer inertial coefficients were correlated and found to be functions of the system charge pressure and the pore-based Reynolds number. The results also show that the periodic flow inertial coefficients are different than the corresponding steady flow parameters.

In the pore level numerical investigation, the hydrodynamic and thermal energy transport phenomena of steady and periodic flows through porous media were studied. Two-dimensional flows in porous media composed of periodically configured arrays of square cylinders was simulated using a computational fluid dynamics tool, with sinusoidal time variation of inlet and exit boundaries and conjugate heat transfer between the solid and fluid domains. Detailed numerical data were obtained for frequencies of 0 ~ 60 Hz and low and high flow amplitudes, for a 75% porous domain. Pore-scale volume-average Darcy permeability, Forchheimer coefficient, and Nusselt number associated with the standard volume-average porous media momentum, and thermal energy equations were quantified and were found to be significantly different for steady and oscillatory flows.

CHAPTER 1

INTRODUCTION

1.1 Introductory Remarks and Objectives

Cryogenics is the study of low temperature physics. The commonly-accepted cryogenic temperature range is below 123 K, down to absolute zero, 0 K, or the lowest theoretically attainable temperature. In engineering, cryogenics is best described as applications that operate in these temperature ranges.

A particular type of cryogenic engineering application is a cryocooler, which is utilized for removing heat loads at very low temperatures and hence thermally managing the overall system that the cryocooler is employed on. Although there are several types of cryocoolers, pulse tube cryocoolers (PTCs) are unique due to their mechanical simplicity and robust nature. They belong to a class of rugged and high-endurance refrigeration systems that operate without moving parts at their cold end, and are capable of easily reaching cryogenic temperatures (below 123 K). These devices can also be configured in multiple stages to efficiently reach temperatures below 20 K. PTCs are particularly suitable for applications in space, missile guiding systems, cryosurgery, superconducting electronics, magnetic resonance imaging, liquefaction of nitrogen, and liquid nitrogen transportation. Space cryocoolers are employed on rockets, shuttles, satellites, telescopes, and on other space science and exploration experiments/missions such as NASA's Mars Curiosity Rover, Compact Reconnaissance Imaging Spectrometer for Mars (CRISM), Mercury Messenger, and High Resolution Dynamics Limb Sounder (HIRDLS) missions. Cryocoolers are also used on tactical defense and commercial applications including many high performance electronic devices such as infrared focal plane arrays and

superconducting quantum interference devices (SQUIDS). Other common applications include the cooling of superconducting magnets of Magnetic Resonance Imaging (MRI) systems, gas liquefaction, and cryopumps for semiconductor fabrication. These devices greatly benefit from the associated cooling and therefore cryocoolers are considered to be enabling technologies which span various industries including aerospace, defense, biomedical, energy, computing, high tech, and pure science.

Although various designs of PTCs have evolved and been in use for a few decades, the field of pulse tube cryocooling represents a dynamic and developmental field. What makes PTCs particularly attractive is that they are extremely rugged since they do not have any moving parts on their cold end. This ruggedness makes PTCs particularly suitable for space technology and military applications. However historically, they have come at the price of relatively low efficiency and hence were used primarily in high-end applications. Although previous studies show PTCs as low efficiency systems compared to other available cryocoolers and hence limited in their employment, PTCs, over recent years, have now equaled or in some cases surpassed Stirling cryocoolers. This has been a result of sophisticated design codes and tools for developing PTCs, new regenerator filler material to increase overall system efficiency, employing the phenomena of staging, and using lessons learned and best practices from ongoing developments. They now have the potential of widespread use in consumer products, since sufficiently higher efficiencies can be achieved. Intense international research and development, and indeed competition, are underway in the field of pulse tube cryocoolers, as newer designs are continuously being introduced. Interestingly, despite extensive research in the past, some of the fundamental processes that are responsible for PTC performance are not fully understood, and consequently systematic modeling of PTC systems has been difficult.

PTCs belong to the regenerative class of cryocoolers, which operate in oscillatory flow. In oscillatory flow, the working fluid is periodically heated and cooled as it

undergoes small displacements over the course of a cycle. Also, a significant portion of the overall cryocooler system and particularly the most critical component, the regenerator, is essentially a porous medium charged with the working fluid which is undergoing the solid-fluid interactions as the gas oscillates in periodic flow. This flow physics phenomenon comes with countless challenges when understanding the fundamental principles behind the operation of PTCs.

Early models have primarily been lumped parameter-type, and semi-mechanistic models based on the numerical solution of relevant differential conservation equations that have been reported only in the last decade or so. Very recently, computation fluid dynamics (CFD) analyses of entire PTC systems have been successfully performed and demonstrated. Also, the advent of miniature sensors and engineering systems has now introduced a new and exciting field for the application of rugged cryocoolers. Thus, among the challenges facing the PTC research community is the possibility for miniaturization of these systems.

The generic structures of PTCs and their operation principles will be discussed in the forthcoming sections. Generally speaking, PTCs are typically composed of a compressor, heat exchangers, a regenerator, a pulse tube, one or more orifice valves or an inertance tube, and a buffer volume. The operating characteristics of a PTC are significantly different from the conventional refrigeration cycles which utilize the vapor compression cycle as described in classical thermodynamics. A PTC implements the theory of oscillatory compression and expansion of the working fluid, typically a gas, within a closed volume to achieve desired refrigeration. Regenerators and pulse tubes are often viewed as the two most complex and essential components of cryocoolers, where the regenerator is arguably the most vital cryocooler component. Their design parameters such as aspect ratios (length-to-diameter ratio), physical dimensions, pore structure, and regenerator filler materials, have a significant impact on the coolers overall performance. In the past, the selection and optimization of these design parameters have been either

empirical, or based on relatively crude lumped parameter or one-dimensional semi-mechanistic models. Recently, CFD analyses, although still limited in scope and depth, have shown that much improvement can be achieved with respect to the design and optimization of PTCs. An example to this point is the aspect ratio (length-to-diameter ratio) of various components of a PTC. Most regenerators and pulse tubes are currently designed with large aspect ratios ($L/D >> 1$), and as a result, one-dimensional models have been utilized to analyze the flow phenomena to predict the overall system performance. However, it is now recognized that certain future application may require small-aspect-ratio components, and recent CFD-based investigations have qualitatively and quantitatively shown that multi-dimensional effects can be significant for abovementioned components with small aspect ratios ($L/D < 2$).

The need for ultra-sensitive sensors in areas such as deep space research has recently created new challenges for cryocoolers. There is now much demand for large-capacity cryocoolers (over a few watts at temperatures below approximately 35 K) operating at temperature ranges of 20 K or below for defense and space applications, and consequently the major industrial players are building large scale cryocoolers to meet these high-capacity requirements. High-capacity pulse tube cryocoolers (HCPTCs) that achieve low temperatures have been a subject of intense research for some time, especially for space exploration applications. Such cryocoolers are attractive due to the mechanical benefits of PTCs and their ability to carry larger heat loads, making HCPTCs ideal for space missions relating to deep space science studies. These physically large cryocoolers require extremely large compressor input power, on the order of kilowatts, and are often accompanied by larger regenerator and pulse tube diameters. The design specifications of these large PTCs are unprecedented and the established empirical and semi-analytical methods may not be reliable for them. The aforementioned multi-dimensional flow phenomena will evidently be important. Multi-dimensional modeling is

therefore helpful to accurately analyze the complex fluid flow phenomena and predict the overall system performance for large diameter regenerators and pulse tubes.

An important deficiency with respect to the state of the art models dealing with PTCs, which applies to well-established as well as novel and forthcoming designs, is the inadequate understanding of the hydrodynamic and thermal transport parameters associated with periodic flow in micro-porous structures. This is particularly troubling with regards to the regenerator, where friction and thermal non-equilibrium between the fluid and the solid structure are detrimental to the performance of the regenerator and may thus play crucial roles. The efficiency of a regenerative cryocooler is dependent on the performance of the regenerator, which in turn depends on the thermal and hydrodynamic phenomena occurring during periodic flow operation. Little attention has been paid to this issue primarily because of the difficulty of experimental measurements.

In view of the above, the goals of this investigation include:

1. Experimentally measuring and correlating the steady and periodic flow Darcy permeability and Forchheimer's inertial hydrodynamic parameters for recently available rare-Earth ErPr regenerator fillers.
2. Employing a CFD-assisted methodology for the unambiguous quantification of the Darcy permeability and Forchheimer's inertial hydrodynamic parameters in the afore-mentioned rare-Earth regenerator fillers, based on experimentally-measured steady and periodic flow pressure drops in these porous structures.
3. Utilizing a direct numerical pore-level investigation for steady and periodic flows in a generic porous medium in order to develop an understanding about the associated flow processes, and for the unambiguous quantification of the solid-fluid hydrodynamic (Darcy permeability and Forchheimer's inertial coefficient) and heat transfer parameters.

1.2 Description of Pulse Tube Cryocoolers

Despite their apparently simple configurations, the operation of pulse tube cryocoolers involves complicated thermo-fluid processes, some of which are not well understood. [Swift (2002, [1]), Radebaugh (1999, [2]), Walker and Bingham (1994, [3])]. There are two specific types of mainstream cryocoolers – recuperative and regenerative type cryocoolers. Recuperative heat exchangers have separate channels with solid walls which split the continuously flowing hot and cold fluids, where the two fluids are usually in counter flow. Regenerative heat exchangers actually have a single flow channel which is typically composed of a porous matrix material that is subject to alternating flows of hot and cold fluids. Figure 1.1 shows schematics of both types of heat exchangers.

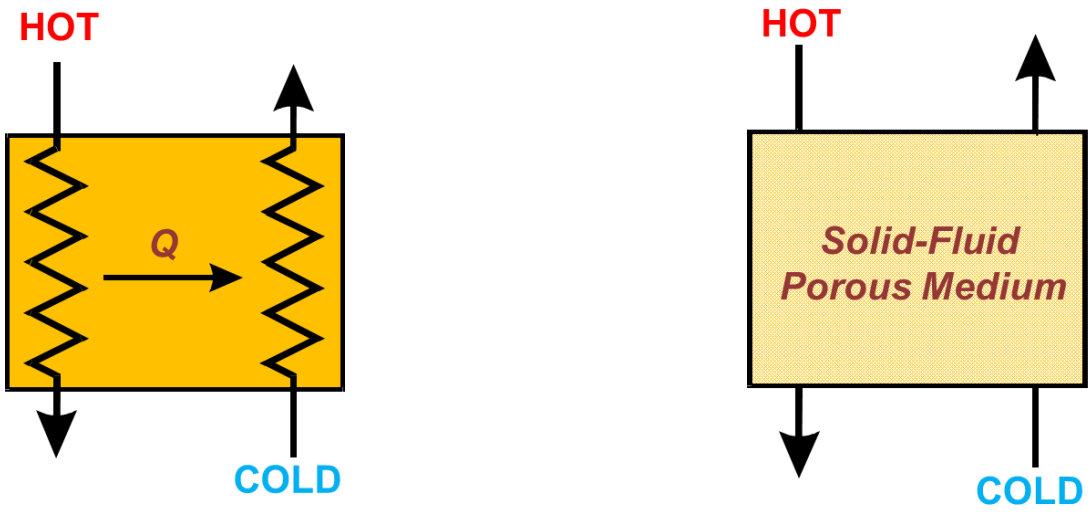

Figure 1.1. Schematic of recuperative (left) and regenerative (right) heat exchangers.

Recuperative cryocoolers operate in steady flow and examples include the Joule-Thomson, Brayton, and Claude cryocoolers. Regenerative cryocoolers, on the other hand, operate in oscillating flow and common examples include Stirling, pulse tube, and Gifford-McMahon cryocoolers. These coolers are considered modified versions of the

well-known Stirling thermodynamic cycle, where the working fluid is subject to a series of compressions and expansions in periodic flow to complete its cyclic process. Figures 1.2-1.3 show schematics of the different common cryocooler types and diagrams of the ideal Stirling cycle, respectively.

The simple Stirling system (Figure 1.2) is a configuration of piston cylinders and heat exchangers designed to provide displacement work by use of controlled heat transfer through gas expansion and compression. It consists of a power piston or compressor, a displacer piston, regenerator, and cold and warm heat exchangers. Transfer lines connect the piston assemblies to their associated heat exchangers.

The oscillating pressures and flows produced by the compressor cause cyclic changes at point locations within the system. A different branch of thermodynamics known as thermoacoustics can be employed to describe the physical processes. Using principles of acoustics as well as laws of thermodynamics, thermoacoustics provides a fundamental understanding of these time-varying phenomena associated with the Stirling cycle and other oscillatory thermal systems [Swift (2002, [1])].

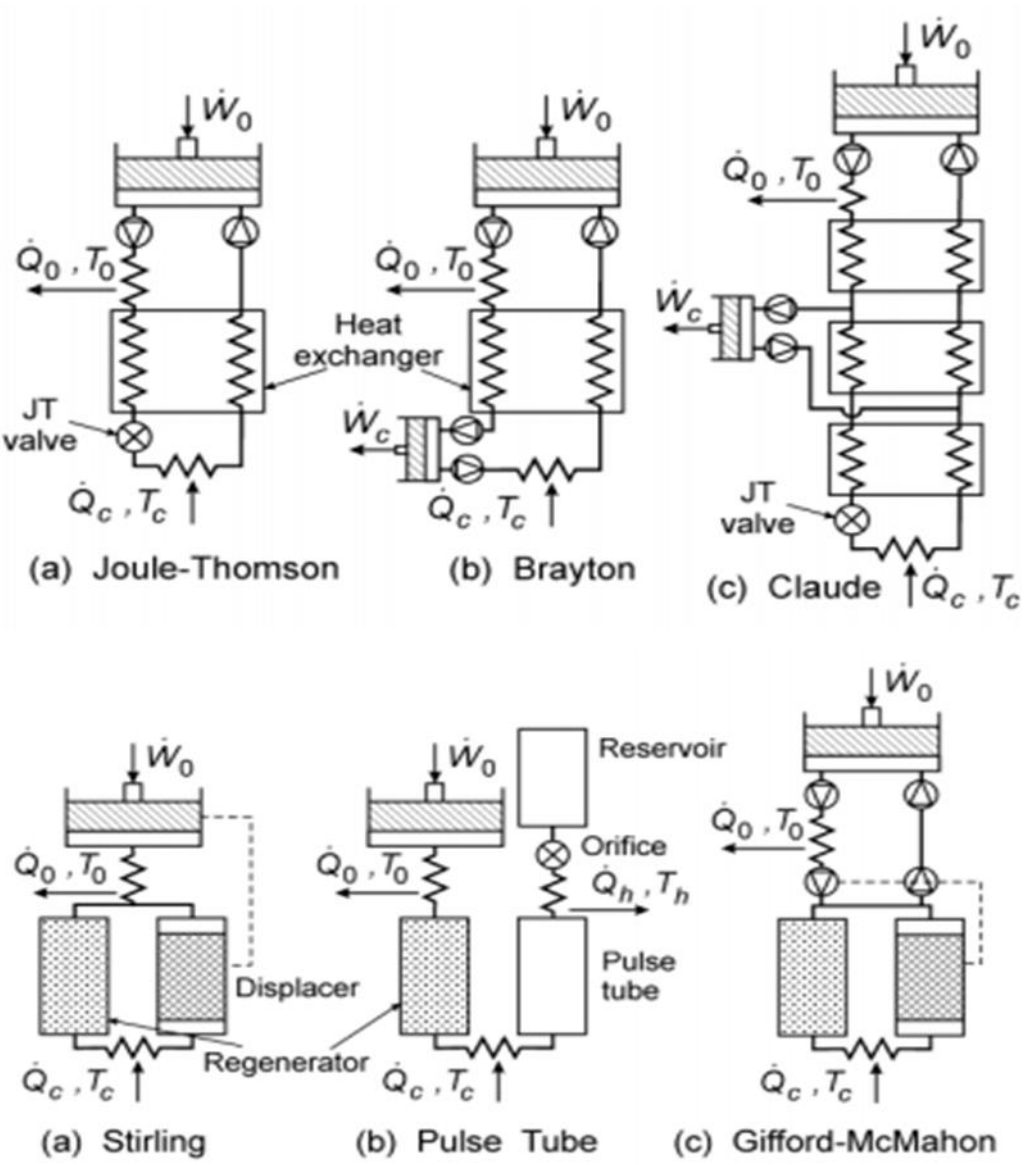

Figure 1.2. Schematic of commonly used cryocoolers – top: Joule-Thomson (a), Brayton (b), Claude (c); bottom: Stirling (a), pulse tube (b), and Gifford-McMahon (c) [Radebaugh (1999, [2])].

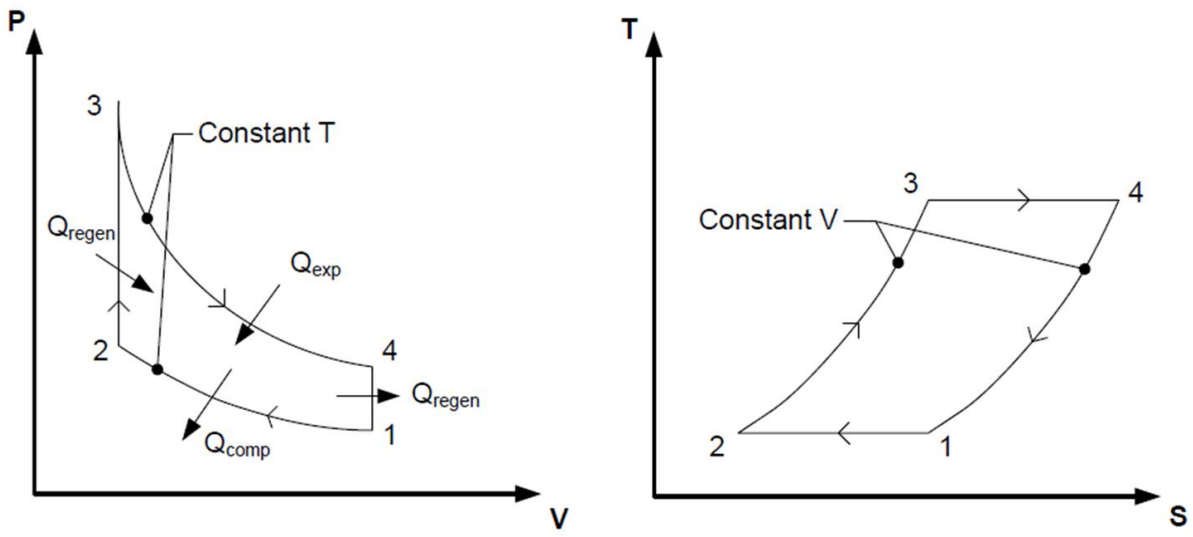

Figure 1.3. Diagrams of ideal Stirling thermodynamic cycle [Landurm (2009, [4])].

The ideal Stirling cycle is described in the pressure-volume (P-V) and temperature-entropy (T-S) diagrams (shown in Figure 1.3). Each diagram describes the states of the working fluid at particular instances during each cycle. Heat is transferred to the fluid in the processes 2-3-4 while heat is transferred away from the fluid in processes 4-1-2. In the process from 3 to 4, fluid is isothermally expanded, absorbing heat from the desired refrigerated environment. A portion of this heat is then stored within the regenerator through a constant-volume process (4-1). During the process from 1 to 2, the working fluid is isothermally compressed and rejects heat to its surroundings. The thermal energy stored within the regenerator is internally absorbed by the fluid in another constant-volume process (2-3). Since all heat is supplied and rejected isothermally, the efficiency of this ideal cycle equals that of a Carnot cycle operating between the same temperatures. A real Stirling cycle would contain efficiencies much less than Carnot due to non-isothermal expansion and compression as well as other inherent irreversibilities such as viscous dissipation.

Since the focus of this investigation is on the periodic flow processes, on both the regenerator component level and pore level, the main application of this study is geared towards regenerative pulse tube cryocoolers, also known as pulse tube refrigerators. Figure 1.4 shows three major configurations of single-stage PTCs (multi-stage PTCs will be discussed later).

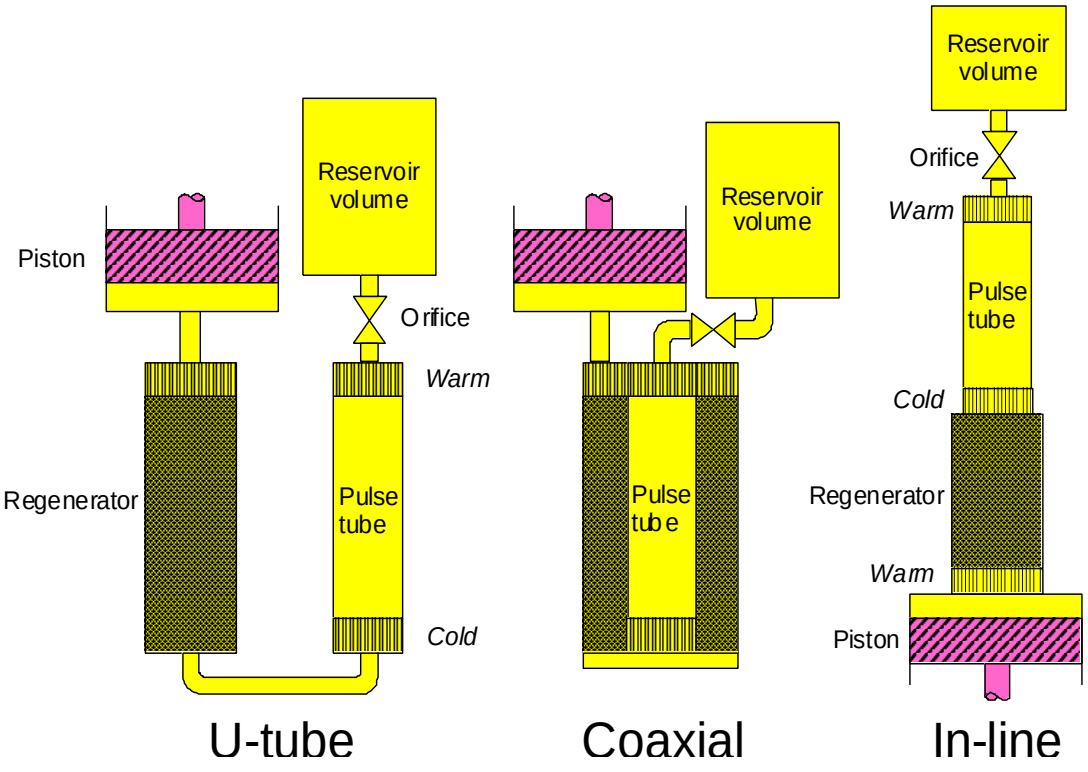

Figure 1.4. Various configurations of PTCs – U-tube (left), coaxial (middle), and in-line (right) [Radebaugh and Gully (2008, [5])].

To explain the components of a typical PTC and its corresponding operative processes in detail, a basic one-stage, in-line, PTC will be considered and is shown in Figure. 1.5.

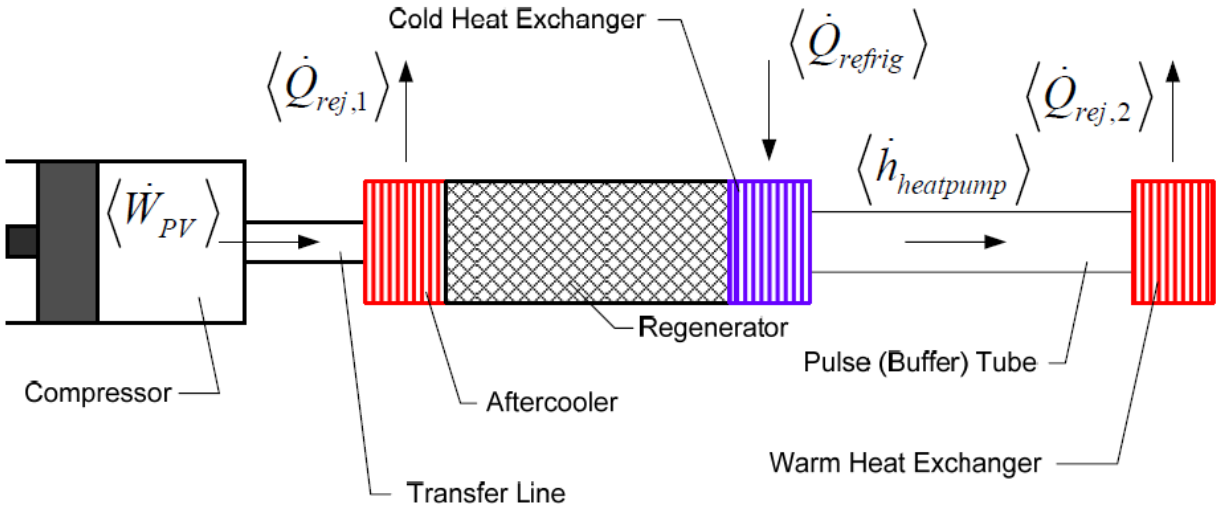

Figure. 1.5 The basic PTC schematic [Pathak (2010, [6])].

Like the Stirling refrigerator, the basic PTC is a simple linear system consisting of a compressor, regenerator and heat exchangers. The compressor generates an oscillating pressure wave and provides a work input to the system. Attached to the compressor through a transfer line is the first warm heat exchanger or aftercooler. Beyond that lies the regenerator which stores and rejects thermal energy in the course of one cycle. Adjacent to the regenerator is the cold heat exchanger which provides the desired cooling load. The pulse tube is then adjoined with another warm heat exchanger on its end. The basic PTC functions much like the Stirling refrigerator, but contains one obvious change - the displacer piston in the expansion space was replaced by a compressible gas piston. The distinct advantage of the PTC over the Stirling refrigerator is the lack of moving parts at the cold end, resulting in increased reliability and operating life with decreased heat losses [Radebaugh (1999, [2])].

A more detailed explanation of the PTC operational process is now presented. An inflow of helium gas is induced by a moving piston, within a compressor. Helium is primarily used as the working fluid in pulse tube refrigerators due to its ability to stay in

the gaseous phase at very low temperatures. Also, helium has a high volumetric heat capacity and high thermal conductivity. From the compressor, the gas flows through the transfer line and enters a warm heat exchanger, where heat is rejected from the fluid to the heat exchanger walls. From the warm heat exchanger, the helium gas transfers through the regenerator where heat is transferred from the fluid to the conductive regenerator material. The gas then goes through the cold heat exchanger, where heat is received by the fluid, and enters the pulse tube section. After the pulse tube, the gas flows through another warm heat exchanger, where again heat is rejected. From this point the gas oscillates back to the start of the process. When the gas flows back through the regenerator, the fluid is cold and heat transfers from the regenerator solid material to the fluid, serving as preheating before the gas enters the aftercooler [Pathak (2010, [6])]. For simplicity the aforementioned PTC process description was explained as if the working fluid gas travels through the entire system, whereas in actuality, the working fluid gas particles oscillate in place moving slightly and the associated hydrodynamic and thermal processes occur in the system as a gas bucket brigade.

An ideal pulse-tube cycle does not exist as there are no well-defined stages in which to characterize the state of the working fluid other than pressure. With no sequence of ideal gas processes, the conventional pressure-volume and temperature-entropy diagrams cannot be constructed. The pulse tube cooling effect relies on unsteady behavior and if fluid processes were steady and ideal, the device would fail to function [Organ (1992, [7])].

Other types of pulse tube cryocoolers include the orifice pulse tube cryocooler and the inertance-tube pulse tube cryocooler, shown in Figures 1.6 and 1.7, respectively.

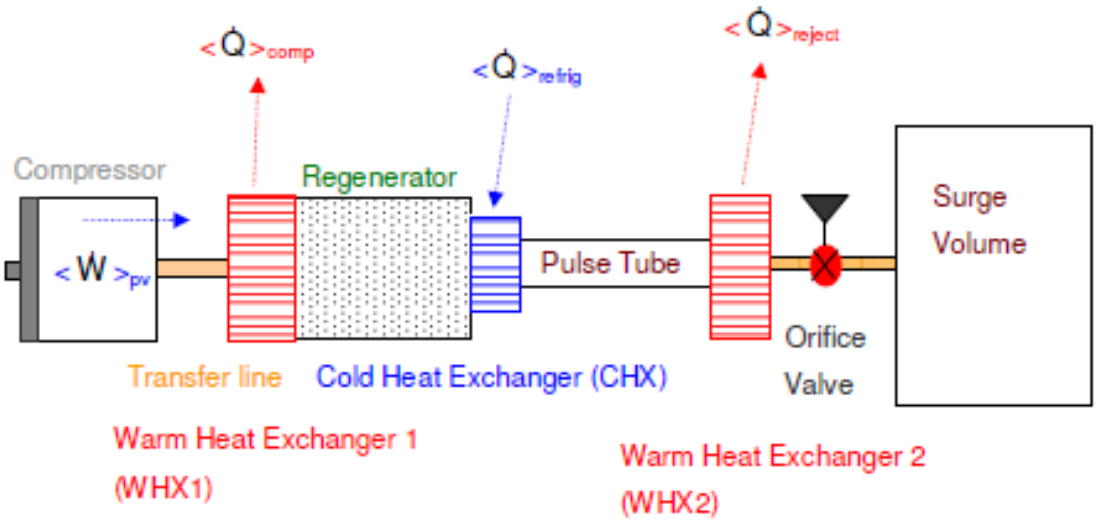

Figure 1.6. Orifice pulse tube Cryocooler schematic [Pathak (2010, [6])].

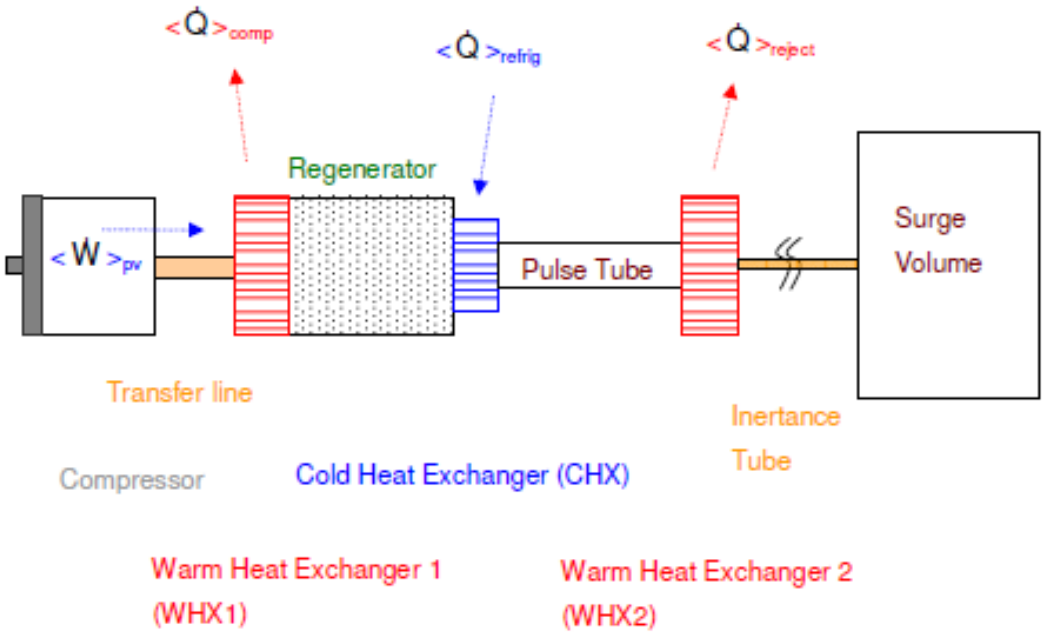

Figure 1.7. Inertance-tube pulse tube Cryocooler schematic [Pathak (2010, [6])].

The orifice pulse tube cryocooler adds a surge volume and an orifice valve to the basic pulse tube cryocooler in order to improve its performance. The role of the orifice is to help improve a phase difference between the pressure and mass flow waves, which is required for the operation of pulse tube refrigerators. The inertance tube pulse tube cryocooler replaces the orifice valve from the orifice pulse tube cryocooler with an inertance tube. The advantage of the inertance-tube pulse tube cryocooler is the fact that the piston within the compressor is the only moving component of the system. Due to not having any system level moving parts (with exception of the compressor, of course), this particular cryocooler is the most reliable and long lasting, making it ideal for space-based applications.

PTCs can also be staged in order to achieve lower temperatures at higher overall system efficiencies, through two common methods – fluid coupling and thermal coupling. Fluidic coupling is when the working fluid flow literally splits, for example: flow between the cold heat exchanger and corresponding pulse tube gets split where a portion of the mass flow travels to the pulse tube and the remaining mass flow visits another regenerator, which is the entrance of the second stage. In this particular case, the cold heat exchanger is actually seen as an aftercooler for the second stage. An example of fluidic coupling can be seen in Figure 1.8.

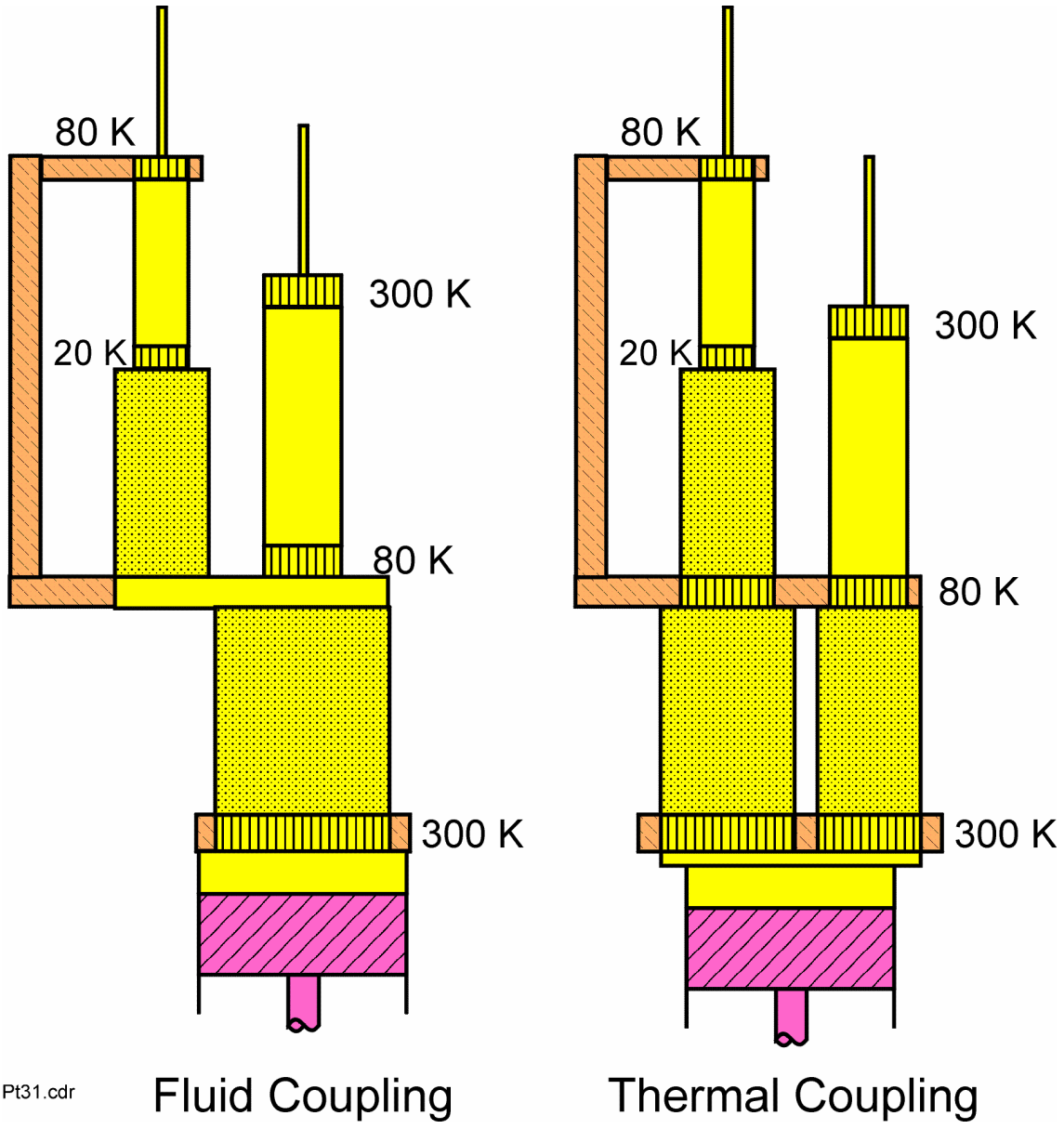

Figure 1.8. Thermal coupling (right) and fluid coupling (left) in PTC staging schematic [Radebaugh (2011, [8])].

In thermal coupling, also shown in Figure 1.8, the two stages concurrently exist and a special thermal bus connection is made between the cold heat exchanger of the first stage and the aftercooler of the second stage. The second stage has a pre-cooling regenerator between the compressor end and the aftercooler of the second stage. This

regenerator produces heat that must be absorbed by the first stage, hence the first stage must have a heat life capacity larger than the amount that must be absorbed from the precooling regenerator. This coupling scheme allows for the second stage warm temperature to be that of the first stage cold temperature. Typically for temperatures down to about 10-15 K, a two-stage PTC performs quite efficiently, however to achieve even lower temperatures including 4 K or below ranges, three or more stages have been designed and fabricated (Lockheed Martin's 4-stage cooler, [Olson et al. (2006, [9])].

1.3 Applications of Pulse Tube Cryocoolers

One of the earliest applications, and one that appeared about 50 years ago, was for cooling infrared sensors to about 80 K for night vision capability. In this respect, as of the year 2000, over 125,000 Stirling cryocoolers for this tactical military application had been produced [Radebaugh (2000, [10])]. In the space satellite applications, PTCs are mainly used for cooling of infrared focal plane arrays and their associated optics. The cooling of superconducting circuits, propellant preservation for the combustion stages of a spacecraft propulsion unit, thermal management of exploration systems and galactic radiation combat units, in space applications are also suitable for PTC systems. For the former applications a space certified PTC can cost anywhere from $1M to $10M. The main reason behind these high prices is the requirement of long life reliability, (typically 7 to 10 years without failure) in Earth's orbit [Cha (2007, [11])].

Apart from space and military applications, PTCs are also suitable for application in high-temperature superconductors, superconducting magnets of Magnetic Resonance Imaging (MRI) systems, superconductors in wireless communication bases, mine sweeping magnets, space instruments, weapon systems, infrared focal plane arrays and detectors, storage of medical specimens, cryosurgery, gas liquefaction, and Liquified

Natural Gas (LNG) transportation, along with many more applications. Table 1.1 shows a brief list of cryogenic system applications. It should be emphasized, however, along with the aforementioned applications for cryogenic refrigerators, numerous other current and potential applications exist that could also benefit from pulse tube cryocooling since cryogenics is an enabling technology.

Table 1.1. List of cryocooler applications in various industries [Radebaugh (1999, [2])].

Military
1. Infrared sensors for missile guidance
2. Infrared sensors for surveillance (satellite based)

Police and Security
1. Infrared sensors for night vision and rescue

Environmental
1. Infrared sensors for atmospheric studies of ozone hole and greenhouse effects
2. Infrared sensors for pollution monitoring

Commercial
1. Cryopumps for semiconductor fabrication
2. High temperature superconductors for cellular-phone base stations
3. Superconductors for voltage standards
4. Semiconductors for high speed computers
5. Infrared sensors for NDE and process monitoring

Medical
1. Cooling superconducting magnets for MRI systems
2. SQUID magnetometers for heart and brain studies
3. Liquefaction of oxygen for storage at hospitals and home use
4. Cryogenic catheters and cryosurgery

Transportation
1. LNG for fleet vehicles
2. Superconducting magnets in maglev trains

Energy
1. LNG for peak shaving
2. Infrared sensors for thermal loss measurements
3. Supercond. mag. energy storage for peak shaving and power conditioning

Agriculture and Biology
1. Storage of biological cells and specimens

CHAPTER 2

BACKGROUND

In this chapter a brief history of pulse tube cryocoolers and some important attributes of the regenerator, are discussed. A detailed discussion of transport processes in porous media, including porous media modeling and steady and periodic flow in such systems is presented. Finally, regenerator modeling and theory is then offered along with regenerator experimental measurements and studies, and the theory and method of determining hydrodynamic and thermal energy closure parameters.

2.1 History of Pulse Tube Cryocoolers

After the Stirling engine was introduced and employed for over a century, another similar regenerative cycle application developed. Gifford and Longsworth from Syracuse University in the mid-1960s pioneered the application of pulse tube cryocoolers and achieved a cold end temperature of 124 K [Gifford and Longsworth (1997, [12])]. Their first design was based on a hollow cylindrical tube with one end open and the other end closed, where the closed end was exposed to an ambient temperature heat exchanger, while the open end represented the cold finger. Thermal interaction between the working fluid and the tube walls would result in a surface heating effect. Continued research at Syracuse University demonstrated that installing a thermal regenerator between the compressor and the pulse tube, achieved a cooling effect [Popescu et al. (2001, [13])]. As a result of the oscillatory flow field caused by a compressor piston, the open end was subjected to an oscillating pressure from the regenerator, causing the open end to cool [Harvey (1999, [14])]. Furthermore, absence of a moving displacer at the cold end

minimized potential vibrations. A heat exchanger was later added to the open end of the pulse tube, making the cryocooler a closed system. This concept led to the creation of the basic pulse tube refrigerator, as shown in Figure 2.1.

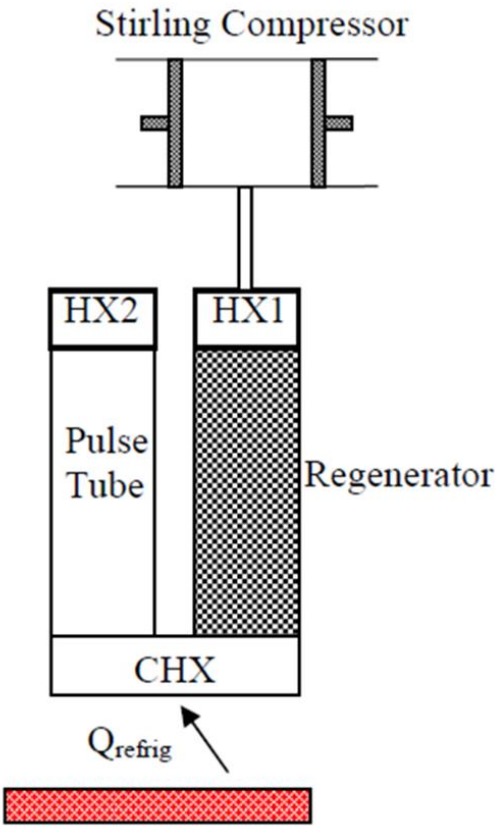

Figure 2.1. Basic pulse tube refrigerator schematic [Cha (2007, [11])].

Although the basic PTC was relatively low in Carnot efficiency, it was recognized that the cooling power varied with the phase shift of pressure waves at the input of the pulse tube and those reflected by the closed end of the pulse tube. Since then, much progress has been made in order to improve the performance, reliability, and efficiency of pulse tube cryocoolers, including the development of orifices, bypass lines, and inertance

tubes as additional components to the basic PTC. A multitude of ideas have been introduced to optimize this phase shift and maximize the enthalpy flow through the pulse tube. Figure 2.2 shows examples of these PTCs [Landrum (2009, [4]), Conrad (2011, [15])].

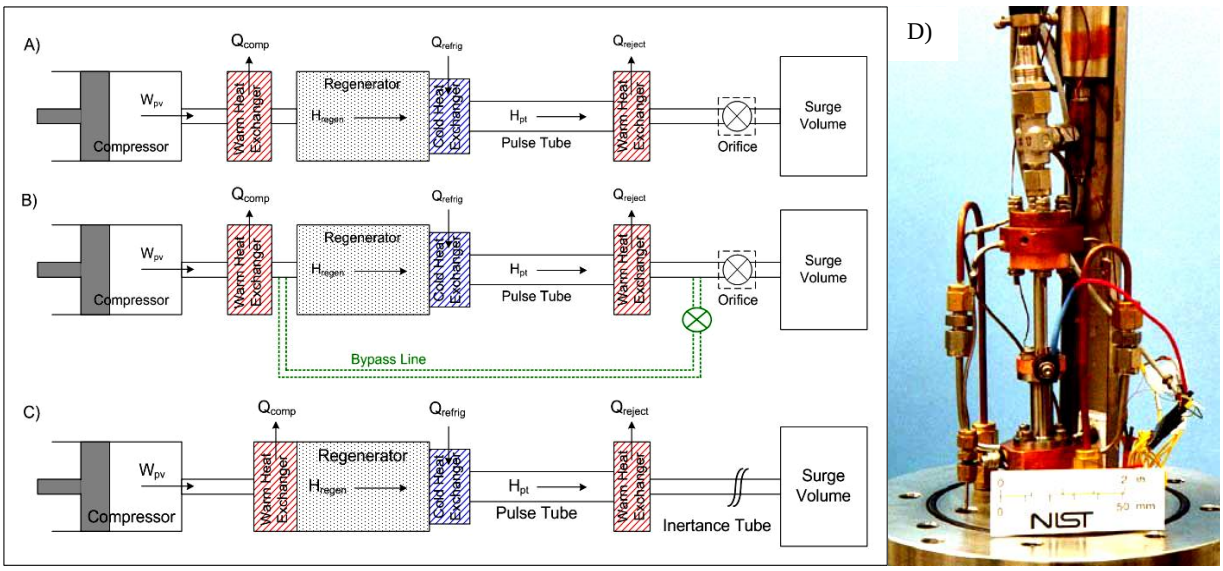

Figure 2.2. Examples of PTCs – A) Orifice pulse tube refrigerator; B) Double inlet pulse tube refrigerator; C) Inertance tube pulse tube refrigerator; D) NIST experimental PTC system [Conrad (2011, [15])].

In 1984, a Russian researcher named, Mikulin added an orifice valve and a buffer volume to the closed end of the basic PTC, as shown in Figure 2.2 [Mikulin et al. (1984, [16])]. The purpose behind these additional components was to create a more appropriate phase relationship between the oscillatory pressure and the mass flow rate. By this favorable in-phase relationship, the orifice PTC achieved higher performance efficiency than the basic PTC, which lead to cooling temperatures as low as 60-120 K, and later became the modern PTC, commonly known as orifice PTC, which achieved temperatures down to 60 K.

Additional improvements came with the additions of a secondary orifice and bypass line in 1990 by Zhu [Zhu et al. (1990, [17])]. This change improved the control over the phasing between pressure and flow oscillations, hence increasing the efficiency of this pulse tube refrigerator, which reached a temperature of 42 K at the cold end, shown in Figure 2.3.

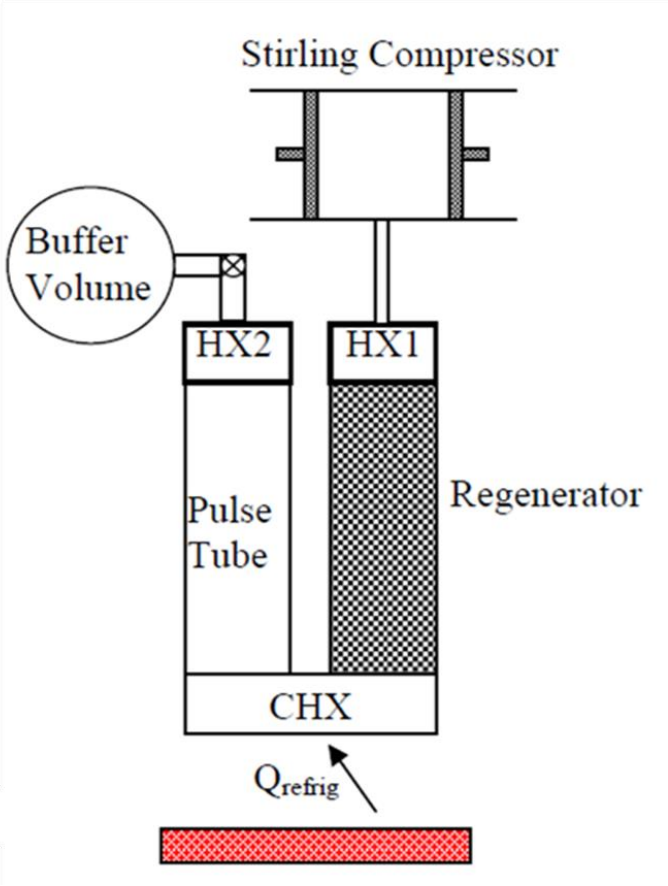

Figure 2.3. The orifice PTC schematic [Cha (2007, [11])].

Gardner and Swift later developed the inertance tube pulse tube refrigerator after Zhu reported the effectiveness of "long neck tubes" for controlling the phase in 1997 PTCs [Zhu et al. (1997, [18]), Gardner and Swift (1997, [19])]. The orifice valve of the orifice PTC was replaced by this long narrow tube called the inertance tube, shown in Figure 2.4. In its most basic form, an inertance tube is simply a tube that imposes a

hydraulic resistance and causes an adjustable delay or phase shift between the pressure and mass flow responses of the pulse tube and the reservoir. In fact, by employing an electrical analogy, Roach and Kashani have shown why the inductance added by the inertance tube allows for an improved enthalpy transfer in the pulse tube PTCs [Roach and Kashani (1998, [20])].

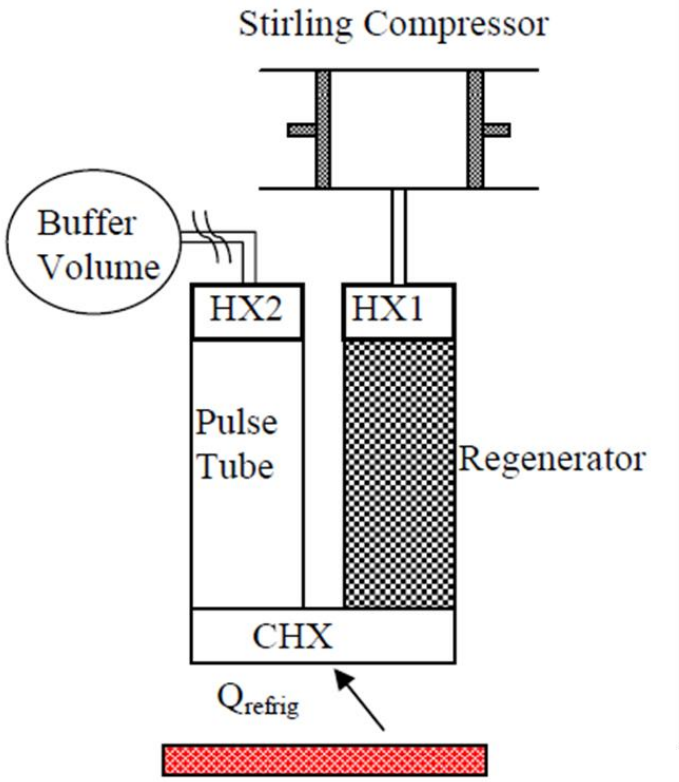

Figure 2.4. Inertance-tube PTC schematic [Cha (2007, [11])].

Cryocoolers with multiple stages, shown in Figure 2.5, have also been developed in order to reach lower temperatures at higher system efficiencies.

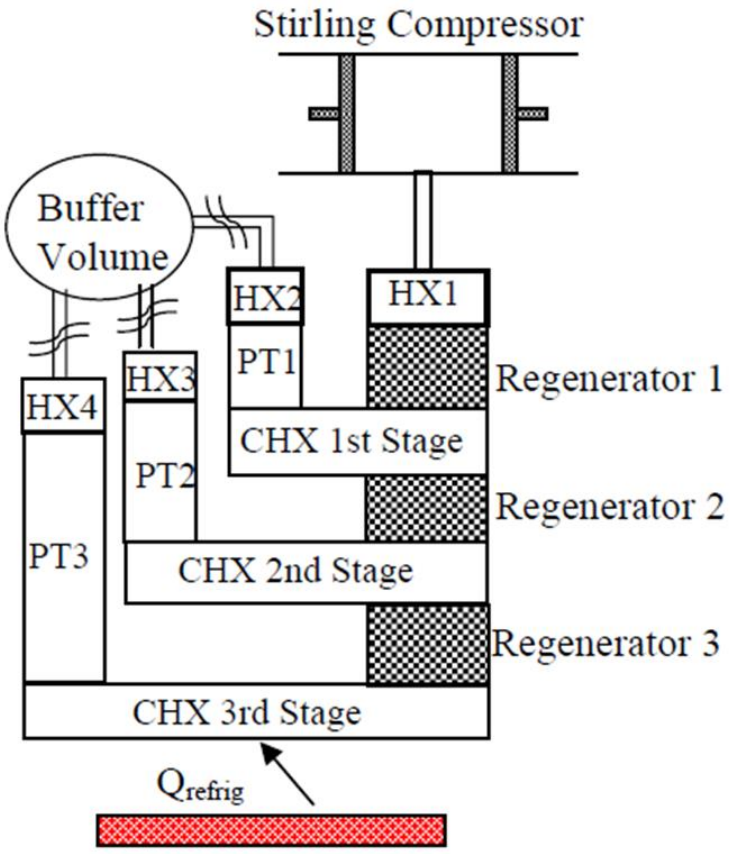

Figure 2.5. Multi-stage PTC schematic [Cha (2007, [11])].

In the last few decades, adjustments to the basic PTR and other such cryocoolers have led to improvements in overall system performance. A summary of these evolutions are displayed in Table 2.1.

Table 2.1. PTR developmental milestones [Landrum (2009, [4])].

1984	Mikulin et al.	Orifice Pulse Tube Refrigerator (OPTR) – placed orifice inside pulse tube to achieved temperature of 105 K.
1985	Radebaugh et al.	Needle valve placed outside pulse tube to achieved temperature of 60 K.
1990	Zhu, Wu & Chen	Double Inlet Orifice Pulse Tube Refrigerator (DIOPTR) - introduced a bypass channel connecting the compressor and warm end of the pulse tube to reduce regenerator losses.
1996	Zhu et al.	Inertance Tube Pulse Tube Refrigerator (ITPTR) – long tube replaced the orifice as the phase shifting mechanism.
1997	Olson & Swift	Tapered pulse tube was utilized to eliminate acoustical streaming in OPTRs.
2007	Garaway & Grossman	Miniature reservoir-less ITPTR (RLITPTR) is designed and tested, reaching a temperature of 146 K.

Modern PTC designs often utilize an orifice along with a reservoir volume to achieve proper phasing. However, this sharp contraction remains a large source of irreversibility so an inertance tube is utilized in place of the orifice leading to increased efficiencies. PTC systems can even achieve compliance through an inertance tube without a surge volume, drastically reducing overall system volume by coiling the interance tube into a tight bundle. Proper operation of individual components is essential for system integration.

A recent trend-setting issue regarding cryocoolers is the miniaturization of such systems. In an age of microelectronics, the demand for compact and low-temperature cryocoolers is ever increasing. In the last decade, there has been a considerable effort to minimize parameters such as mass, volume, cost, and input power, while increasing cryocooler performance. Miniaturization of cryocoolers has been an ongoing process since 1999. Understanding the loss mechanisms of such small-scale devices leads to

several design principles essential for miniature PTCs - high operating frequencies at small tidal displacements, a regenerator matrix with small hydraulic diameters and increased fill pressures [Garaway and Grossman (2008, [21])]. Thermal management of temperature gradients over significantly reduced length scales is among the ultimate performance limitations.

It must be mentioned that although previous studies show PTCs as low efficiency systems compared to other available crycoolers and hence limited in their employment, PTC's have now equaled or in some cases surpassed Stirling cryocoolers [Radebaugh (2009, [22])]. Thus, even though PTCs are not currently used in consumer products due to their low efficiency, the situation may change in the future.

2.2 Transport Processes in Porous Media

The discussion thus far must have made clear the utmost importance of porous media flow and heat transfer phenomena in relation to PTCs. In this section a description and discussion of the relevance of porous media to PTCs will be presented. Modeling methods and a literature survey on porous media will then follow. The section concludes with a review of the hydrodynamic and thermal studies of steady and periodic flows in porous media.

2.2.1 Description and Relevance of Porous Media

Periodic flows in porous media are encountered in some important industrial applications including conventional heat exchangers, microchannels, and the regenerators and heat exchangers of Stirling and pulse tube cryocoolers, which during their normal

operation are subject to periodic flows of working fluid, typically helium. During their normal operation, regenerative cryocoolers are subject to periodic flow with frequencies that range from a few to more than a hundred cycles per second. Frictional losses and other types of irreversibility in the regenerators and heat exchangers of Stirling and pulse tube cryocoolers adversely impact their performance. An understanding of the hydrodynamics and thermal transport phenomena in porous media during periodic flow is necessary for the development of reliable analytical or numerical design tools for these cryogenic systems.

Transport phenomena in periodic flow in porous media are not well understood, however. At the geometric scales of interest in PTCs, direct experimental measurement or visualization of pore-level flow and heat transfer phenomena is currently impractical. This impracticality is due to the difficulty involved with extracting temperature and velocity data from micron-sized regenerator filler material, which operate at cryogenic temperatures and pressures. Numerical simulations with minimal modeling approximations present an alternative to experiments. Past studies of steady flow in generically-configured porous media are extensive [Kuwahara et al. and Nakayama et al. (1996-2007, [23-30])], however limited material has been published about periodic flow [Kim and Ghiaasiaan (2009, [31]), Pathak and Ghiaasiaan (2010, [32]), Mulcahey et al. (2012, [33])].

2.2.2 Porous Media Models

Tractable conservation equations for flow in porous media can be derived by volume-averaging of the local and instantaneous conservation equations [Kaviany (2006, [34]), Whitaker (1999, [35]), Grant and O'Neil (1976, [36]), Quintard et al. (1997, [37]), Monye et al. (2000, [38])], or by simply postulating model transport equations [Vafai and

Tien (1981, [39]), Vafai and Amiri (1998, [40]), Hsu et al. (1999, (41)]. These tractable conservation equations are not concerned with pore-level phenomena, and deal with macroscopic flow and transport processes instead.

Volume-averaged conservation equations can be derived rigorously, starting from the local and instantaneous differential conservation equations [Kaviany (2006, [34]), Whitaker (1999, [35]); Harvey (2003, [42])]. The formulations of the volume-average governing equations that are presented in this section are consistent with commonly used porous media literatures [Whitaker (1999, [35]), Nakayama et al. (2001, [27]), Kim and Ghiaasiaan (2009, [31])].

Any volume-average fluid property can be found from,

$$\langle \phi \rangle^f = \frac{1}{V_f} \int_{V_f} \phi \, \mathrm{d}V \tag{2.1}$$

where:

ϕ = Any fluid property

V_f = Fluid volume

Evidently, for volume averaging to make sense, V_f should be large enough to smooth out the effects of small scale discontinuities.

Now, consider the flow of an incompressible fluid in a porous medium. The local and instantaneous mass, momentum, and energy conservation equations in Cartesian coordinates will then be (note that Einstein's summation notation was used).

$$\frac{\partial u_j}{\partial x_j} = 0 \tag{2.2}$$

$$\frac{\partial u_i}{\partial t} + \frac{\partial}{\partial x_j} u_j u_i = -\frac{1}{\rho}\frac{\partial p}{\partial x_i} + \frac{\partial}{\partial x_j}\nu_f \left(\frac{\partial u_i}{\partial x_j} + \frac{\partial u_j}{\partial x_i} \right) \tag{2.3}$$

$$\rho_f c_{pf} \left(\frac{\partial T}{\partial t} + \frac{\partial}{\partial x_j} u_j T \right) = \frac{\partial}{\partial x_j} \left(k_f \frac{\partial T}{\partial x_j} \right) \tag{2.4}$$

where:

u_j = Velocity vector

ν_f = Fluid kinematic viscosity

t = Time

c_{pf} = Fluid specific heat

k_f = Fluid thermal conductivity

T = Temperature

Any fluid property can be separated into a volume-average fluid property term and a spatial deviation term,

$$\phi = \langle \phi \rangle^f + \tilde{\phi} \tag{2.5}$$

where $\tilde{\phi}$ represents the spatial deviation of fluid property ϕ.

To derive tractable equations, volume-averaging is now applied to all of the terms in the above conservation equations. The mass conservation equation will give,

$$\frac{\partial \langle u_j \rangle^f}{\partial x_j} = 0 \tag{2.6}$$

Volume averaging of the momentum conservation equation will lead to complicated terms that result from solid-fluid interactions. Detailed derivation and discussion can be found in Grant and O'Neil [Grant and O'Neil (1976, [36])] and Harvey [Harvey (2003, [42])]. The complicated fluid-solid interaction terms are replaced with model terms in practice, however, to render tractable equations. Perhaps the most widely-used model volume-average fluid momentum conservation equation is the Forchheimer-extended Darcy equation,

$$\begin{aligned} &\frac{\partial \langle u_i \rangle^f}{\partial t} + \frac{\partial}{\partial x_j} \langle u_j \rangle^f \langle u_i \rangle^f = -\frac{1}{\rho} \frac{\partial \langle p \rangle^f}{\partial x_i} \\ &+ \frac{\partial}{\partial x_j} \nu_f \left(\frac{\partial \langle u_i \rangle^f}{\partial x_j} + \frac{\partial \langle u_j \rangle^f}{\partial x_i} \right) - \frac{\nu_f}{\bar{\bar{K}}} \varepsilon \langle u_i \rangle^f - \varepsilon^2 \bar{\bar{b}} \cdot \left| \langle u_k \rangle^f \right| \langle u_i \rangle^f \end{aligned} \tag{2.7}$$

where:

$\bar{\bar{b}}$ = Forchheimer coefficient tensor

$\bar{\bar{K}}$ = Permeability tensor

Note that in the above equation non-isotropy of a porous medium is considered. The permeability and Forchheimer coefficients are thus in general symmetric second-rank tensors [Bear (1972, [43])].

Two important points should be made about Equation 2.7. First, the equation in principle is applicable only to quasi-steady (slow transient) conditions. This can be understood, for example, by examining the rigorous theoretical bases for the definition of permeability and Forchheimer coefficients. Grant and O'Neil [Grant and O'Neil (1976, [36])], for example, show that the permeability and Forchheimer coefficients and their corresponding terms in the momentum equation result from the series expansion of surface-fluid momentum interaction term by truncating the expansion at the second order term. Such truncation is clearly acceptable only for slow transients. Secondly, although the representation of the momentum equation in the above volume-averaged form is a simplification by itself, the elements of the permeability and Forchheimer coefficients still need to be specified. These can be found experimentally only for relatively simple configurations and boundary conditions. When experimental measurements are problematic, direct numerical simulation can be used [Kim (2008, [44])].

The volume-average fluid energy conservation equation will be (note that this is not a model equation),

$$\varepsilon\rho_f c_{pf}\left(\frac{\partial\langle T\rangle^f}{\partial t}+\frac{\partial}{\partial x_j}\langle u_j\rangle^f\langle T\rangle^f\right)= \\ \frac{\partial}{\partial x_j}\left(\varepsilon k_f\frac{\partial\langle T\rangle^f}{\partial x_j}+\frac{k_f}{V}\int_{A_{\text{int}}}Tn_j\mathrm{d}A-\varepsilon\rho_f c_{pf}\langle\tilde{u}_j T\rangle^f\right)+\frac{1}{V}\int_{A_{\text{int}}}k_f\frac{\partial T}{\partial x_j}n_j\mathrm{d}A \tag{2.8}$$

where:

$\langle T\rangle^f$ = Volume-average fluid temperature

n_j = Component of the unit vector pointing out from the fluid into the solid

A_{int} = Solid-fluid interface area

$\varepsilon \rho_f c_{pf} \left\langle \tilde{u}_j T \right\rangle^f$ = Thermal dispersion

ε = Porosity

The term $\frac{\partial}{\partial x_j} \frac{k_f}{V} \int_{A_{\text{int}}} T n_j \mathrm{d}A$ is called the tortuosity term. It vanishes when the surface temperature is uniform. The third term in the bracket on the right side of the above equation represents thermal dispersion. The thermal dispersion represents the amount of energy a fluid particle loses or gains in a unit cell due to momentum transfer and thermal energy storage. The last term on the right side represents the solid-fluid (interfacial) heat transfer.

Consistent with the volume-averaging concept, the average interfacial heat transfer coefficient may be defined by writing,

$$\frac{1}{V} \int_{A_{\text{int}}} k_f \frac{\partial T}{\partial x_j} n_j \mathrm{d}A = a_f h_f \left(\langle T \rangle^s - \langle T \rangle^f \right) \tag{2.9}$$

where:

a_f = Solid-fluid specific area (interfacial area concentration)

h_f = Heat transfer coefficient (also called convection coefficient)

$\langle T \rangle^s$ = Average solid surface temperature in the reference volume

The interfacial heat transfer coefficient (Equation 2.9) can be substituted into the fluid energy conservation equation (Equation 2.8) and the resulting simplified thermal energy conservation equation takes the following more familiar form,

$$\varepsilon\rho_f c_{pf}\left(\frac{\partial\langle T\rangle^f}{\partial t}+\frac{\partial}{\partial x_j}\langle u_j\rangle^f\langle T\rangle^f\right)=$$
$$\frac{\partial}{\partial x_j}\left(\varepsilon k_f\frac{\partial\langle T\rangle^f}{\partial x_j}-\varepsilon\rho_f c_{pf}\left\langle\tilde{u}_j T\right\rangle^f\right)-a_f h_f\left(\langle T\rangle^f-\langle T\rangle^s\right) \tag{2.10}$$

It is emphasized that the volume-average governing equations described in this section consider the fluid to be Newtonian and incompressible, and have constant properties. The industrial applications of interest to this study involve Newtonian fluids in low Mach number conditions.

The Forchheimer-extended Darcy equation (Equation 2.7), cast for the incompressible flow through a homogeneous and isotropic porous medium, has been widely used in experimental and numerical studies on convection heat transfer in a fully saturated porous media. For an isotropic porous medium permeability and Forchheimer coefficients are both scalar quantities. For steady flow in a homogeneous porous medium, for example, one can write [Vafai and Tien (1981,[39]), Hsu and Cheng (1990,[45])],

$$-\nabla\langle p\rangle^f=\frac{\mu_f}{K}\langle\vec{u}\rangle+\rho_f b\left|\langle\vec{u}\rangle\langle\vec{u}\rangle\right|^{\frac{1}{2}}\langle\vec{u}\rangle \tag{2.11}$$

where:

K = Permeability coefficient

b = Forchheimer coefficient

ρ_f = Fluid density

μ_f = Fluid dynamic viscosity

$\langle p\rangle^f$ = Intrinsic volume-average fluid static pressure over a fluid volume V_f

Equation 2.11 is the familiar form of the Forchheimer-extended Darcy equation. When the velocity is sufficiently small, the Forchheimer term $\rho_f B \left|\langle\vec{u}\rangle\langle\vec{u}\rangle\right|^{\frac{1}{2}}\left\langle\vec{u}\right\rangle$ of Equation 2.11 becomes negligibly small and the equation is reduced to the well-known Darcy's law as follows,

$$-\nabla\langle p\rangle^f = \frac{\mu_f}{K}\left\langle\vec{u}\right\rangle \tag{2.12}$$

Thus, for very low Reynolds number flows through porous media, the pressure gradient is proportional to the superficial velocity.

Darcy flow regime, which is the dominant flow regime in underground water flows, for example, has limited applications in many engineering systems. In practice various flow regimes can occur in a porous medium. Figure 2.6 shows qualitatively the flow regimes in a homogeneous porous medium. It can be seen that there are three major flow regimes in laminar flow. At extremely low flow rates, the surface-interactive force dominates. This flow regime is typically of little interest to most applications. Without considering the surface-interactive force dominant flow regime which is only observed under very weak flows, the spectrum of laminar flow in porous media can be divided into Darcy's flow (where fluid inertia effect is negligible) and Forchheimer flow regions in which inertial effects become increasingly important [Liu et al. (1994, [46])]. The critical Reynolds number for the transition from Darcy's (viscous dominant) flow to Forchheimer (inertia dominant) flow, Re_{tran}, has been examined by many researchers. For example, $\mathrm{Re}_{tran} \approx 4$ according to Liu et al. [Liu et al. (1994, [46])], while transition occurs in the range $1 < \mathrm{Re}_{tran} < 13$ according to Coulaud et al. [Couland (1988, [47])].

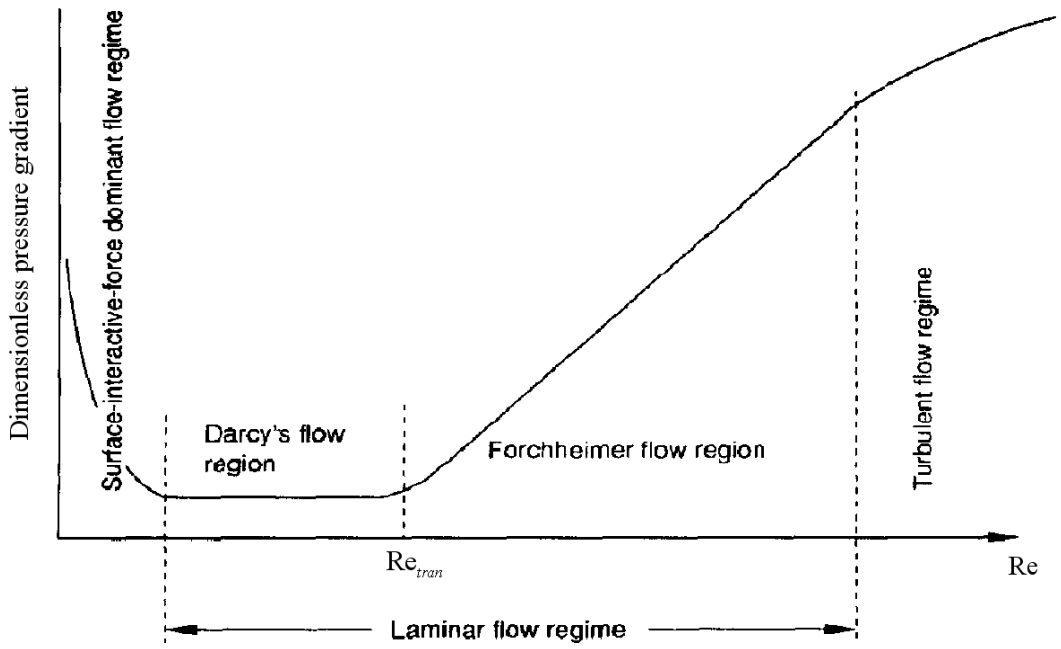

Figure 2.6. Laminar flow regions in porous media [Liu et al. (1994, [46])].

Turbulent flow can occur in porous media, and like most other applications the transition from laminar to turbulent flow regime is an extremely important threshold. The hydrodynamic conditions that lead to the onset of turbulent flow under steady flow conditions have been investigated in the past [Pedras and de Lemos (2001, [48])]. Little is known about turbulent flow in porous media under pulsating or periodic flow, however. Consequently, due to the lack of directly-applicable information, steady flow criterion has been used for the onset of turbulent flow regime [Landrum (2009, [4]), Clearman (2007, [49]), Cha (2007, [11])].

The pore – based Reynolds number is defined as,

$$\mathrm{Re}_K = \frac{\rho_f \left|\left\langle \vec{u} \right\rangle\right| \sqrt{K}}{\mu_f} \tag{2.13}$$

As noted, the length scale in this definition is the square root of permeability. For steady flow, laminar flow regime is maintained as long as the value of the above Reynolds number is at or below 300 [Pedras and de Lemos (2001, [48])]. In certain industry scenarios, a hydraulic diameter based Reynolds number is also considered. In this case, the square root of the permeability term in Equation 2.13 is substituted with the hydraulic diameter divided by the porosity of the system. This typically increases the order of magnitude of the Reynolds number value by 10^1 to 10^3.

2.2.3 Steady and Quasi-Steady Flow in Porous Media

There have been numerous studies for transport phenomena in porous media, however most porous media literature deals mainly with steady flow situations, whereas significant industrial applications require knowledge of periodic flows. Design and analysis tools addressing pulsating or periodic flow in porous media should evidently use tractable model conservation and transport equations that are often derived based on the homogenization technique, volume-averaging, or simple postulation. As noted earlier, volume-average conservation and transport equations for steady or quasi-steady flows in porous media have been rigorously derived by several authors [Kaviany (2006, [34]), Whitaker (1999, [35]), Grant and O'Neil (1976, [36]), Quintard et al. (1997, [37]), Monye et al. (2000, [38])], and postulated and discussed by others [Vafai and Amiri (1998, [40]), Hsu et al. (1999, [41])]. Quasi-steady flow approximation is reasonable with low frequency flow oscillations. Sözen and Vafai [Sözen and Vafai (1991, [50])], who were interested in the thermal storage behavior of packed beds under low frequency (

$0.05-0.2\,Hz$) oscillatory compressible flow conditions, applied standard macroscopic porous media conservation equations with closure relations borrowed from steady flow literature, and noted little difference between steady and oscillatory boundary conditions with respect to the energy storage behavior of their investigated packed bed. Furthermore, experience shows that the standard model equations such as Equation 2.7 are often applied to moderately fast transient flows in porous media, even though their applicability to fast transients is questionable in most operating scenarios. In any case, the volume-average equations need closure relations for solid-fluid interactions which must be found from experiment or pore-level numerical simulations. Several experimental investigations have been reported for periodic flow in porous media that are of interest for cryocooler applications [Nam and Jeong (2002, [51]), Jeong et al. (2002, [52]), Cha et al. (2006, [53]), Clearman et al. (2008, [54])]. These investigations in general have shown that steady-flow closure relations are not *always* suitable for application to periodic flows, and have produced useful experimental data applicable to some widely-used cryocooler regenerator fillers. However there appears to be no systematic investigation about heat or mass transfer phenomena in porous media during fast transients, and in particular in periodic flow conditions.

Reliable closure parameters for volume-average transient flow in porous media can be rigorously obtained when the details of pore-level processes are known. Direct experimental measurements of pore-level transport phenomena are difficult, hence direct numerical simulation can be utilized instead provided that the exact geometry of the porous structure is known. Porous media of course often have complex and non-uniform structures, nevertheless valuable information can be deduced by the direct numerical simulation of flow in generic porous media composed of periodic arrays of regular-shaped structures such as arrays of parallel square or circular cylinders [Kuwahara et al. and Nakayama et al. (1996-2007, [23-30])]. These and other similar investigations thus far have all addressed steady flow.

Two-dimensional flow through arrays of tubes or fins of various shapes is also of great interest in relation to heat exchangers [Sparrow and Grannis (1996, [55]), Cha et al. (2006, [56]), Sahiti et al. (2006, [57])]. Most investigations that were concerned with heat exchangers are interested in tube friction, drag coefficients, and Nusselt numbers. However, flow in large heat exchangers are treated as flow in porous media by many investigators [Raju and Narasimhan (2007, [58]), Missirlis et al. (2010, [59]), Pinson et al. (2007, [60]), Carluccio et al. (2005, [61]), Imke (2004, [62])]. Virtually all past investigations dealing with simulation of flow in heat exchanger tube bundles have addressed steady flow.

As mentioned earlier, since there is much complexity and inaccuracy in experimental studies when dealing with porous media flows due to apparatus, measurement difficulty and flow control, direct numerical simulations that resolve the pore-level geometric details and solve the conservation equations without any arbitrary or simplifying assumptions have become popular as substitutes or complements to experiments dealing with porous media. Many researchers have used numerical models to collect data and derive solutions to flow and energy equations in porous media with simple and generic pore structures.

Nakayama et al. [Nakayama et al. (2001, [27])], utilized a two-energy equation model for analyzing conduction and convection within porous media, where the system is everywhere in local thermal non-equilibrium. The exact solutions were obtained for two cases: the one-dimensional steady conduction in a porous slab with internal heat generations in the solid, and thermally developing unidirectional flow through a semi-infinite medium. Figure 2.7 displays their generic porous media.

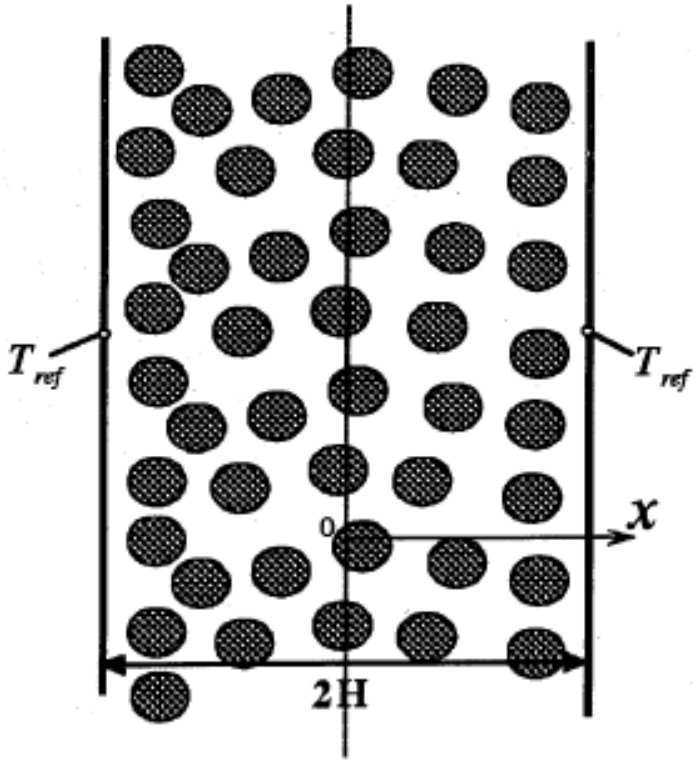

Figure 2.7. Generic porous media [Nakayama et al. (2001, [27])].

Nakayama et al. [Nakayama et al. (2001, [27])], found that for their first case, the solid and fluid temperatures decrease along the x-direction toward the wall (see Figure 2.7). For the second case, the fluid temperature remained fairly constant, while the solid temperature exponentially increased to approach the fluid temperature along the x-direction toward the wall.

Jiang and Ren [Jiang and Ren (2001, [63])], used a numerical model including the thermal non-equilibrium assumption to see the effects of viscous dissipation, the boundary condition assumptions, thermal dispersion, particle diameters, and the variable properties of oil on convection heat transfer in steady flow in a porous medium. They found that viscous dissipation weakened the convection heat transfer from the fluid to the wall in the porous media, where the wall was modeled as a constant wall heat flux boundary condition.

Nakayama et al. [Nakayama et al. (2004, [29])], developed a numerical model for a three-dimensional heat and fluid flow through a bank of infinitely long cylinders in yaw. Figure 2.8 shows a schematic of the porous structure along with a coordinate system they investigated. This investigation is one among several pore-level direct numerical simulations that latter authors had investigated over the past several years. Their simulation results led to the development of a permeability tensor and Forchheimer tensor. These results can be used in order to investigate complex flow and heat transfer characteristics associated with manmade structures such as fins [Kuwahara et al. and Nakayama et al. (1996-2007, [23-30])].

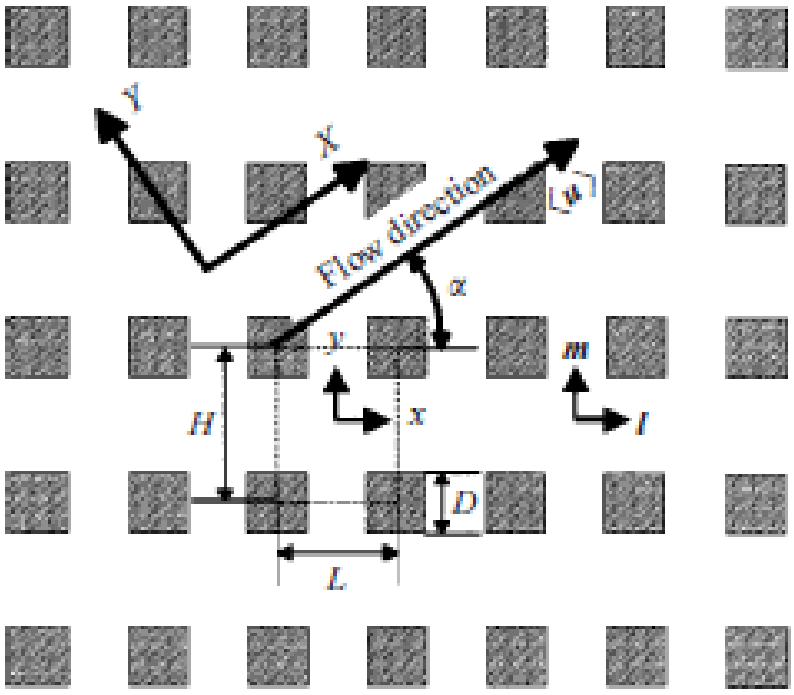

Figure 2.8. Porous structure with coordinate system [Nakayama et al. (2004, [29])].

Recently, Benarji et al. [Benarji et al. (2008, [64])], performed detailed numerical simulations of fluid flow and heat transfer over a bank of flat tubes for both in-line and staggered configurations for isothermal and isoflux boundary conditions. From this, they investigated the effect of Reynolds number, Prandtl number, length ratio, and the height ratio on the Nusselt number. They found that at a particular Reynolds number and Prandtl number, the Nusselt number decreased as the length of the investigated unit cell increased. However, the Nusselt number increased as the height of the unit cell increased, for the same conditions.

An industrial application where porous media analysis proves suitable and handy is the flow in tube bundles in large heat exchangers, or flow through pin fins. The very large number of spatially-periodic tube or pin fin unit cells makes the application of porous-media methods to these applications convenient as well as justifiable [Kim and Ghiaasiaan (2009, [31]), Pathak and Ghiaasiaan (2010, [32]), Mulcahey et al. (2012, [33])].

The above investigations are representative examples out of a large number of investigations that have studied steady flow in porous media. In comparison, investigations dealing with transient pulsating or periodic flow are few. These will be briefly discussed in the next section.

2.2.4 Periodic Flow in Porous Media

Periodic flow, specifically pulsating and oscillatory flow investigations have been few in literature. The subject has attracted significant attention only recently. In view of

the close relevance to this investigation, the present section describes the limited periodic flow studies in some detail, most of which are recent studies.

Guo et al. [Guo et al. (1997, [65])], performed a numerical study of pulsating flow and heat transfer characteristics in a circular pipe partially filled with a porous medium. They utilized the Brinkman-Forchheimer-extended Darcy model for their porous matrix region, which was attached to a pipe wall. The study, of course, was based on the solution of modeled (i.e. volume-average) conservation equations. The investigation showed that the Nusselt number monotonically increased as the porous layer thickness increased. This is graphically shown in Figure 2.9.

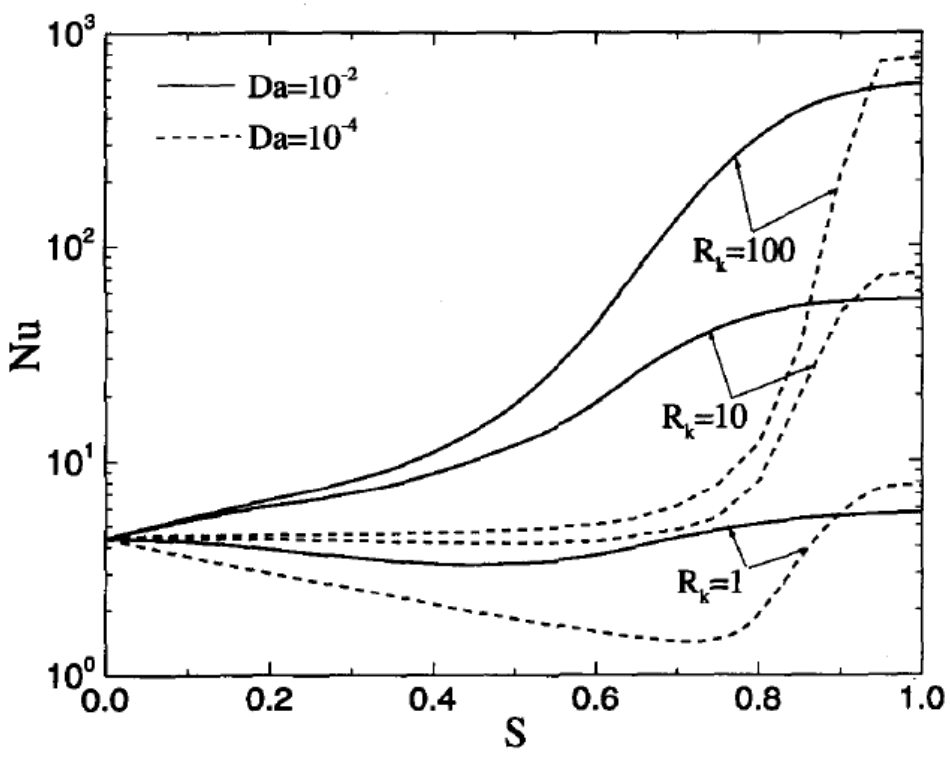

Figure 2.9. Nusselt number as a function of porous layer thickness [Guo et al. (1997, [65])].

Kim and Ghiaasiaan [Kim and Ghiaasiaan (2009, [31]), Kim (2008, [44])], numerically studied the flow friction associated with laminar pulsating flows through porous media, where the structure details of their investigated porous media are shown in Figures 2.10-2.12. They simulated two-dimensional flows in a system composed of unit cells of generic porous structures using a CFD tool, with sinusoidal time variations of flow. Detailed numerical data representing the oscillating velocity and pressure variations for five different generic porous structure geometries in the porosity range of 0.64 to 0.84, with flow pulsation frequency of 40 Hz were obtained, and attention was paid to the phase shift characteristics between the velocity and pressure waves.

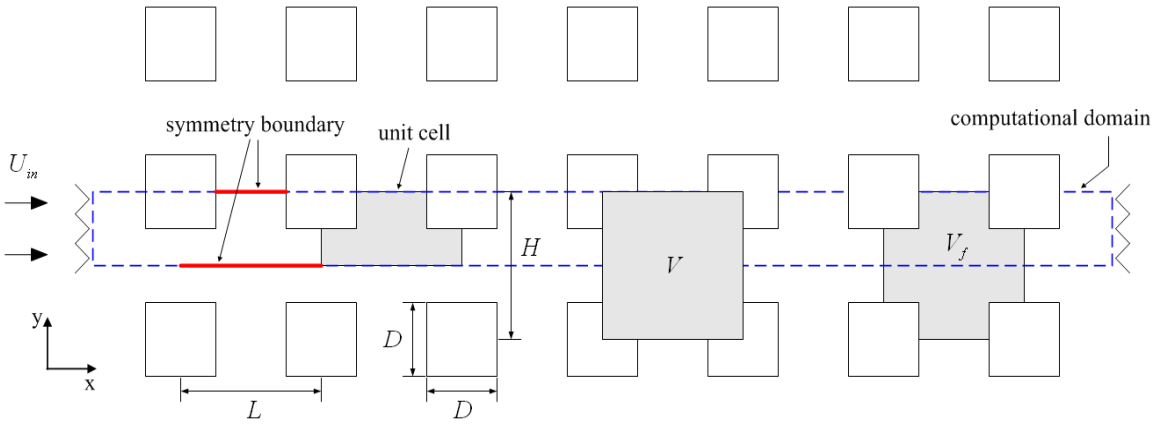

Figure 2.10. Computational domain with boundary conditions [Kim (2008, [44])].

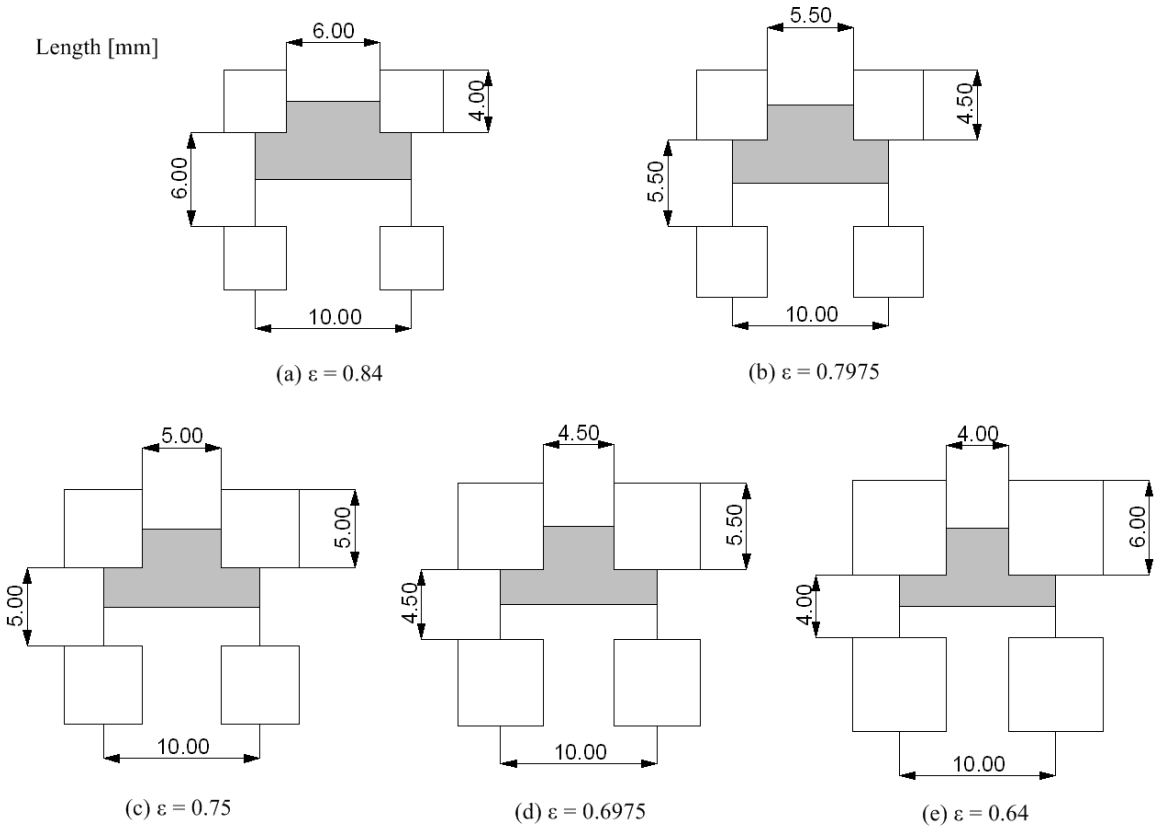

Figure 2.11. Different porous structure geometries showing a unit cell [Kim (2008, [44])].

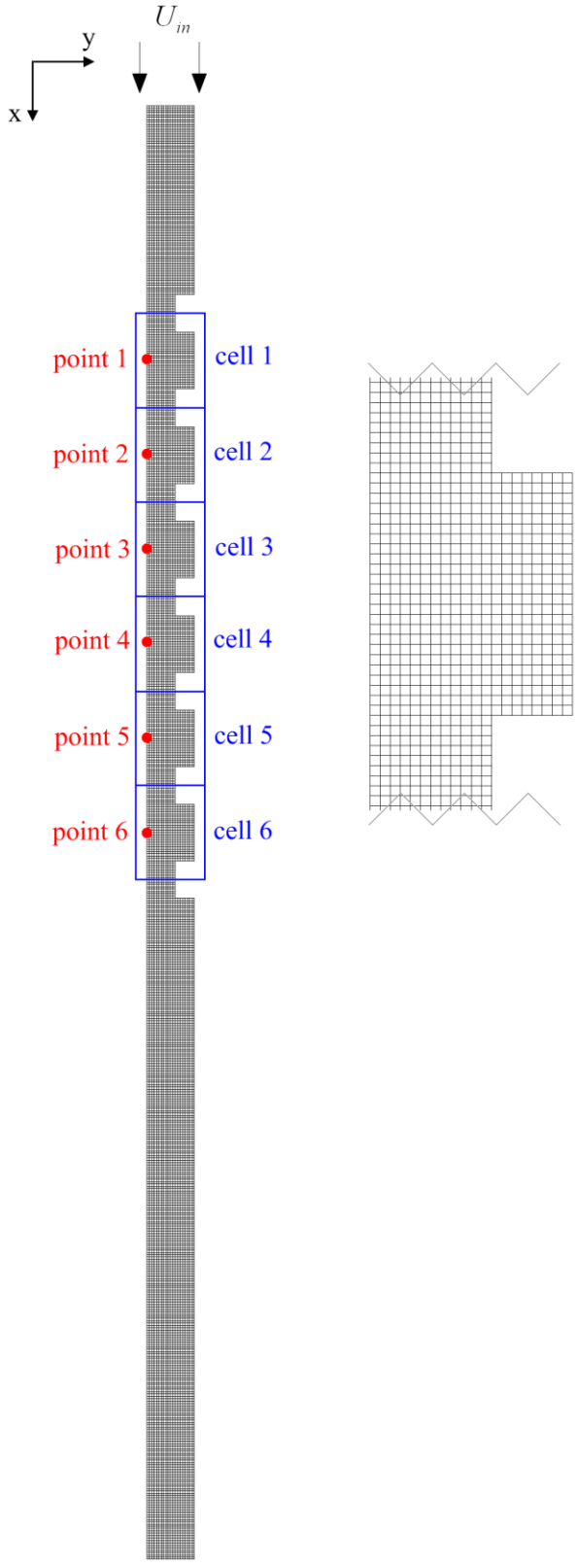

Figure 2.12. Sample grid system [Kim (2008, [44])].

Based on their numerical results, the standard unsteady volume-averaged momentum conservation equation for porous media (Equation 3.7 in Kim (2008, [44])) was then applied in order to obtain the instantaneous as well as cycle-averaged permeability and Forchheimer coefficients. The calculation procedure that they developed to obtain the instantaneous permeability and Forchheimer coefficients was comprised of the following five-step algorithm [Kim (2008, [44])],

" Step 1: obtain the intrinsic volume averaged values of u_i^n *and* p_i^n *at* $i=1$ *to 6, and during* n *time snapshots covering two pulsation cycles from the microscopic-level solution results*

Step 2: solve the following equation for the n *time snapshots covering two pulsation cycles for low-flow simulations, and thereby obtain* $K_{xx,inst}$

$$\rho_f\left(\frac{u_i^n-u_i^{n-1}}{\Delta t}+u_i^n\frac{u_{i+1}^n-u_{i-1}^n}{2\Delta x}\right)=-\frac{p_{i+1}^n-p_{i-1}^n}{2\Delta x}+\mu_f\frac{u_{i+1}^n-2u_i^n+u_{i-1}^n}{\Delta x^2}-\frac{\varepsilon\mu_f}{K_{xx,inst}}u_i^n$$

Step 3: obtain the cycle-averaged permeability coefficient, $K_{xx,avg}$

Step 4: solve the following equation for the n *time snapshots covering two pulsation cycles for high-flow simulations, and thereby obtain* $B_{xx,inst}$

$$\rho_f \left(\frac{u_i^n - u_i^{n-1}}{\Delta t} + u_i^n \frac{u_{i+1}^n - u_{i-1}^n}{2\Delta x} \right) =$$

$$= -\frac{p_{i+1}^n - p_{i-1}^n}{2\Delta x} + \mu_f \frac{u_{i+1}^n - 2u_i^n + u_{i-1}^n}{\Delta x^2} - \frac{\varepsilon \mu_f}{K_{xx,avg}} u_i^n - \varepsilon^2 \rho_f B_{xx,inst} \cdot |u_i^n| u_i^n$$

Step 5: obtain the cycle-averaged Forchheimer coefficient, $B_{xx,avg}$

The u^n, u^{n-1}, *and* p^n *are already calculated values from the microscopic-level equations, thus the instantaneous permeability coefficient* $K_{xx,inst}$ *can be obtained from Step 2. In Step 3, the cycle-averaged permeability coefficient is defined as:*

$$K_{xx,avg} = f \int_{t_o}^{t_o + \frac{1}{f}} K_{xx,inst} dt$$

By substituting $K_{xx,avg}$ *into Equation (29), the instantaneous Forchheimer coefficient* $B_{xx,inst}$ *is numerically calculated from Step 4. Finally, the cycle-averaged Forchheimer coefficient can be obtained from:*

$$B_{xx,avg} = f \int_{t_o}^{t_o + \frac{1}{f}} B_{xx,inst} dt$$ ”

It was found that the cycle-averaged permeability coefficients were nearly the same as those for steady flow, but the cycle-averaged Forchheimer coefficients were about twice larger than those for steady flow. Also, significant phase differences were

observed with respect to the volume-averaged velocity and pressure waves. They found parametric trends representing the dependence of these phase lags on porosity and flow Reynolds number. The phase difference between pressure and velocity waves, which is important for PTC operation, strongly depended on porosity and flow Reynolds number. Figures 2.13-2.14 show some of Kim and Ghiaasiaan's results.

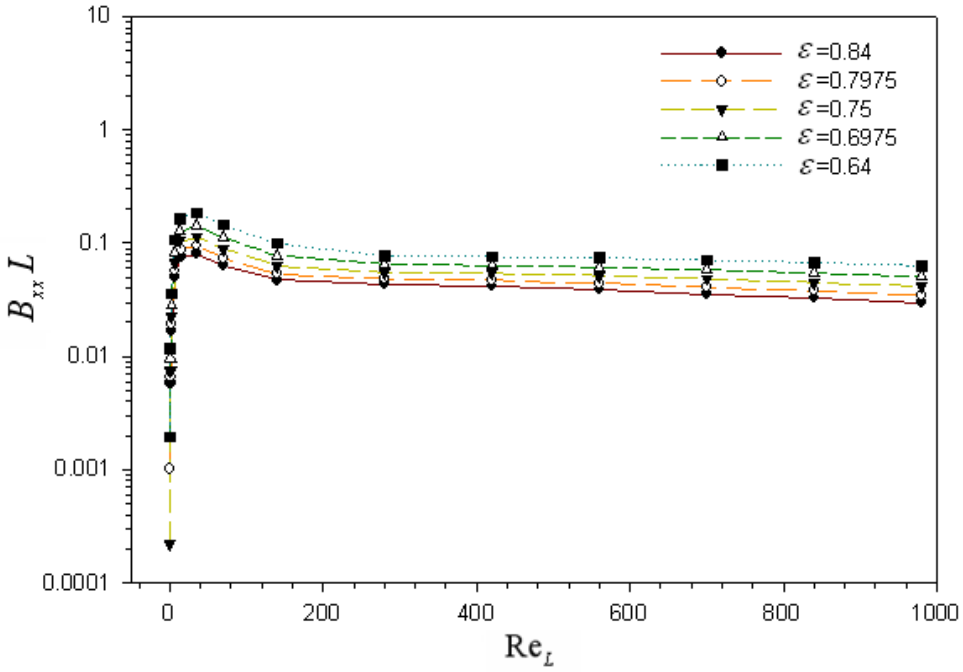

Figure 2.13. Forchheimer term as a function of Reynolds number for the steady flow [Kim (2008, [44])].

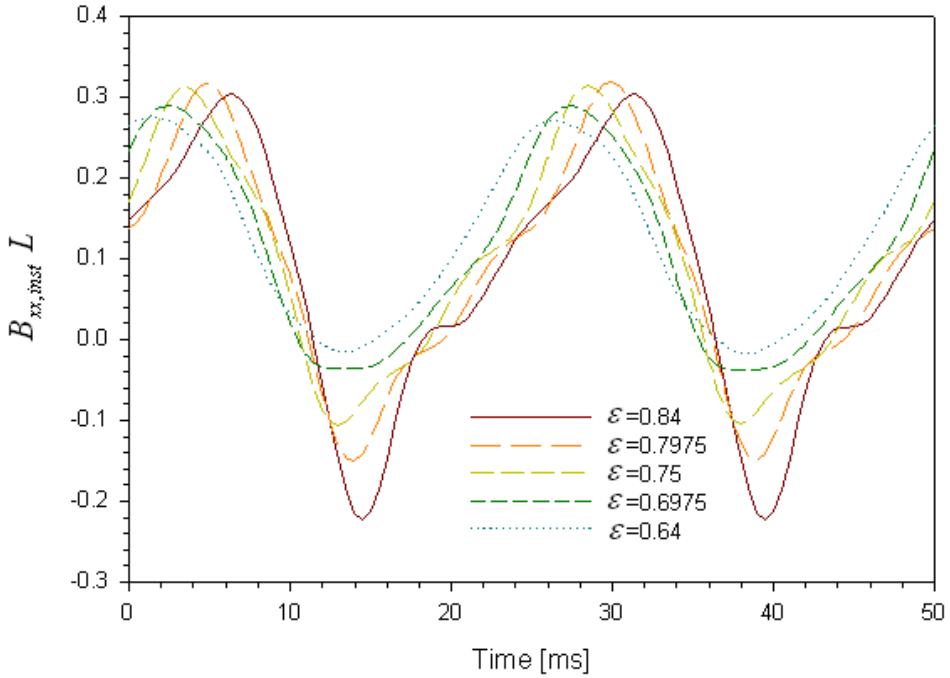

Figure 2.14. Variation of the instantaneous Forchheimer coefficients for different porosities [Kim (2008, [44])].

Recently, Pathak and Ghiaasiaan [Pathak and Ghiaasiaan (2010, [32]), Pathak (2010, [6])], further extended the previous investigation to study the thermal dispersion and heat transfer effects that occur during incompressible laminar pulsating flow within a porous medium. The pore scale heat transfer coefficient and thermal dispersion interactions were examined. They simulated arrays of square cylinders similar to those studied by Kim and Ghiaasiaan [Kim and Ghiaasiaan (2009, [31])], where the porosity was varied by scaling the cylinder diameters. Specialized user defined functions were created to impose a pulsating flow condition and flow simulations were conducted with Fluent [Fluent (2006, [66])], a widely used commercial CFD code. The volume-average mass, momentum, and energy conservation equations were numerically solved, and the average Nusselt number and average dimensionless thermal dispersion were determined.

The computational investigation revealed that the average Nusselt number and the magnitude of the dimensionless thermal dispersion decreased with increasing oscillation frequency for a given unit cell length-based Reynolds number and structure porosity. The instantaneous thermal dispersion conductivity (thermal conductivity defined to replace the thermal dispersion term with an equivalent heat conduction term) was found to vary periodically during each cycle and was found to be orders of magnitude larger than the molecular thermal conductivity of the fluid. Finally, correlations for the cycle- and volume-average (double-averaged) Nusselt number and non-dimensional thermal dispersion term (see Equation 2.14) were derived and compared well with the generated numerical data. Figures 2.15-2.18 show some of their collected results.

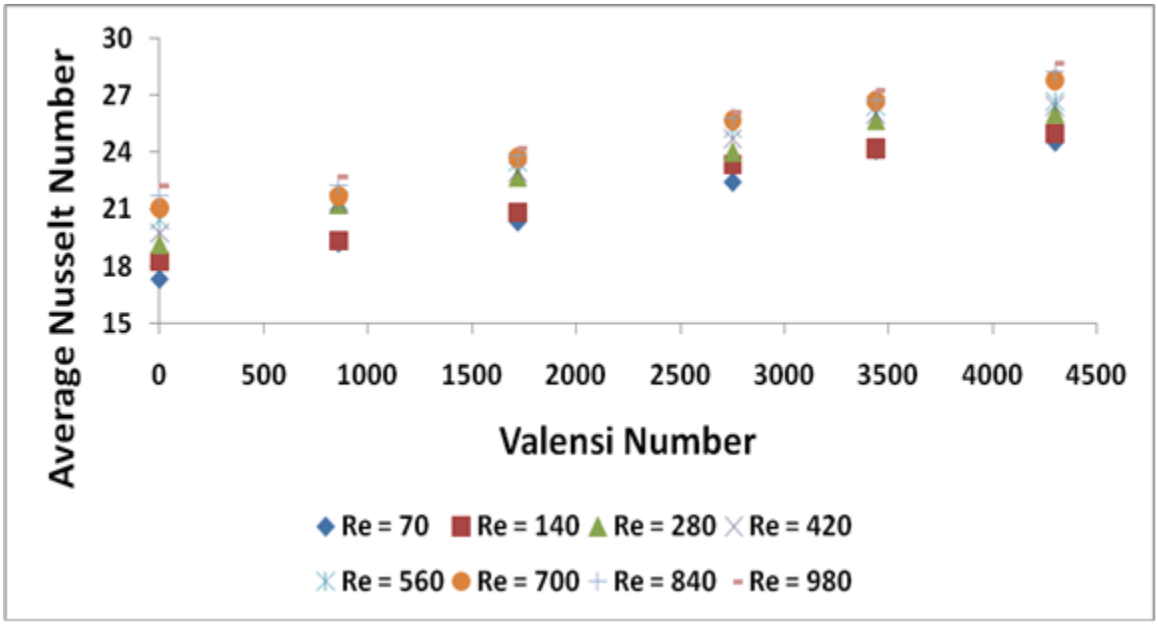

Figure 2.15. 75% porosity – Nusselt number vs. Valensi number [Pathak (2010, [6])].

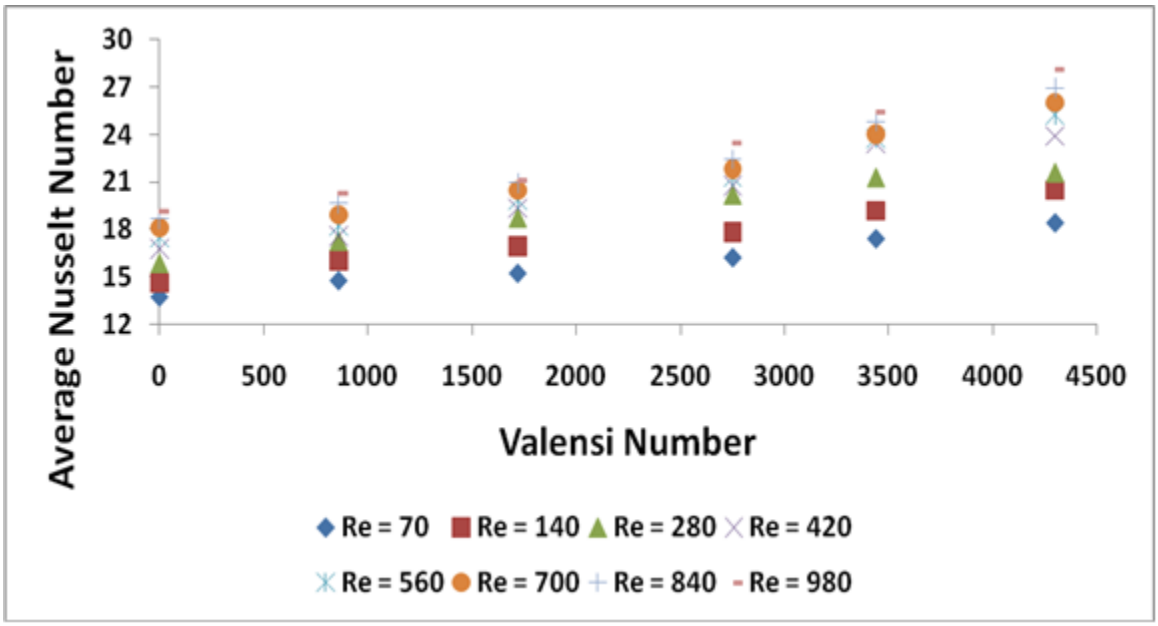

Figure 2.16. 84% porosity – Nusselt number vs. Valensi number [Pathak (2010, [6])].

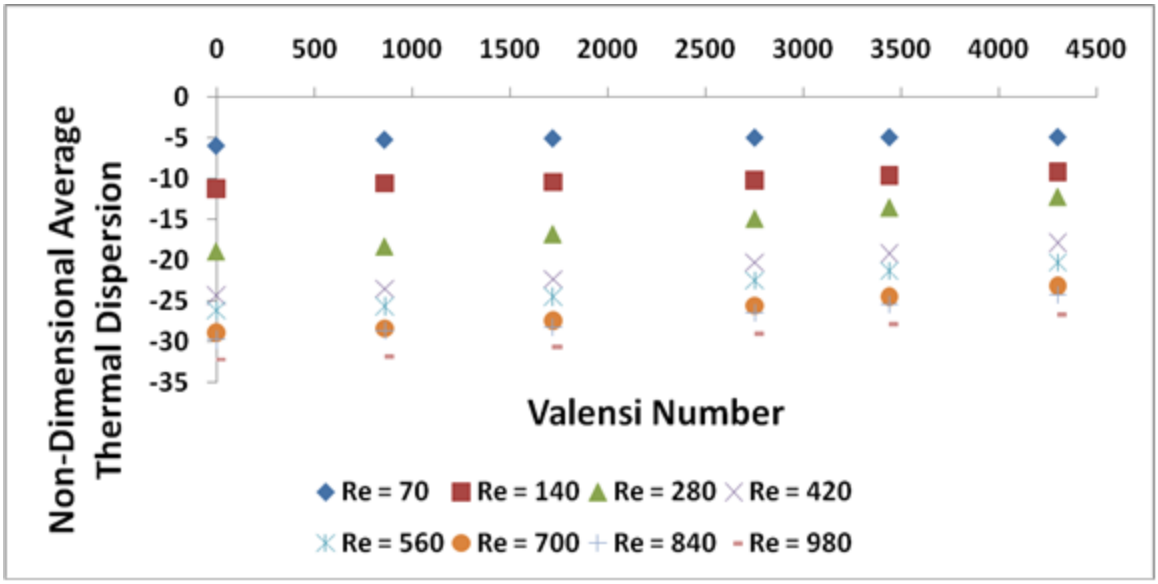

Figure 2.17. 64% porosity – Non-dimensional dispersion vs. Valensi number [Pathak (2010, [6])].

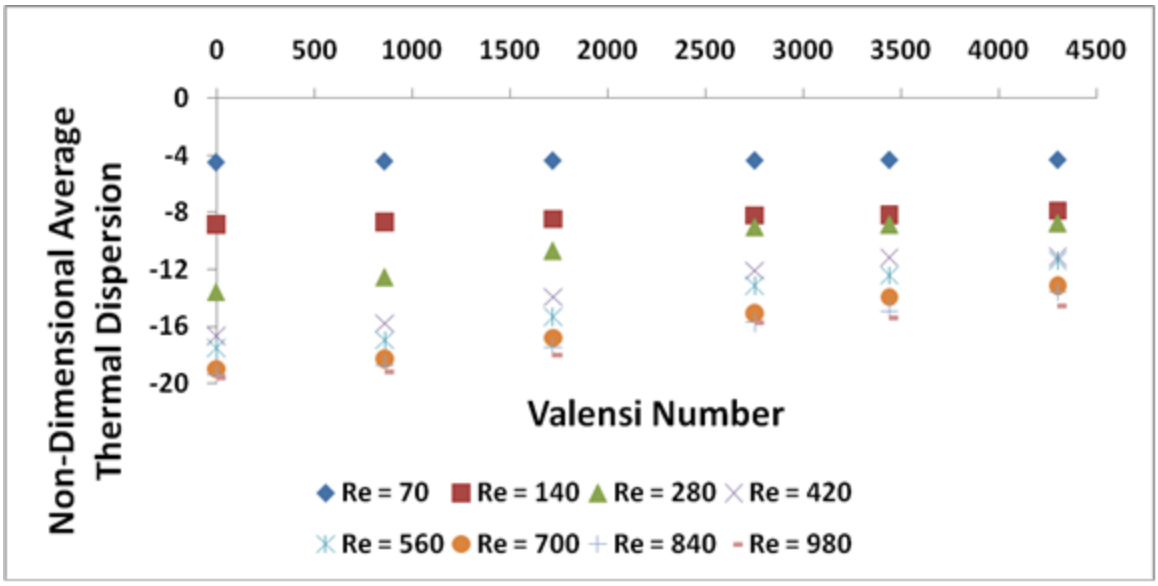

Figure 2.18. 75% porosity – Non-dimensional dispersion vs. Valensi number [Pathak (2010, [6])].

In their study, the thermal dispersion term was non-dimensionalized by writing,

$$D_T^* = \frac{\varepsilon \rho_f c_{pf} \left\langle \tilde{u}_j T \right\rangle^f}{\rho c_p \varepsilon u_{\max} L \left(\left\langle \frac{dT}{dx} \right\rangle \right)} \tag{2.14}$$

This equation compares the thermal dispersion term to the maximum change in stored thermal energy in the fluid as it moves from one unit cell to another. The Valensi number is defined as, $Va = \frac{\omega L^2}{\nu}$, and can be thought of as the ratio of characteristic length to the momentum diffusion length.

More recently, Mulcahey, Pathak, and Ghiaasiaan [Mulcahey et al. (2012, [33])],

studied laminar two-dimensional pulsating flow through homogeneous linear arrays of heated square rods for pulsation frequencies in the range 0 – 80 Hz range and for tube diameter – based Reynolds numbers from 50-200, shown in Figures 2.19-2.21.

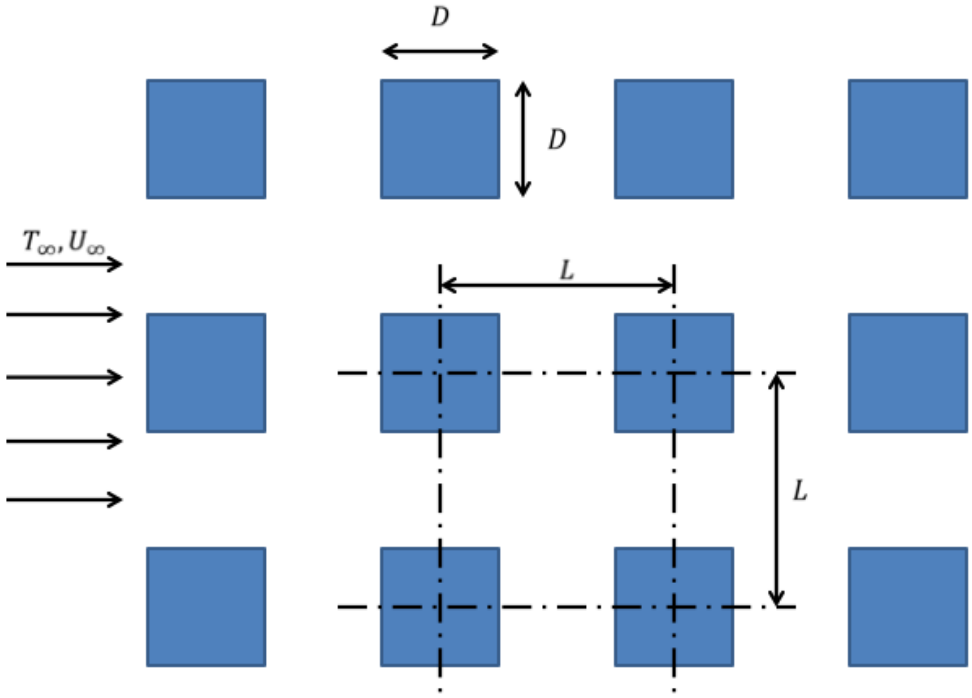

Figure 2.19. Physical configuration of parallel square rods in pulsating flow field [Mulcahey et al. (2012, [33])].

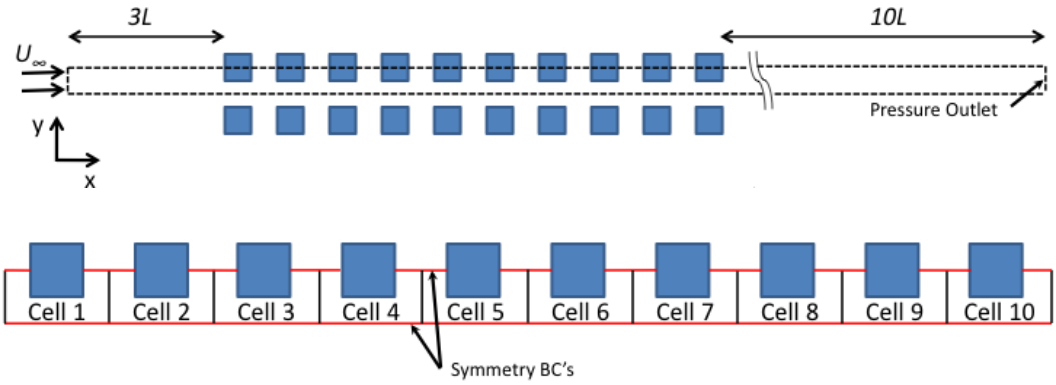

Figure 2.20. Computational domain for simulations [Mulcahey et al. (2012, [33])].

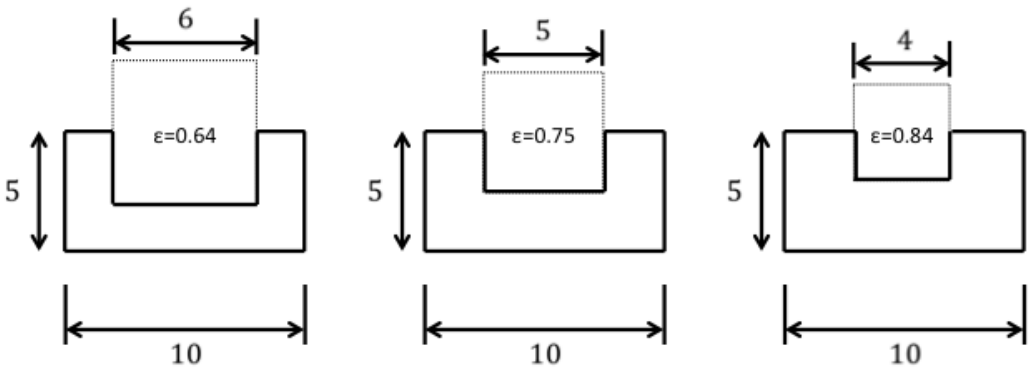

Figure 2.21. Unit cell configurations and dimensions for the porosities simulated [Mulcahey et al. (2012, [33])].

They calculated and analyzed cycle-averaged and maximum drag coefficients, as well as the cycle-averaged Nusselt number for each of the ten rods in the experimental array. In tube arrays subject to steady flow, these parameters are known to depend on the location of a particular tube, and the tubes in the first row typically show the highest Nusselt number and friction factor. Mulcahey et al. [Mulcahey et al. (2012, [33])], derived correlations which relate the maximum and cycle-average drag coefficient as well as Nusselt number to the following parameters: Reynolds number, frequency, porosity (ratio of flow area to total area), and cell (row) number. A wake galloping effect was observed by studying the details of the flow field which significantly amplified the drag on the leading cells while instantaneously reversing the sign of the drag force on the rods located in the wake region. Cycle average drag was found to decrease with increasing Reynolds number and porosity, and was only a weak function of pulsation frequency. Peak drag was found to decrease with increasing Reynolds number and

porosity, but linearly increase with increasing frequency. Nusselt number was also predicted to have an inverse relationship with porosity and a direct relationship with both Reynolds number and frequency. Figures 2.22-2.24 show some collected results.

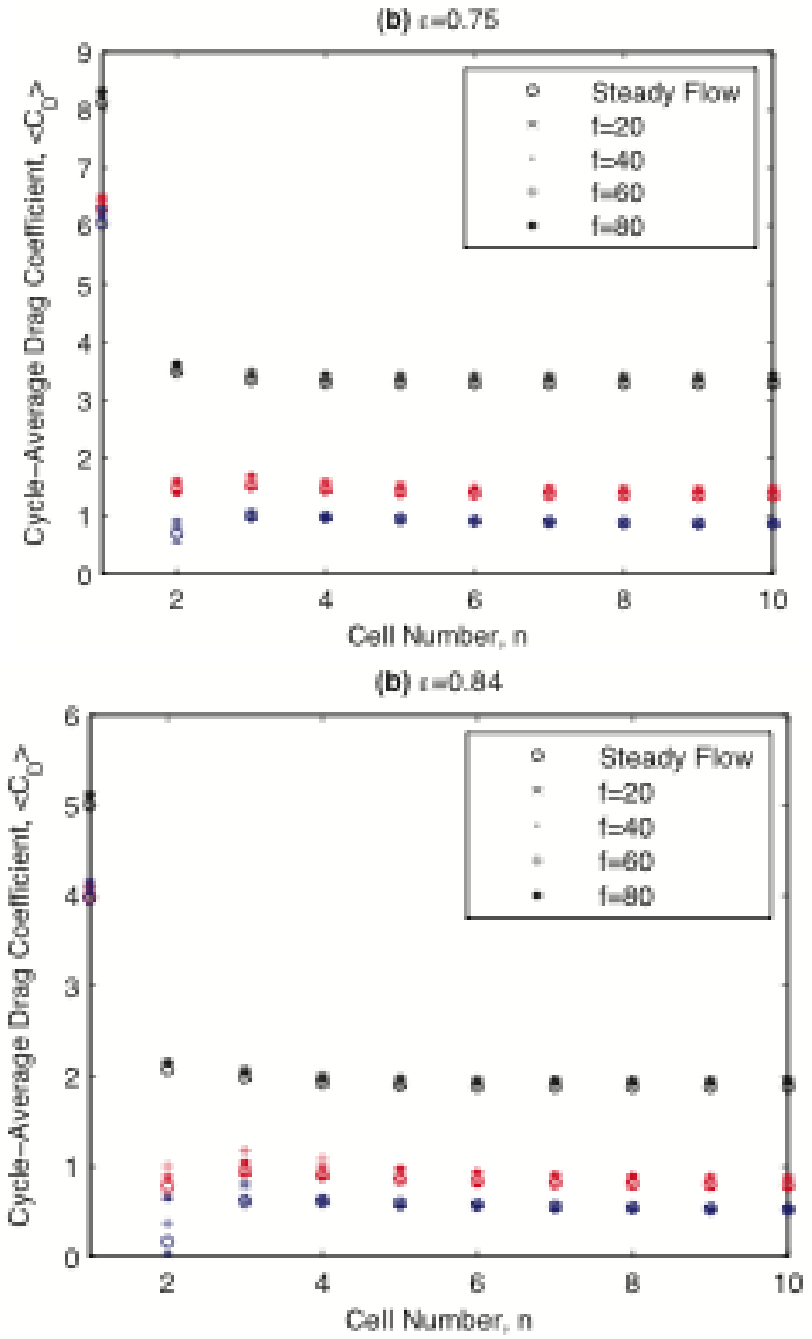

Figure 2.22. Cycle-average drag coefficients by cell [Mulcahey et al. (2012, [33])].

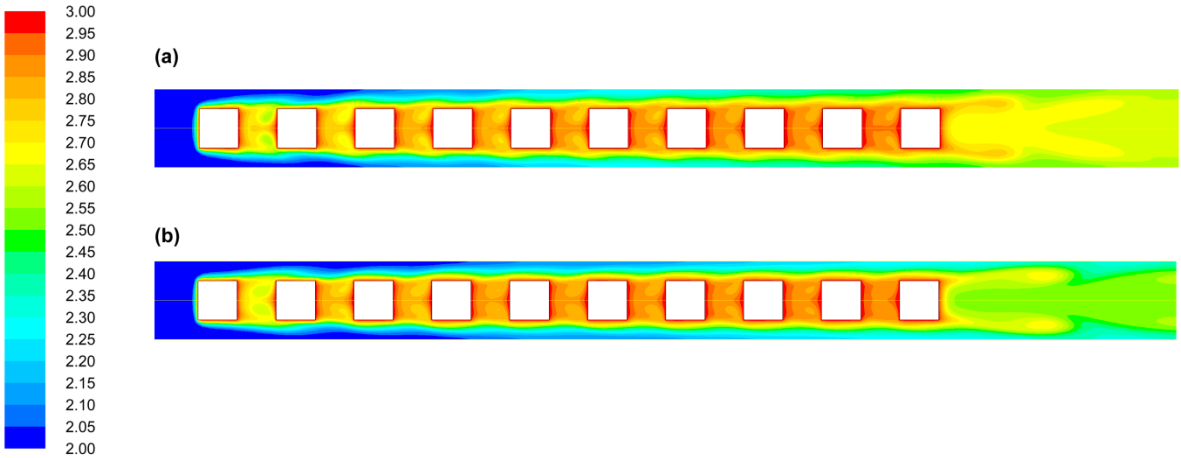

Figure 2.23. Temperature contours for selected cases [Mulcahey et al. (2012, [33])].

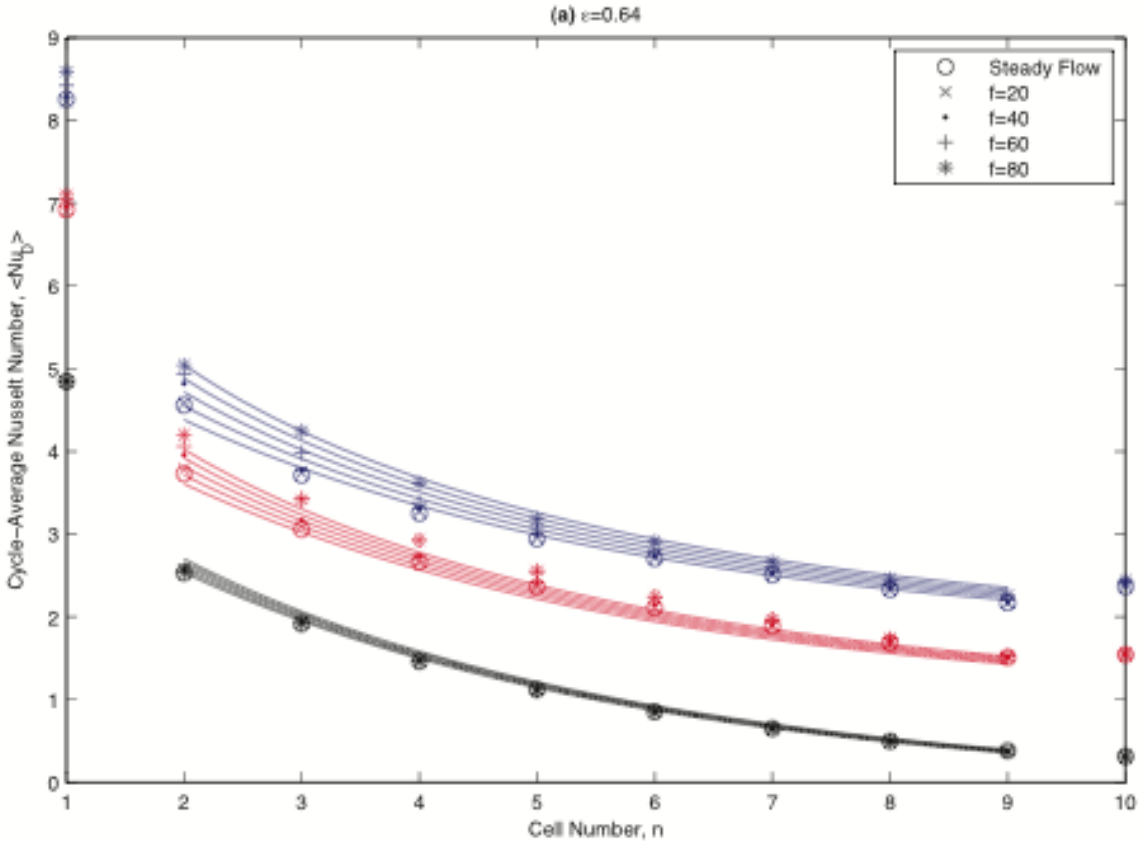

Figure 2.24. Cycle-averaged Nusselt Number [Mulcahey et al. (2012, [33])].

Pathak, Mulcahey, and Ghiaasiaan [Pathak et al. (2012, [67])], extended the pulsating flow studies to periodic flow and investigated the differences between the hydrodynamics and thermal energy of steady state and periodic flow through porous media. Two-dimensional flows in porous media composed of periodically configured arrays of square cylinders were simulated using a computational fluid dynamics tool, with sinusoidal time variation of inlet and exit boundaries and conjugate heat transfer between the solid and fluid domains. Detailed numerical data were obtained for frequencies of 0 ~ 60 Hz, and low and high amplitudes, for a 75% porous domain. Pore-scale volume-average Darcy Permeability, Forchheimer, and Nusselt number associated with the standard volume-average porous media momentum and thermal energy equation were quantified and were found to be significantly different from steady flow to oscillatory flow.

These investigations further prove the usefulness of direct numerical simulations when studying flow and thermal energy phenomena on the pore-scale [Kim (2008, [44]), Pathak (2010, [6])].

2.3 Regenerators

In this section regenerators and their important attributes will be discussed. Modeling methods for the regenerator component, as well as the system-level pulse tube cryocoolers will be deliberated. A description of experimental measurements and corresponding published studies will then follow. The section concludes with the theory and method of determining closure parameters.

2.3.1 General Remarks

Configurations of major PTC designs were discussed earlier in Section 2.1. The regenerator of a PTC presents many design challenges and optimal performance is invariably a compromise among several conditions. Typical regenerators utilize stacks of steel wire mesh screens (at relatively high cold head temperatures) or metal or rare earth beads housed within a thin-walled frame. A major problem with regenerators is that the filler material must have a large specific heat and large thermal conductivity in the lateral direction (Large thermal conductivity in the axial direction is detrimental to the performance of the regenerator). The large thermal conductivity can be satisfied by using metallic fillers. However, the specific heats of the metals decrease sharply as very low temperatures are approached. Recent developments show that the application of multilayer regenerators comprised of several materials can take better advantage of temperature dependent thermal properties [Radebaugh and Gully (2008, [5])]. The regenerator structure must provide a large heat capacity for thermal storage and the necessary surface area for optimal heat transfer between the working fluid and solid matrix. The associated rate of heat transfer is dependent on many factors including operating frequency, pore size, and charge pressure. At steady-periodic state, one end of the regenerator may be at an ambient temperature condition while the other end is at cryogenic temperatures. As a result, the regenerator must minimize axial conduction across large temperature gradients and reduce hydrodynamic impedance or pressure drop within its porous medium.

The pulse tube component operates by transferring enthalpy in an oscillating system across and up a temperature gradient while minimizing hydrodynamic losses and

entropy generation. The magnitude of this hydrodynamic flow work is dependent upon the phase angle between the volumetric flow rate and dynamic pressure. Because of this harmonic relationship, enthalpy flow is non-uniform throughout the pulse tube. The optimal operational situation involves the mass flow at the cold end of the pulse tube to lag the pressure while the flow at the warm end of the pulse tube leads the pressure. Gas displacements within the tube must be relatively small to effectively insulate the two ends and axial conduction in the pulse tube shell must be minimized. Mitigation of turbulence (which causes mixing and disrupts the axial thermal stratification) and acoustic streaming are also essential for effective operation.

The heat exchangers in a PTC function by transferring thermal energy between the PTC working fluid (usually helium) and the external environment. Highly conductive materials such as copper alloys are employed in the exchanger matrix to maximize radial conduction. Heat exchangers also act as flow straighteners to produce a plug-flow regime within the pulse tube. Like the regenerator, they are usually composed of wire mesh bundles. Desired cooling loads are typically adjoined to the cold head via a thermal bus.

2.3.2 Regenerator and System-Level Studies

As mentioned earlier, a number of design tools have been developed in the recent past to simulate the working processes governing PTCs. These tools include, in order of rigor and complexity, lumped-capacitance methods, one-dimensional numerical tools [Gedeon (2009, [68])], and CFD codes. Recent successful CFD models [Cha (2007, [11]), Cha et al. (2006, [53]), Conrad et al. (2008, [69])] of cryocooler systems have shown that such models can provide very useful performance predictions for cryocoolers. For miniature cryocoolers, CFD modeling is likely the best technique available as models developed for larger systems may not accurately represent phenomena which become

important as the device scale is reduced. Detailed CFD modeling of Stirling and pulse tube refrigerators of course requires realistic closure relations, particularly with respect to the hydrodynamic and thermal transport processes for the porous media which make up their heat exchangers and regenerators. Recent studies [Cha (2007, [11]), Clearman (2007, [49])] present useful experimental data and correlations for some common regenerator fillers.

It should be emphasized that without direct pore-level simulation, the macroscopic conservation equations which govern fluid flow through the porous media require empirical momentum closure parameters, and experimental data is needed for the development of these empirical correlations [Cha (2007, [11])]. These empirical correlations include the aforementioned Darcy permeability and Forchheimer's inertial coefficient which are needed for the closure of macroscopic momentum conservation equations [Landrum (2009, [4])]. Ideally, heat transfer coefficients that can be used to predict thermal non-equilibrium in regenerators are also needed. Reliable correlations for predicting such heat transfer coefficients are not available at this time, however, and local thermal equilibrium is often assumed.

Many analytical and computational models of pulse tube refrigerators have been developed as part of the ongoing research effort to improve the performance of cryocoolers. Examples of each popular model types are now introduced.

Analytical models of Stirling and pulse tube cryocoolers often involve some form of control volume method [Nika and Bailly (2002, [70])]. In order to accurately represent actual systems, these models are equipped with empirical parameters. They are useful for providing information about parametric dependencies and are applied as design tools, however these analytical approaches inherently neglect the details of the flow inside the modeled systems. Information about these flow details is necessary to assess the effects of several of the previously discussed phenomena.

A better approach, in comparison with the aforementioned simple analytical models involves computational models specifically developed for PTCs. These models are generally one-dimensional and based on solutions of the differential fluid conservation equations at component boundaries and axially distributed nodes. Widely used models of this type include REGEN code published by NIST [Gary et al. (2008, [71])], and Gedeon and Associate's SAGE [Gedeon (2009, [68])]. REGEN is a state-of-art regenerator development and modeling code that solves the fluid and solid conservation equations using the finite-difference method. It is equipped with property libraries for more than 30 regenerator filler materials, and is used for geometric and thermodynamic optimizations. The code correctly calculates a multitude of parameters (enthalpy and entropy flows, efficiency, etc.). REGEN is a one-dimensional stand-alone code, however. It is used for design purposes in tandem with other tools that represent other PTC components.

SAGE is a modular, hierarchical modeling program, which is assembled to represent the steady-periodic performance of Stirling or pulse tube cryocoolers in their entirety on a full-scale system level. It has detailed, one-dimensional models for various components of Stirling or pulse-tube cryocoolers, and is used for system-level and component-level optimization.

One-dimensional computational models have also been developed at the Los Alamos National Laboratory (LANL) (DeltaE, [Ward and Swift (1994, [72])]). More recently, Kashani and Roach, from NASA Ames Research Center, developed a computer program known as ARCOPTR [Kashani and Roach (1997, [73]), Kashani and Roach (1998, [74])]. This program utilizes the 1-D fluid mass, momentum, and energy conservation equations to simulate the thermo-fluidic processes in the regenerator along with the entire cooler. However, this program was only limited to small mass flows and small pressure and temperature oscillations.

Ju et al. [Ju et al. (1998, [75])], in a one dimensional simulation modeled the entire orifice and double-inlet PTCs, by using a common set of fluid conservation equations everywhere. The friction factor and heat transfer coefficients were chosen to be the larger among relevant laminar and turbulent correlations everywhere, however.

A common feature of the aforementioned regenerator models is that they assume that the working fluid and the solid porous matrix in the regenerator are everywhere at thermal equilibrium. However, Harvey [Harvey (2003, [42])] has recently developed a 1-D regenerator model based on the volume averaged method. He solved the model differential equations using the method of lines. The model by Harvey uses the best available closure relations as of 2002 for the 1-D conservation equations. A major distinction between the model by Harvey and other models published in the open literature is that Harvey's model is capable of accounting for thermal non-equilibrium between the working fluid and the solid structure in the regenerator. The selected hydrodynamic correlations, however, are primarily based on steady state literature dealing with purely axial flow in the porous media of interest [Cha (2007, [11])].

The analytical tools discussed above are all one-dimensional. Experiment and detailed CFD analyses show that one-dimensional flow assumptions are an appropriate approximation, at least for PTCs that are linearly configured and are made of components with large aspect ratios. However, multi-dimensional flow effects occur at certain applications and localities even in linear PTCs, for example at the vicinity of component interphases, in components with small aspect ratios, and when chamfering is used. Multi-dimensional flow effects are also inevitable in co-axial or U-shaped cryocoolers. These one-dimensional models miss multi-dimensional flow details, however, and their predictions should be considered as scoping analyses when significant deviations from one-dimensional flow configurations are involved.

Computational Fluid Dynamics (CFD) is a modeling technique used to solve the differential conservation equations for mass, momentum, and energy on a computational

grid. This grid is actually a discretized representation of an entire two- or three-dimensional model domain. Two-dimensional, axisymmetric models are most commonly used for linear PTC simulation. Recent successful CFD simulations of system-level and component-level cryocoolers have provided fairly accurate performance predictions for pulse tube refrigerators [Conrad et al. (2008, [69]), Taylor et al. (2008, [76]), Zhang et al. (2007, [77]), Flake and Razani (2004, [78]), Nachman et al. (2009, [79])]. Among the pioneers of CFD simulation of PTCs in their entirety, Cha et al. [Cha et al. (2004, [80])] examined the adequacy of pulse tube cryocoolers being modeled as one-dimensional flow fields. To test this, they modeled and tested two entire inertance tube pulse tube refrigerator systems which were operating under various thermal boundary conditions using the aforementioned Fluent computational fluid dynamics code [Ansys Fluent (2011, [81])]. They were able to prove that a one-dimensional analysis is adequate when all components of the inertance tube pulse tube refrigerator have a large length to diameter ratio.

Virtually all of these PTC simulations have been performed with Ansys Fluent, a commercial CFD package capable of producing detailed solutions of models involving complex geometries [Ansys Fluent (2011, [81])]. It performs steady-state or transient solutions to problems that involve a variety of flow phenomena, including flow in porous media. Available Fluent functions can be enhanced by using user defined functions (UDFs) in order to add or modify closure relations and incorporate custom boundary conditions.

These codes: REGEN, SAGE, and Fluent are employed to design and study both system-level and pore-level thermal and hydrodynamic processes.

2.3.3 Experimental Studies

As mentioned earlier, PTC regenerators are microporous structures that are subject to periodic flows of cryogens. The literature dealing with flow in porous media is indeed vast. However, the discussion in this section will be restricted to studies specifically addressing flow and heat transfer in PTC regenerators.

Cha et al. [Cha et al. (2008, [82])] reported on the measurement and correlation of anisotropic hydrodynamic parameters of the most widely used cryocooler regenerator fillers. They tested stainless steel 400 and 325 mesh screens, stainless steel 400 mesh sintered filler, stainless steel sintered foam metal, and nickel micro-machined disks. A CFD assisted methodology was used for the analysis and interpretation of their measured data. They were able to compare the magnitudes of oscillatory flow friction factors to steady flow friction factors at particular Reynolds number values for each of the regenerator fillers. Their results are presented in Figure 2.25. For this figure, the Reynolds number is defined according to Equation 2.15 and the friction factor for one dimensional flow in an isotropic porous medium is related to the Darcy permeability and Forchheimer coefficient according to Equation 2.16.

$$\mathrm{Re}_{\beta_j} = \frac{\rho |\vec{u}| \beta_j^{0.5}}{\mu} \tag{2.15}$$

$$f_j = \frac{2}{\mathrm{Re}_{\beta_j}} + C_j \beta_j^{0.5} \tag{2.16}$$

Figure 2.25 indicates that for the porous structures studied, for Re>0.1 the steady-flow and periodic flow friction factors are different.

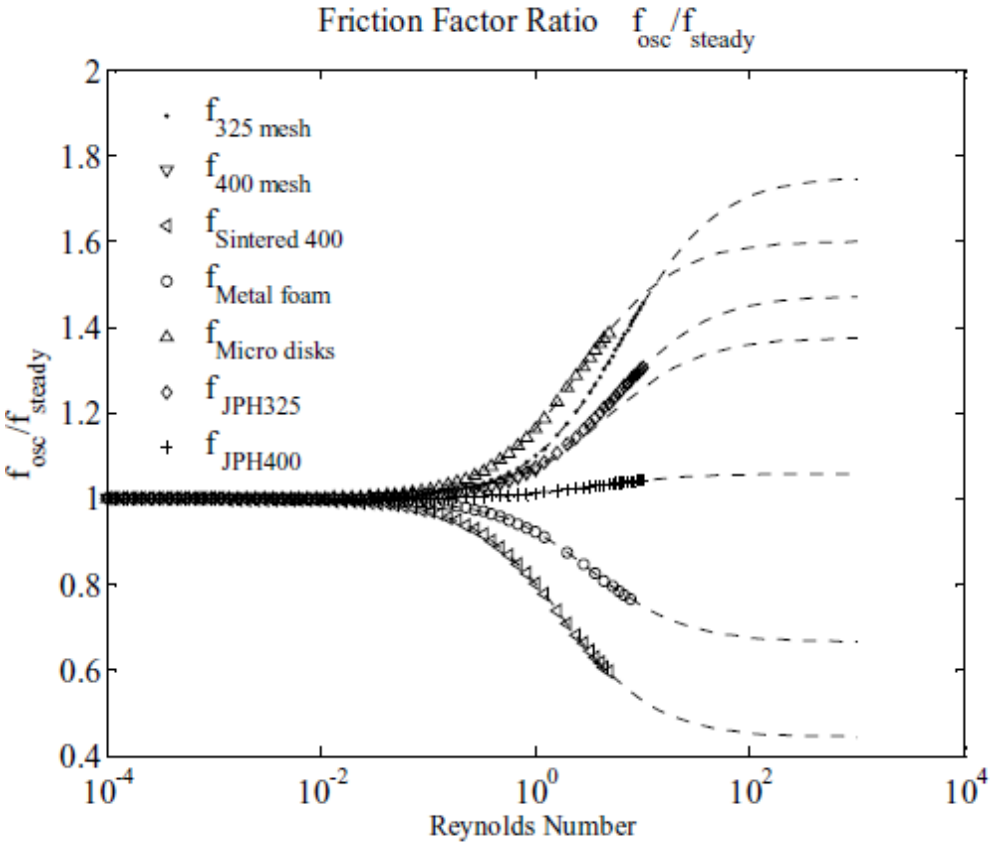

Figure 2.25. Friction factor study [Cha et al. (2008, [82])].

Harvey [Harvey (2003, [42])] studied various regenerator filler materials including, wire mesh, perforated disk, and foam metal, shown in Figure 2.26. He concluded that oscillating flow situations produced larger friction factors relative to steady flow cases.

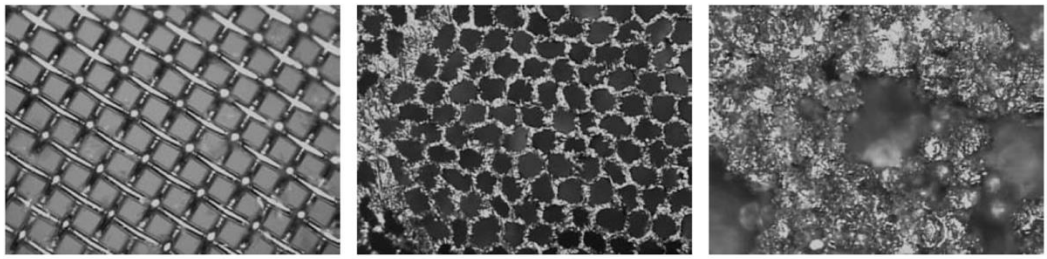

Figure 2.26. Regenerator fillers: wire mesh (left), perforated disk (middle), foam metal (right) [Harvey (2003, [42])].

.

Clearman [Clearman (2007, [49])] also measured and correlated the hydrodynamic parameters associated with steady longitudinal and radial flow of helium in many widely-used pulse tube and Stirling cryocooler regenerator fillers. They determined that for 325 mesh screens, a higher porosity results in a lower relative pressure drop within the regenerator.

Cha's [Cha (2007, [11])] investigation was aimed at the: a) experimental measurement and correlation of the steady and periodic flow directional Darcy permeability and Forchheimer's inertial hydrodynamic parameters for some widely-used regenerator fillers; b) system-level parametric CFD-based analyses of entire PTC systems; and c) a preliminary CFD-based assessment of the effect of direct and linear scale-down of current inertance tube PTCs (ITPTCs) on their thermal performance.

He performed separate effects tests where pressure drops in axial and lateral directions were measured on regenerator fillers including 325 mesh stainless steel screens, 400 mesh stainless steel screens, sintered 400 mesh stainless steel screens, stainless steel metal foam, and stacked nickel micro-machined disks. The parametric effects that were addressed included porosity in the range of 26.8% to 69.2%, and frequency in the range of 5 Hz to 60 Hz for the periodic flow tests. A CFD-assisted method was developed, which allowed for obtaining the directional permeability and

Forchheimer coefficients from the experimental data in a rigorous manner and without any arbitrary assumption. Figures 2.27-2.30 show Cha's experimental test apparatus.

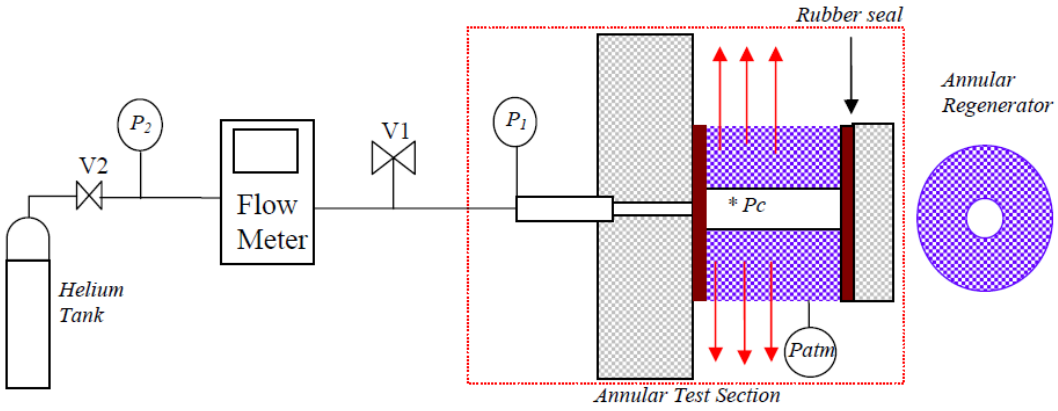

Figure 2.27. Radial pressure drop test apparatus for steady flow [Cha (2007, [11])].

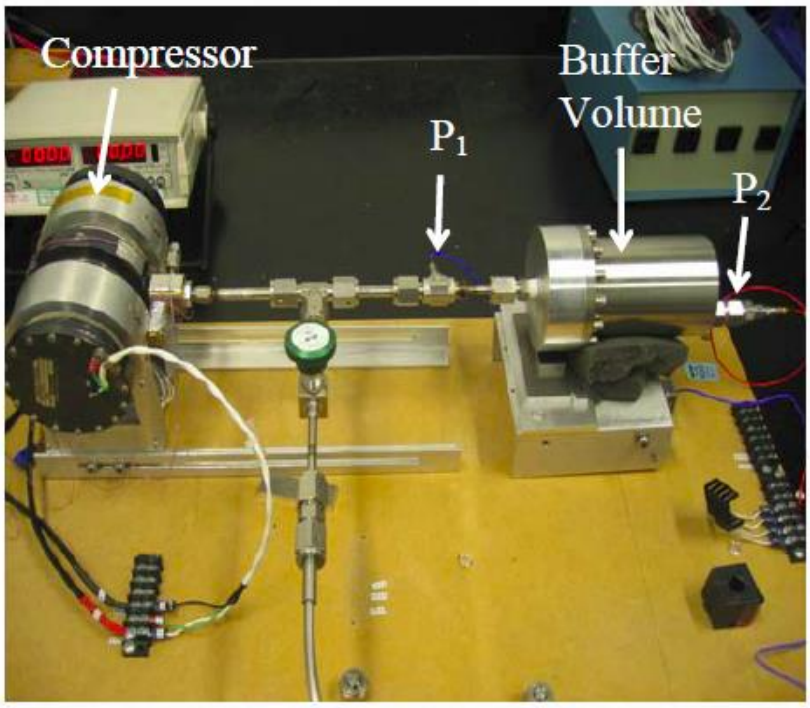

Figure 2.28. Radial pressure drop test apparatus for oscillatory flow [Cha (2007, [11])].

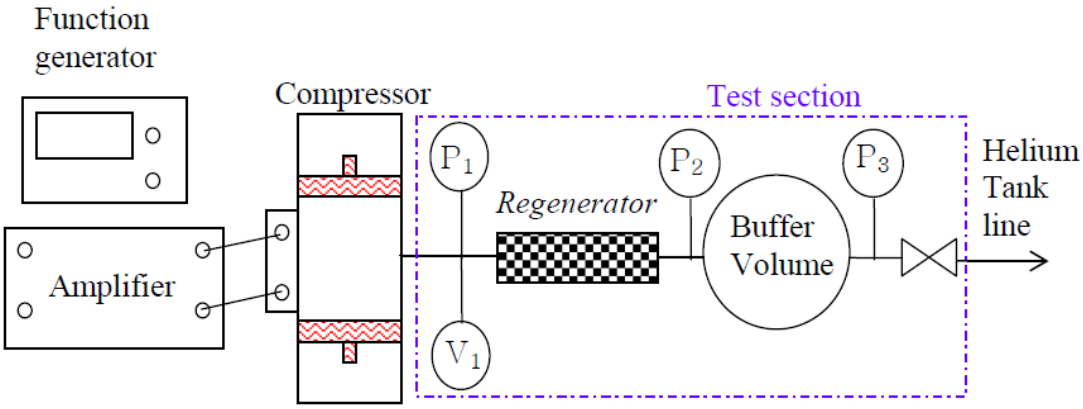

Figure 2.29. Axial pressure drop test apparatus for oscillatory flow [Cha (2007, [11])].

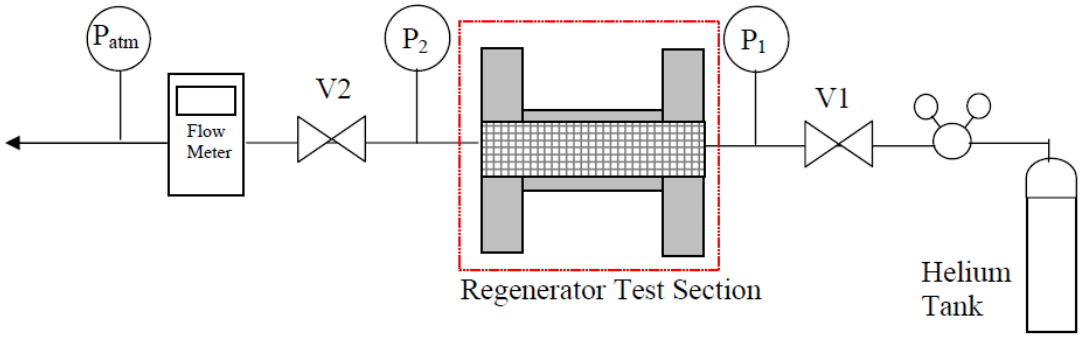

Figure 2.30. Axial pressure drop test apparatus for steady flow [Cha (2007, [11])].

The hydrodynamic and thermal performances of the 5 tested regenerator filler matrices were then simulated using a CFD tool. It showed that the hydrodynamic parameters representing steady flow were in general different from the hydrodynamic parameters associated with periodic flow.

The effect of direct miniaturization on the performance of a linearly-configured ITPTC system was also examined in a preliminary, CFD-assisted analysis. It was shown that direct and linear miniaturization, when all the dimensions of a current conventional scale ITPTC system are proportionately reduced, leads to significant deterioration of the performance of the cryocooler. A summary of Cha's results are shown in Table 2.2.

Table 2.2. Summary of Cha's results [Cha (2007, [11])].

IPTPC Model	Oscillatory Friction Factor					Steady Friction Factor				
HX1 Wall [°K]	293	293	293	293	293	293	293	293	293	293
HX2 Wall [°K]	293	293	293	293	293	293	293	293	293	293
Regenerator Type	325 Mesh	400 Mesh	400 Mesh Sintered	Foam Metal	Micro-machined Disks	325 Mesh	400 Mesh	400 Mesh Sintered	Foam Metal	Micro-machined Disks
Regenerator Material	Stainless Steel	Stainless Steel	Stainless Steel	Stainless Steel	Nickel	Stainless Steel	Stainless Steel	Stainless Steel	Stainless Steel	Nickel
β [m^2]*	6.4247 E-11	2.5295 E-11	1.9828 E-11	3.7689 E-11	4.0000 E-11	4.2553 E-11	3.6101 E-11	1.8018 E-11	3.7736 E-11	4.3478 E-11
C [1/m]*	67000	120000	110000	66000	192000	47000	73000	260000	99000	115000
Regenerator Porosity	0.692	0.692	0.6147	0.5547	0.268	0.696	0.696	0.6147	0.5547	0.268
CHX, HX1, and HX2 material	Copper	Copper	Copper	Copper	Copper	Copper	Copper	Copper	Copper	Copper
β_c [m^2]	1.345 E-9	1.345 E-9	1.345 E-9	1.345 E-9	1.345 E-9	1.345 E-9	1.345 E-9	1.345 E-9	1.345 E-9	1.345 E-9
C_c [1/m]	8147	8147	8147	8147	8147	8147	8147	8147	8147	8147
CHX, HX1 and HX2 Porosity	0.68	0.68	0.68	0.68	0.68	0.68	0.68	0.68	0.68	0.68
Initial CHX Temperature [°K]	300	300	300	300	300	300	300	300	300	300
CHX LOAD (W)	0	0	0	0	0	0	0	0	0	0

Landrum [Landrum (2009, [4])] determined the hydrodynamic parameters of two of the best commercially available mesh filler materials suitable for miniature PTCs - stacked screens of #635 stainless steel and #325 phosphor-bronze wire mesh cloth. The results indicate large differences between the directional hydrodynamic resistance parameters for steady and oscillating flow regimes. Figures 2.31-2.32 show his results.

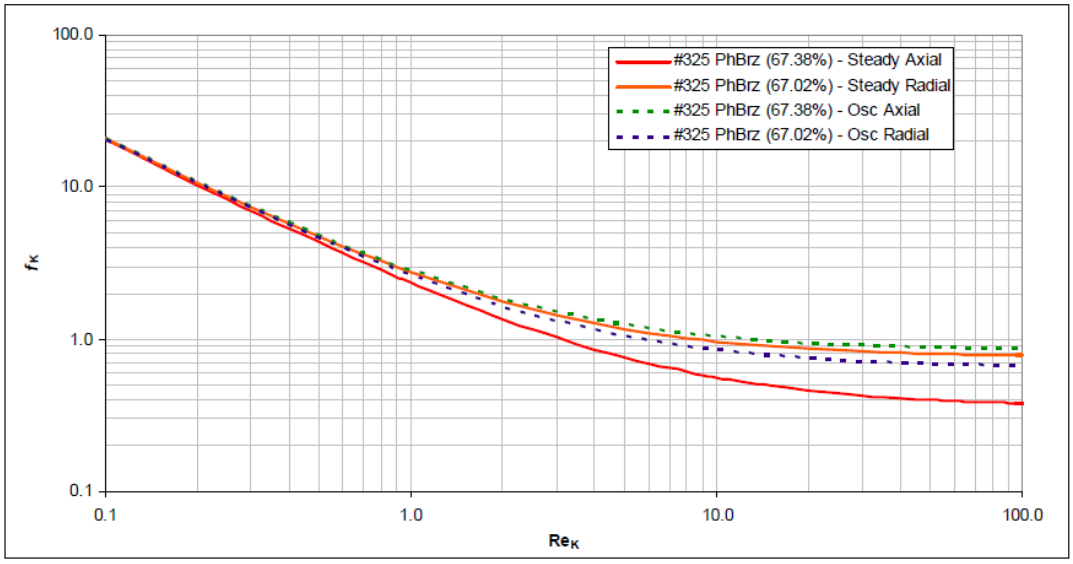

Figure 2.31. Friction factor plot for #325 phosphor bronze [Landrum (2009, [4])].

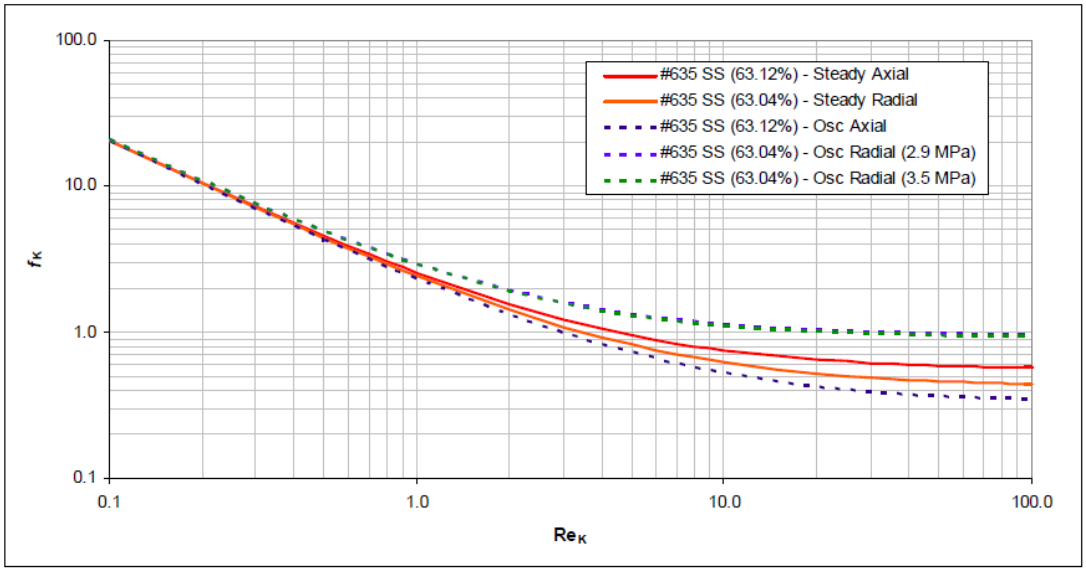

Figure 2.32. Friction factor plot for #635 stainless steel [Landrum (2009, [4])].

Conrad [Conrad (2011, [15])] performed a similar study to Landrum [Landrum (2009, [4])], where he also determined the hydrodynamic parameters mesh filler materials - stacked screens of #635 stainless steel and #325 phosphor-bronze wire mesh cloth.

Pathak et al. [Pathak et al. (2013, [83])] conducted experiments in which laminar steady and oscillatory flows of helium were imposed on $Er_{50}Pr_{50}$ rare-Earth regenerator filler material and mass flow and pressure drop data were recorded under ambient temperature conditions. They selected a filler material composed of 63 to 75 μm diameter $Er_{50}Pr_{50}$ spheres based on current commercially available particle geometries. A computational fluid dynamic (CFD)-assisted method was applied for the analysis and interpretation of the experimental data, with sinusoidal time variations of inlet and exit boundary conditions for the periodic flow case. The permeability and inertial coefficients that led to agreement between the experimental data and computational simulations were iteratively obtained. A constant permeability value for all steady and periodic flow tests was found and correlated well to experimental data. The Forchheimer inertial coefficients were correlated and found to be functions of the system charge pressure and the pore-based Reynolds number. The results also show that the periodic flow inertial coefficients are different than the steady flow parameters typically used.

Many other researchers have also studied the role of regenerators in cryocooling systems because of the effect they have on the entire cryogenic system performance, including [13, 15, 49, 56, 84-94]: Nam and Jeong, 2007; Clearman, 2007; Cha, Ghiaasiaan, and Desai, 2006; Sahoo and Das, 1994; Guo et al., 1987; Erk and Dudukovic, 1997; Bubnovich, and Gonzalez, 2005; Ogawa et al., 1990; Willmott, 1964; Hua and Zhong, 1988, Radebaugh et al., 2002; de Waele and Zeegers, 2002; Yuan and Jing-Tao, 2002; Popescu et al., 2001; and Conrad 2011. Although the findings of the above investigators have led to new product development and important regenerator insights,

the pore scale phenomena for transient flow through a regenerator has yet to be understood.

CHAPTER 3

EXPERIMENTAL METHODOLOGY

In this chapter the experimental methodology and test apparatus design, setup, and test procedures are discussed. The section opens with a description of the tested regenerator section and its corresponding characteristics. Specifications of both the steady flow tests and periodic flow tests are then discussed. Finally, the chapter concludes with a discussion on the uncertainty associated with the experiments.

3.1 Regenerator Characteristics

Figure 3.1 shows the $Er_{50}Pr_{50}$ rare Earth regenerator filler that was studied in this investigation along with the regenerator test section. The filler was made of near-spherical pellets with an average diameter of 69 μm and a porosity of 38%. These particles cover a size range of 63 to 75 μm diameter. The $Er_{50}Pr_{50}$ powder filled a cylindrical regenerator space of 2.3 cm in diameter and 5.08 cm in length. This regenerator test section was used for both the steady and periodic flow experiments. Table 3.1 shows a summary of the tested regenerator in both flow tests.

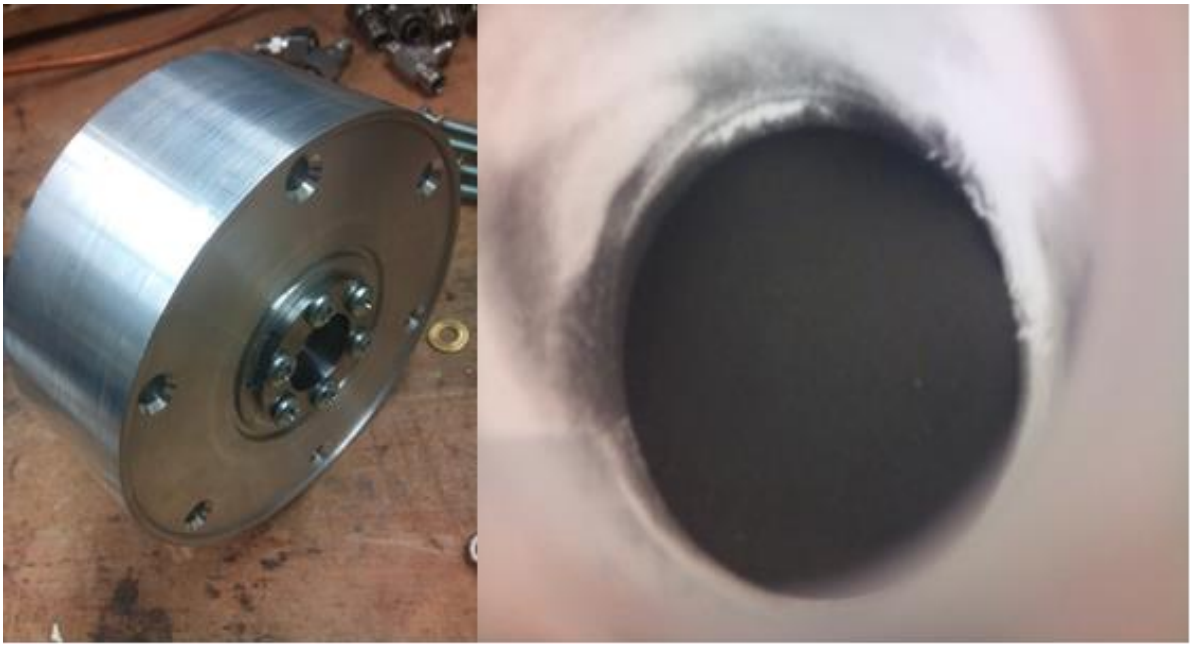

Figure 3.1. Regenerator test section (left) and ErPr Filler Material (right). *Courtesy of Atlas Scientific (San Jose, CA) and NASA Ames Research Center (Moffett Field, CA).

Table 3.1. Summary of tested regenerators.

Regenerator Material	$Er_{50}Pr_{50}$ rare Earth
Porosity	0.38
Filler Geometric Type	Spherical pellets
Filler Particle Size	63 to 75 µm,
Average Filler Particle Size	69 µm
Regenerator Diameter	2.3 cm
Regenerator Length	5.08 cm

The common approach for constructing a regenerator is to load it with a stack of screen sheets or other filler material (spherical pellets, foam metal, etc.), and adjust its porosity by properly packing the stack. As a result of the stacking, the hydraulic resistance of the porous structure in axial and lateral direction will vary. In light of the randomness of the stacking process for various fillers, and the average spherical diameter in the pellets, the porous structures can be assumed to be isotropic. The $Er_{50}Pr_{50}$ pellets were provided by Atlas Scientific (San Jose, CA) and the construction of the regenerator was done at NASA Ames Research Center (Moffett Field, CA).

There are several factors that lead to the selection of regenerator filler material for various pulse tube cryocoolers. These factors include thermo-physical properties, manufacturability, cost, toxicity, and life cycle. In this investigation $Er_{50}Pr_{50}$ spherical pellets were chosen because, of the materials considered (Figure 3.2), spherical Er_{50}-Pr_{50} particles were determined to be the best candidate material, due to the material exhibiting the largest volumetric heat capacity at very low operating temperatures, specifically within the temperature range of 18 K – 22 K. Spherical particle geometry was selected because of the ability of spherical pellets to achieve very low temperatures [Radebaugh et al. (2009, [95])] and because hydrodynamic and heat transfer properties of packed beds composed of spherical pellets are well known. Relative to lead (~$0.15/gram) and other metal fillers, which were historically used in low temperature PTCs, Er_{50}-Pr_{50} is considered to be more expensive (~$1/gram), however, it has many benefits. Er_{50}-Pr_{50} is a rare Earth material which is non-toxic unlike certain metallic materials, can be manufactured quite easily, has good thermal performance, and its proven operational life cycle is significantly higher than metallic materials. Also, along with a high volumetric heat capacity, erbium is ductile, oxidation resistant, has low thermal conductivity, and high tensile strength. Further, Er_{50}-Pr_{50} exhibits a density that is ~20% less than most metals, resulting in less mass needed to make a similar sized regenerator and in turn reduces the load on the overall cryocooler, making Er_{50}-Pr_{50} ideal for regenerators with

operating temperatures between 8 K to 80 K [Wysokinski et al. (2002, [96])]. Lower payload masses and higher efficiency cryocoolers are critical for space, aerospace, and defense based thermal management applications.

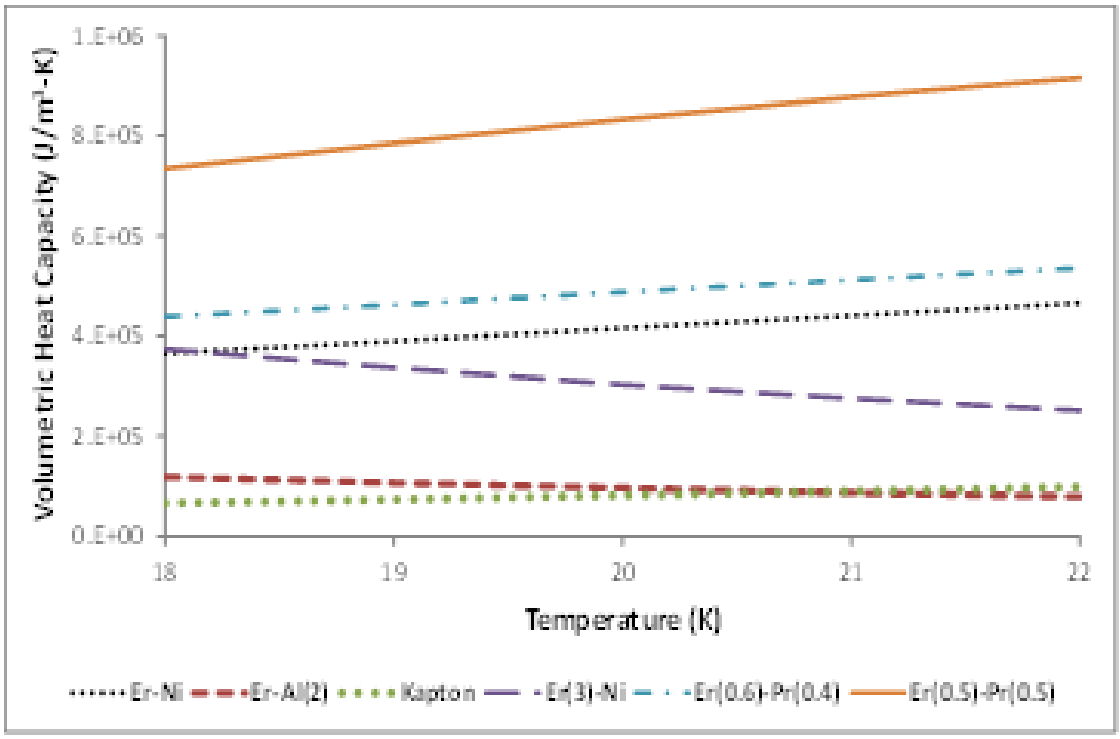

Figure 3.2. Filler material volumetric heat capacity at low temperatures [Gary et al. (2008, [71])].

3.2 Apparatus and Test Matrix for Steady Flow

The test apparatus for the measurement of the steady flow hydrodynamic characteristics of the regenerator Er_{50}-Pr_{50} rare Earth material is schematically displayed in Figure 3.3.

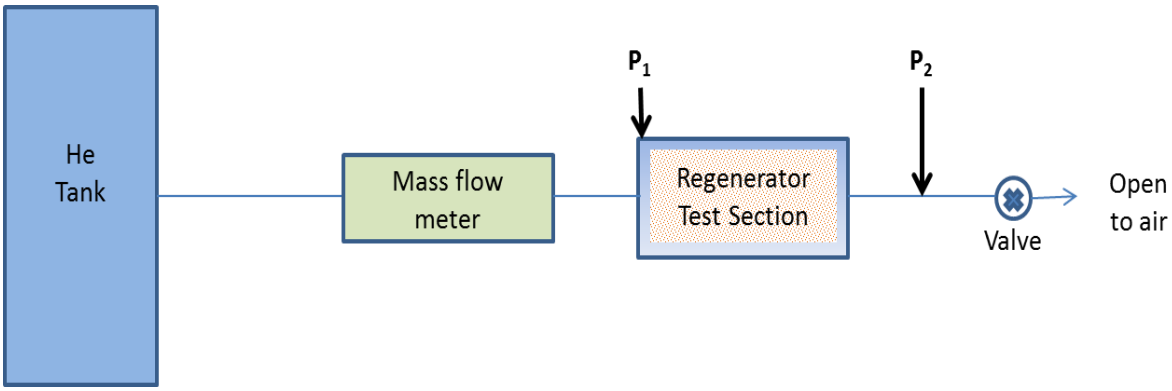

Figure 3.3. Schematic of steady flow apparatus.

The steady flow test apparatus includes, a mass flow meter, two Omega PX94 pressure transducers, an Omega FMA 1700/1800 mass flow meter, and a specially designed module that houses the porous structure sample, as described in the previous section.

The working fluid in all the tests was research grade helium with a nominal purity of 99.9999%. The regenerator test section was designed and fabricated at NASA Ames Research Center. It includes a specially designed regenerator housing module that has flange type end-connections, O-ring seals, and flange type connecting components. The test section had an inner diameter of 2.3 cm and length of 5.08 cm. The regenerator module was used for all of the tests.

Two PX94 pressure transducers (from Omega, 0-300 psi model) measured the local instantaneous pressures. A mass flow meter (from Omega, model FMA 1700/1800) was used to measure the local instantaneous velocities at the inlet of the regenerator.

A total of 59 steady flow tests were conducted, shown in Table 3.2, covering a mass flow rate range of 4.3E-5 to 8.7E-4 kg/s at a charge pressure range of 0.345 MPa to 1.724 MPa. This was done by manually adjusting the valve such that the flow rate of

interested could be reached. In each test, the local pressures at the inlet and exit of the regenerator and the regenerator inlet velocity were measured. The steady-state pressures at P_1 and P_2, and the mass flow rate were recorded. All the tests were performed at ambient room temperature.

Table 3.2. Summary of steady flow tests.

Case	P_{charge}**(Pa)**	$\dot{m}$**(kg/s)**
1	3.45E+05	4.33E-05
2	3.45E+05	8.66E-05
3	3.45E+05	1.73E-04
4	3.45E+05	1.95E-04
5	3.45E+05	2.08E-04
6	5.17E+05	8.66E-05
7	5.17E+05	1.73E-04
8	5.17E+05	2.60E-04
9	5.17E+05	3.46E-04
10	5.17E+05	4.24E-04
11	6.89E+05	8.66E-05
12	6.89E+05	1.73E-04
13	6.89E+05	2.60E-04
14	6.89E+05	3.46E-04
15	6.89E+05	4.33E-04
16	6.89E+05	5.19E-04
17	6.89E+05	6.06E-04

18	6.89E+05	6.92E-04
19	6.89E+05	7.10E-04
20	8.62E+05	8.66E-05
21	8.62E+05	1.73E-04
22	8.62E+05	2.60E-04
23	8.62E+05	3.46E-04
24	8.62E+05	4.33E-04
25	8.62E+05	5.19E-04
26	8.62E+05	6.06E-04
27	8.62E+05	6.92E-04
28	8.62E+05	7.79E-04
29	8.62E+05	8.66E-04
30	1.03E+06	8.66E-05
31	1.03E+06	1.73E-04
32	1.03E+06	2.60E-04
33	1.03E+06	3.46E-04
34	1.03E+06	4.33E-04
35	1.03E+06	5.19E-04
36	1.03E+06	6.06E-04
37	1.03E+06	6.92E-04
38	1.03E+06	7.79E-04
39	1.03E+06	8.66E-04
40	1.38E+06	8.66E-05
41	1.38E+06	1.73E-04

42	1.38E+06	2.60E-04
43	1.38E+06	3.46E-04
44	1.38E+06	4.33E-04
45	1.38E+06	5.19E-04
46	1.38E+06	6.06E-04
47	1.38E+06	6.92E-04
48	1.38E+06	7.79E-04
49	1.38E+06	8.66E-04
50	1.72E+06	8.66E-05
51	1.72E+06	1.73E-04
52	1.72E+06	2.60E-04
53	1.72E+06	3.46E-04
54	1.72E+06	4.33E-04
55	1.72E+06	5.19E-04
56	1.72E+06	6.06E-04
57	1.72E+06	6.92E-04
58	1.72E+06	7.79E-04
59	1.72E+06	8.66E-04

3.3 Apparatus and Text Matrix for Periodic Flow

The test apparatus for the periodic flow experiments is much more complicated compared to the test apparatus for steady flow experimentation. In periodic flow

experiments, the entire working fluid is contained in a leak free, hermetically-closed chamber, and the working fluid, typically helium gas, undergoes a periodic series of compressions and expansions through oscillating pressure waves. The entire periodic flow test apparatus is schematically shown in Figure 3.4.

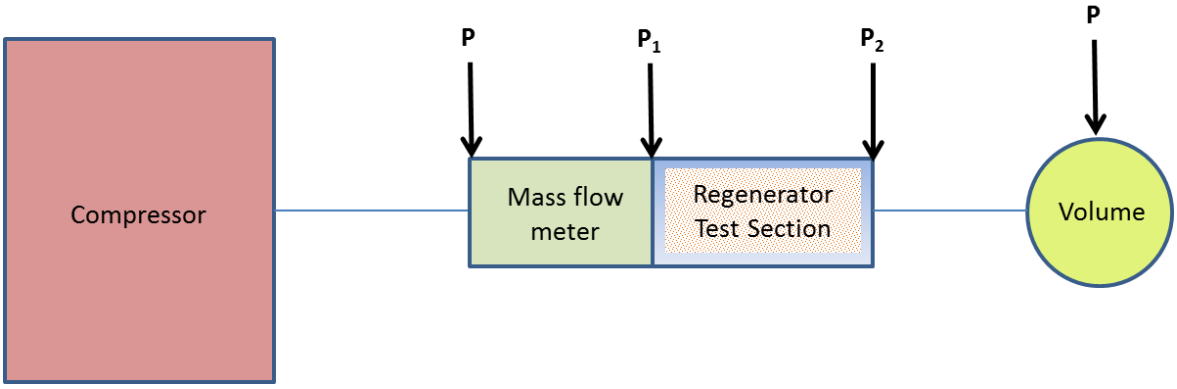

Figure 3.4. Schematic of periodic flow apparatus.

The oscillatory flow test apparatus includes a compressor, a dynamic mass flow meter, several pressure transducers, a buffer volume, and a specially designed module that houses the porous structure sample. A 4 kW CFIC compressor is used to impose oscillatory flow. The aforementioned regenerator module and research grade helium as the working fluid were used for all of the tests, as described in the previous sections. Three PCB piezo transducers (model 401A, from PCB Piezotronics) and one PX94 (mentioned in previous section) pressure transducer measured the local instantaneous pressures. An in-house (developed at NASA Ames Research Center) built dynamic mass flow meter was used to measure the mass flow rate at the inlet of the regenerator.

A total of twenty four periodic flow tests were conducted, shown in Table 3.3, covering the frequency range 30–70 Hz at charge pressures of 1.034 MPa and 1.724

MPa. In each test, the time histories of local instantaneous pressures at the inlet and exit of the regenerator and the buffer volume were recorded under steady-periodic conditions. The time variation of regenerator inlet mass flow rate was also measured along with the piston displacement in the compressor. In all of the tests, the peak-to-peak sinusoidal voltage amplitude was first increased until either the maximum compressor piston displacement or the maximum current limit was reached. The voltage amplitude was then maintained constant and the steady-periodic pressures at P_1 and P_2 and the mass flow rate were recorded. All the tests were performed at ambient temperature.

Table 3.3. Summary of periodic flow tests.

Case	P_{charge} **(Pa)**	f **(Hz)**	**Piston Amplitude (mm)**
1	1.03E+06	30	1.68
2	1.03E+06	30	2.03
3	1.03E+06	30	2.43
4	1.03E+06	30	3.16
5	1.03E+06	40	3.06
6	1.03E+06	40	3.58
7	1.03E+06	50	3.07
8	1.72E+06	30	1.27
9	1.72E+06	30	1.54
10	1.72E+06	30	1.77
11	1.72E+06	30	2.29
12	1.72E+06	30	2.83
13	1.72E+06	40	2.19

14	1.72E+06	40	2.46
15	1.72E+06	40	2.83
16	1.72E+06	40	3.51
17	1.72E+06	50	1.96
18	1.72E+06	50	2.34
19	1.72E+06	50	3.10
20	1.72E+06	50	3.88
21	1.72E+06	70	1.89
22	1.72E+06	70	2.48
23	1.72E+06	70	3.05
24	1.72E+06	70	3.62

3.4 Determination of Hydrodynamic Closure Parameters

Macroscopic measurements for periodic flow in PTC components (separate-effects tests), most importantly in the regenerator, are relatively routine. Extracting closure parameters that can be used in CFD simulation of such flows from these experimental data is not straightforward, however. A methodology for extracting hydrodynamic closure parameters from separate-effects tests has been developed and demonstrated. CFD models of the regenerator test sections and their vicinities are developed in this method and simulations are performed in which the regenerator test sections were modeled as porous media. By iterative repetition of the simulations, the longitudinal and radial permeability and Forchheimer inertial coefficients were

determined such that they would lead to agreement between experimental measurements and the simulations [Cha (2007, [11]), Clearman (2007, [49]), Landrum et al. (2009, [97])].

The following procedure, originally developed by Cha et al. [Cha et al. (2008, [82])], will be employed for the tested regenerator filler in this investigation. Recall that our regenerator filler is made of near-spherical particles with two different sizes that are randomly mixed, and is therefore homogeneous and isotropic. As such, the following relations apply:

$$K = \varepsilon^2 \beta \tag{3.1}$$

$$c_f = \frac{CK^{0.5}}{2\varepsilon^3} \tag{3.2}$$

For periodic flow, first, the case of 30 Hz (i.e., lowest frequency) at the lowest charge pressure and piston amplitude, was simulated by iteratively adjusting the viscous resistance coefficient β without including the inertial effect (C = 0) until the simulation predictions at P1 matched the experimental data. Since the effect of the inertial coefficient is nearly negligible at low velocities, the lowest flow case was chosen to determine the viscous resistance. Subsequently the 70 Hz case, which had the largest piston amplitude and charge pressure, was simulated. This time however, only the inertial coefficient C was iteratively adjusted while β was kept constant until good agreement was obtained between the P1 predictions and experimental data. Using the determined value of C, β was again iteratively adjusted to determine a new β for the 30 Hz, lowest piston amplitude case. This was done in order to determine a valid C for the lowest flow case. Simulations were then performed for all the measured frequencies. If good agreement was obtained for all frequencies then iterative simulations would end, otherwise β and C would be further adjusted iteratively to match the experiment data. A similar procedure was employed for steady flow where the lowest charge pressure, lowest

flow rate case was tested to determine the viscous resistance coefficient, without including the inertial effect. Then the largest charge pressure, largest flow rate case was used to determine the corresponding inertia resistance coefficient while borrowing the viscous resistance term from the aforementioned low flow case. Once determined, the low flow case was iteratively adjusted to find a valid *C*, and then the β term was further adjusted to better match the experimental data and simulation results. It should be mentioned, however, that at this point in both steady flow and periodic flow cases, only minor adjustments to *C* were needed to match all the experiment data and simulation results to reasonable accuracy, while β was found to be constant for both steady flow and periodic flow cases. All the iterative adjustments were performed manually [Pathak et al. (2013, [83])].

3.5 Uncertainty in Experiments

The uncertainty in the results stems from the accuracy of the sensors associated with the experimental flow tests. To calculated uncertainty, the steady-flow Forchheimer Equation, which is an extension of Darcy's Law, was used along with error propagation analysis, represented by,

$$\frac{\Delta p}{L} = \frac{\mu}{K\rho A}\dot{m} + \frac{c_f}{\sqrt{K}\rho A^2}\dot{m}^2 \tag{3.3}$$

$$\sigma_{c_f}{}^2 = \sigma_{P_{in}}{}^2 + \sigma_{P_{out}}{}^2 + \sigma_{\dot{m}}{}^2 \tag{3.4}$$

Substituting the sensor variable partial differential equations and associated sensor uncertainties into Equation 3.2, the full form uncertainty equations can be represented by writing,

$$\sigma_{c_f}{}^2 = \left(\frac{\partial c_f}{\partial P_{in}} U_{P_{in}}\right)^2 + \left(\frac{\partial c_f}{\partial P_{out}} U_{P_{out}}\right)^2 + \left(\frac{\partial c_f}{\partial \dot{m}} U_{\dot{m}}\right)^2 \quad (3.5)$$

where,

U_x = associated uncertainty of the corresponding sensor, x

When calculating the uncertainty of the experiments, the fluid properties and test section geometry were held as constants and only the collected variables from the apparatus sensors were used in Equation 3.3.

A sample plot to show the effect of uncertainty on the derived c_f values, which is discussed in the forthcoming sections, is shown in Figure 3.5.

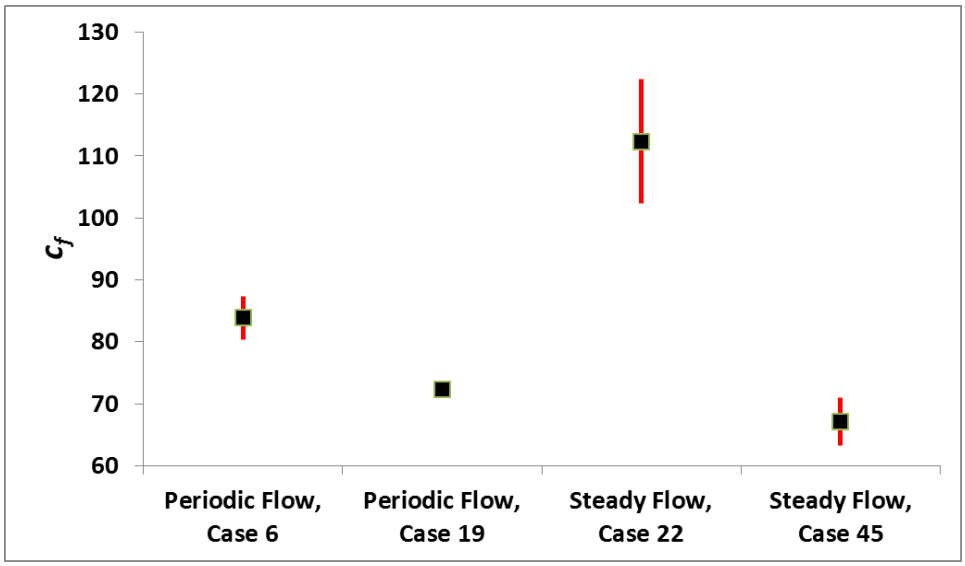

Figure 3.5. Effect of uncertainty on c_f values.

CHAPTER 4

MODELING AND SOLUTION METHODS

This chapter describes the basic modeling and solution methods that were used for simulating and interpreting the regenerator filler experiments, and the pore-level study. The continuum-based conservation equations for basic single-phase fluid flow and heat transfer in open and porous media are first presented. Two exact solutions for one dimensional flow pressure drop across a regenerator are then derived and presented. Finally, the method applied for CFD modeling for the pore-level study and the regenerator filler study are presented and discussed.

4.1 Computational Fluid Dynamics (CFD) Modeling and Governing Equations

CFD simulations in this study were performed using the Ansys Fluent [Ansys Fluent (2011, [81])] code package. Fluent is a well-known and widely-used computer program for modeling fluid flow and heat transfer processes in complicated engineering and physics problems. Fluent offers the flexibility of meshing complex geometry and solving complicated two-dimensional and three-dimensional problems. Transient flow and transport phenomena in porous media, two-phase flow, laminar and turbulent flow, and volumetrically-generating sources can all be modeled by Fluent. Fluent numerically solves the entire continuum fluid and energy equations with no arbitrary assumptions. Although Fluent's basic conservation equations and numerical solution methods are not accessible to users for modification or manipulation, the code allows the users to develop their own subroutines (referred to as User Defined Functions, or UDFs) and couple them with the main code in order to add or modify closure relations, impose arbitrary transient

boundary conditions, and/or collect various domain properties, both local-instantaneous and time-average volume-average properties, that are not default options in the main Fluent tool bar.

For this investigation, two types of continuum-based conservation equations were utilized for modeling the fluid flow and heat transfer processes. One set of continuum-based conservation equations are the well-known Navier-Stokes (NS) equations along with energy transport equation. NS equations are discretized and solved for the components and parts in the test domain that are not porous structures and represent open spaces. The other set represents the volume-averaged conservation equations, based on porous media flow theory. For the component parts that are better represented as porous media, these volume-averaged continuum conservation equation are used to solve the fluid flow and heat transfer processes. All porous media/regenerator parts are modeled using the latter set of conservation equations.

The general continuum-based governing equations (NS and energy) used by the Fluent code [Ansys Fluent (2011, [81])] are as follows

$$\frac{\partial \rho}{\partial t} + \nabla \cdot (\rho \vec{u}) = 0 \tag{4.1}$$

$$\frac{\partial (\rho \vec{u})}{\partial t} + \nabla \cdot (\rho \vec{u}\vec{u}) + \nabla P - \nabla \cdot \bar{\bar{\tau}} - \rho \vec{g} = 0 \tag{4.2}$$

$$\nabla \cdot \left(k \nabla T + \bar{\bar{\tau}} \cdot \vec{u} \right) - \frac{\partial (\rho E)}{\partial t} - \nabla \cdot \left(\vec{u} \left(\rho E + P \right) \right) = 0 \tag{4.3}$$

where

$$E = h - \frac{P}{\rho} + \frac{u^2}{2} \tag{4.4}$$

$$\bar{\bar{\tau}} = \mu\left\{\left\langle \nabla\vec{u} + \nabla\vec{u}^{T} \right\rangle - \frac{2}{3}\nabla\cdot\vec{u}\,\bar{\bar{I}}\right\} \tag{4.5}$$

where

$\bar{\bar{I}}$ = the second-order unit tensor.

The second term on the right hand side of Equation 4.5 represents the effect of volume dilation. The quantity $2/3\,\mu$ is in fact the second coefficient of viscosity. All properties in these equations represent the properties of the working fluid (usually helium for cryocoolers and their experimental representations).

The above equations apply to all components of an entire PTC system, except for the regenerator and heat exchangers, which are modeled as porous mediums. The warm and cold-end heat exchangers are modeled as a porous media because porous media representation is flexible and is not restricted to any particular geometric configuration. When it is assumed that there is local thermodynamic equilibrium between the fluid and the solid structure, the mass, momentum, and energy equations in the porous media components are represented by,

$$\frac{\partial(\varepsilon\rho)}{\partial t} + \nabla\cdot(\varepsilon\rho\vec{u}) = 0 \tag{4.6}$$

$$\begin{aligned}\frac{\partial(\varepsilon\rho\vec{u})}{\partial t} + \nabla\cdot(\varepsilon\rho\vec{u}\vec{u}) + \varepsilon\nabla P + \nabla\cdot\left(\varepsilon\bar{\bar{\tau}}\cdot\vec{u}\right) \\ -\varepsilon\vec{F}_{bf} + \mu\bar{\bar{\beta}}^{-1}\cdot\vec{u} + \frac{\bar{\bar{C}}\rho}{2}\cdot|\vec{u}|\vec{u} = 0\end{aligned} \tag{4.7}$$

$$\nabla\cdot\left(\left(\varepsilon k_f+(1-\varepsilon)k_s\right)\nabla T+\overline{\overline{\tau}}\cdot\varepsilon\vec{u}\right)=$$
$$\frac{\partial}{\partial t}\left(\varepsilon\rho_f E_f+(1-\varepsilon)\rho_s E_s\right)+\nabla\cdot\left(\varepsilon\vec{u}\left(\rho_f E_f+P\right)\right) \tag{4.8}$$

where

ε = porosity

$\overline{\overline{\beta}}$ $[m^2]$ = viscous resistance coefficient tensor

$\overline{\overline{C}}$ $[m^{-1}]$ = inertial resistance coefficient tensor

$\vec{u}$ = velocity

The porous media of interest here, namely fillers used for regenerators or heat exchangers, are anisotropic. However, they are usually homogeneous and have *axi-symmetric anisoptropy* (also referred to as *transverse* anisotropy) [Bear (1972, [43])]. For these porous media there exists a unique (axial) principle direction, while in any plane that is perpendicular to the aforementioned axial direction, any line can be considered a principle direction. In other words, only axial and lateral (radial) directions need to be defined, because the hydraulic conductivity for all radial directions is the same. When flow along a principle direction [x (axial) and r (radial), in our case] is considered, the Darcy permeability, K_j, and Forchheimer's inertial coefficient, $c_{f,j}$, can be compared directly to the last two terms in Eqn. (4.7) to obtain the following relationship,

$$\frac{\varepsilon\mu}{K_j}u_j+\frac{c_{f,j}\varepsilon^2\rho}{\sqrt{K_j}}\cdot|\vec{u}|u_j=\frac{\mu}{\varepsilon\beta_j}u_j+\frac{C_j\rho}{\varepsilon 2}\cdot|\vec{u}|u_j \tag{4.9}$$

where $j = x, r$.

By comparing the coefficients of first and second order terms on the two sides of the equation, the Darcy permeability, K_j and the Forchheimer's inertial coefficient, $c_{f,j}$, can be represented as,

$$K_j = \varepsilon^2 \beta_j \tag{4.10}$$

$$c_{f,j} = \frac{C_j \sqrt{K_j}}{2\varepsilon^3} \tag{4.11}$$

In the forthcoming sections, several computational models are developed using the above sets of equations to characterize the fluid flow and heat transfer phenomenon in this investigation.

4.2 Exact Solutions for Steady Flow in Anisotropic Porous Medium

There are only a limited numbers of exact solutions that describe the pressure drop across a porous medium. The derivation of exact solutions for the axial pressure drop across a porous medium bounded by an impermeable wall on its outer boundary, where the flow is assumed to be one-dimensional, compressible, isothermal, and steady-state can be found in Cha [Cha (2007,[11])].

This analytical approach is employed for the regenerator filler study since the porous media is represented on the component-level, keeping consistent with the associated experimental tests. For the pore-level study, however, the viscous and inertial

resistance coefficients are determined by collecting the fluid and physical time-average, volume-average, and local instantaneous properties of the computational simulation domain at important locations (such as the inlet and exit of the domain) and substituted into the porous media Navier-Stokes momentum equation, Equation 4.7. For this reason, the pore-level CFD simulations do not make any arbitrary assumptions and can be considered to represent direct numerical simulations.

4.3 Computational Fluid Dynamics (CFD) Models

In this section, the computational fluid dynamics models used for both the pore-level study and the regenerator filler study, in steady and periodic flow, are presented and discussed.

4.3.1 Pore-Level Study

The generic porous media simulated here are regularly spaced square rods arranged in a linear pattern with rows parallel to the direction of the flow field. The domain is similar to those addressed by Kim, Pathak, Mulcahey, and Ghiaasiaan [Kim and Ghiaasiaan (2009, [31]), Pathak and Ghiaasiaan (2010, [32]), Mulcahey et al. (2012, [33])]. Figure 4.1 displays the physical configuration of the parallel square rods. Previous researchers typically studied the flow details in a single unit cell, using periodic boundary conditions. However, for periodic flow, simulation of a single unit cell is not sufficient due to the entrance effect complications and the development of phase shift which makes simple periodic boundary conditions along the main flow direction unsuitable [Kim and Ghiaasiaan (2009, [31])]. Therefore, the generic computational domain for this study is composed of seven consecutive unit cells in series.

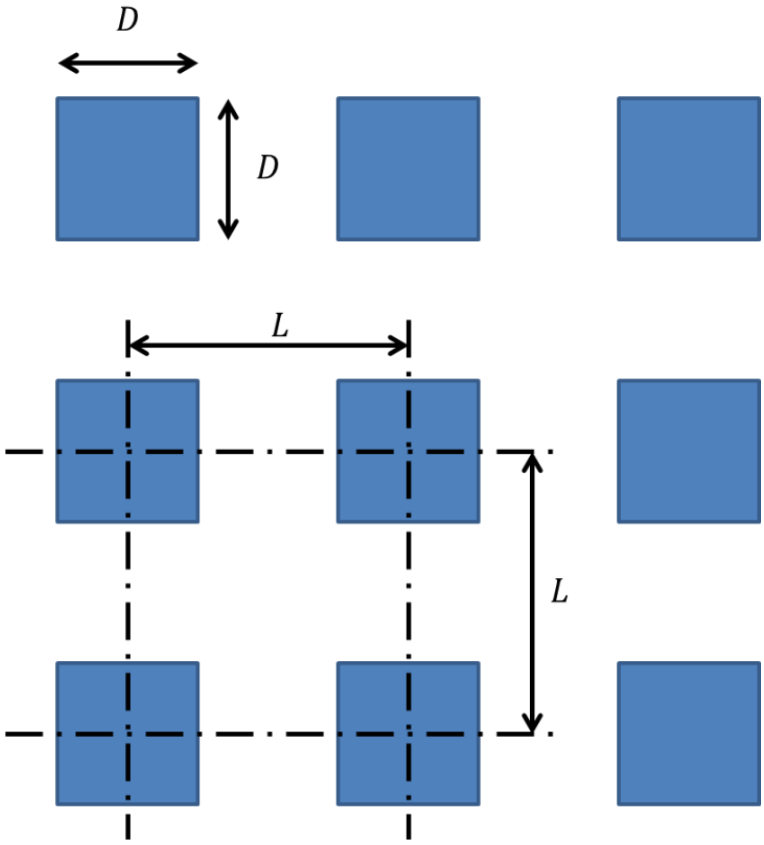

Figure 4.1. Generic computational domain.

The upper and lower surfaces of each unit cell consist of a symmetry boundary condition, since the flow about the x-axis for the entire computation domain is symmetric. The square cylinders have an edge length of D = 100 μm, hydraulic diameter, D_h = 50 μm, and the domain has a porosity of 0.75.

Previous studies also indicate that the end effects of the simulated row of the unit cells essentially disappear after the first few unit cells with the addition of beginning and ending buffer zones [Kim and Ghiaasiaan (2009, [31]), Pathak and Ghiaasiaan (2010, [32]), Mulcahey et al. (2012, [33])]. Following the results of the numerical investigation

of Kim, Pathak, Mulcahey, and Ghiaasiaan, the buffer zone at the inlet has a length of $10D_h$ for the high amplitude cases and a length of $2.5D_h$ for the low amplitude cases. In actual operation the amplitude to D_h ratio is much closer to 100, however 10 at the maximum was used to simulate and understand where the low amplitude effects mitigate. These buffer zones were used at both the inlet and exit. For all cases, the ratio of amplitude to buffer zone was kept constant at 0.8. The flow details of the fourth unit cell were used in the pore-scale computations so that all end effects were mitigated. The entire computational domain with the buffer zones is shown in Figure 4.2.

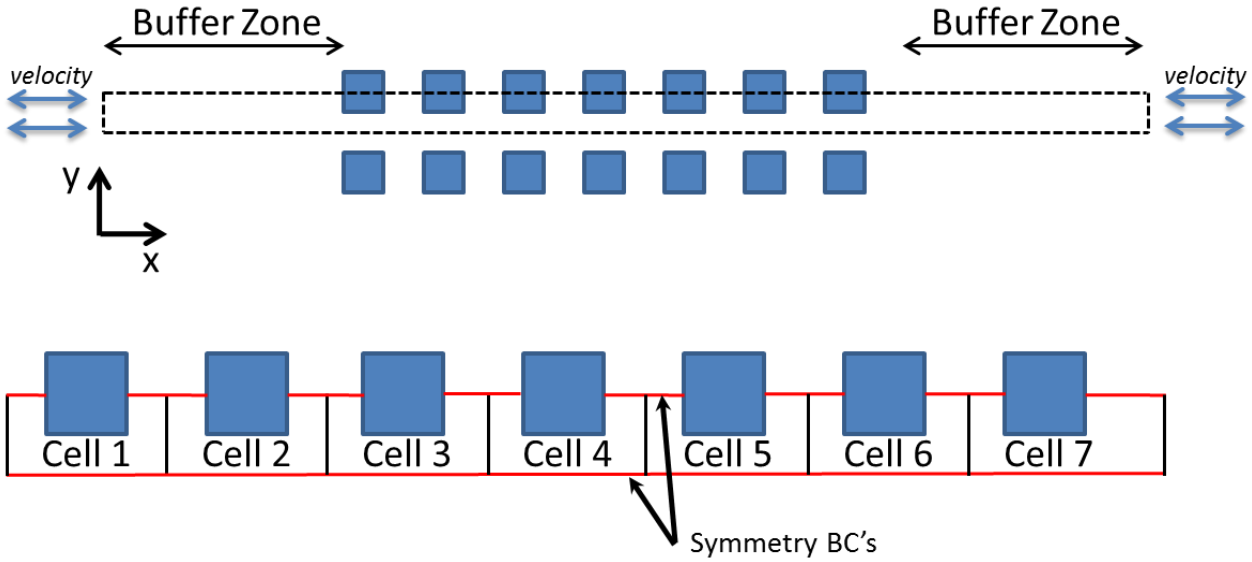

Figure 4.2. Computational domain.

The microscopic level (pore-scale) calculations were performed by numerically solving the mass, momentum, and energy conservation equations in the domain shown in Figure 4.2. The CFD code Ansys Fluent [Ansys Fluent (2011, [81])] was used for this purpose. The pressure-based Navier-Stokes coupled solution algorithm of Fluent, which

includes low Mach number conditioning, artificial compressibility, and dual time stepping for the solution of unsteady flow, was used to solve the mass continuity, momentum, and thermal-energy conservation equations simultaneously.

The two-dimensional mesh and details of cell 4, generated by using Gambit [Fluent (2003, [98])], are shown in Figure 4.3.

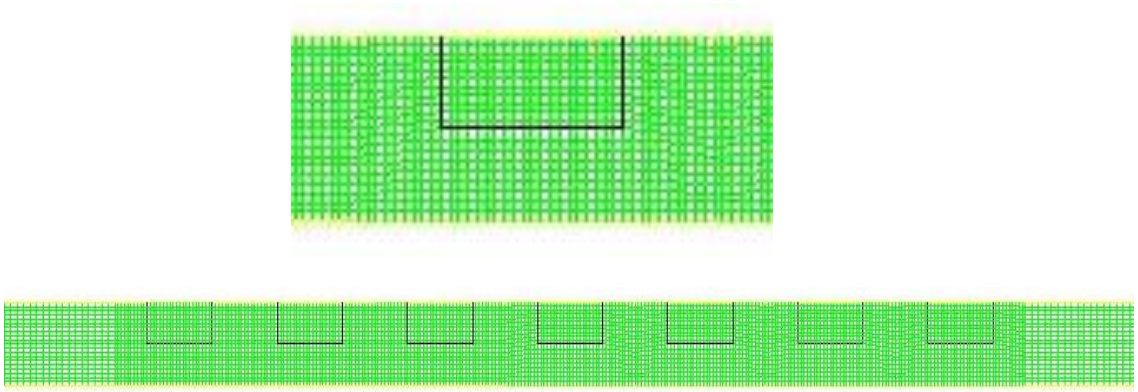

Figure 4.3. 2D mesh and details of cell 4 for low amplitude case.

For initial conditions, first a steady-state simulation was performed assuming that helium at 2 MPa pressure and a temperature of 80 K filled the entire system. Transient simulations were then initiated by imposing the following moving wall boundary condition as a special user defined function (UDF).

$$U = \omega a \cos(\omega t) \tag{4.12}$$

Detailed description of this UDF code is shown in Appendix A.

The solid interface experienced conjugate heat transfer. The micro-scale numerical calculations were continued until steady periodic conditions were reached,

whereafter all calculated parameters everywhere in the simulated system were identical from one cycle to the next. All simulations assumed laminar flow for both steady and unsteady cases.

Once steady-periodic conditions were established, various parameters were calculated. These included volume-average velocity, pressure, and temperature; instantaneous and volume-average Darcy permeability, Forchheimer, and Nusselt Number. The instantaneous permeability-based and unit cell length-based Nusselt number was found from,

$$Nu_K = \frac{Q\sqrt{K}}{kA\Delta T} \tag{4.13}$$

$$Nu_L = \frac{QL}{kA\Delta T} \tag{4.14}$$

where the temperature difference is defined as the low-end (80 K) and high-end (300 K) temperatures in the simulated system. This is similar to the definition used by Ashwin et al [Ashwin et al. (2011, [99])] for oscillatory flow.

For all numerical simulations, the convergence criterion applied to the residuals for the continuity and momentum equations was a tolerance of 10^{-3}. A convergence criterion of 10^{-6} was used for the energy equation residuals. These tolerance criteria are known to be quite adequate for simulations with Fluent [Ansys Fluent (2011, [81])]. A detailed grid independence study was performed, the results of which showed that good grid-independence could be achieved by using 20×40 nodes in each unit cell. Table 4.1 and Figure 4.4, show the comparison of unsteady flow results at 6 six seconds between a 20x40 mesh and a 40×80 mesh for a low amplitude 60 Hz case for unit cell 4, and temperature contours of the entire system, respectively.

Table 4.1. Comparison of results for meshes.

Parameter	20x40 Mesh	40x80 Mesh
Volume-Average Temperature (K)	188.7	185.4
Volume-Average Velocity (m/s)	0.054	0.052

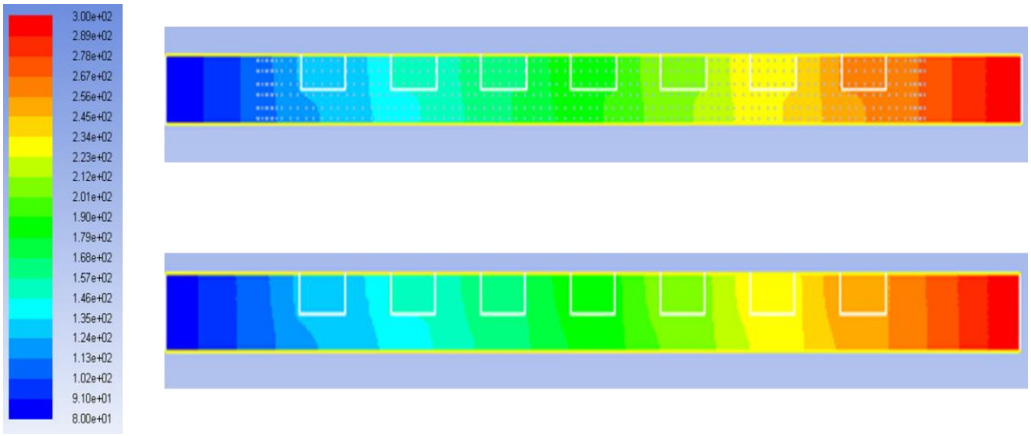

Figure 4.4. Temperature contours for 20x40 mesh (top) and 40x80 mesh (bottom).

As mentioned before, all the volume-average terms were calculated using UDFs and post processing. The correctness and consistency of these computations could then be ascertained by using these computed volume-average terms in the aforementioned equation. This was done for selected runs, where the volume-average porous media momentum conservation equation was finite differenced using forward differencing in time and central differencing in space, and performing macroscopic calculations for unit

cell 4. Excellent results were obtained. As a note, one simulation takes approximately 576 hours to run on a commercially available core i7 PC, typically to reach steady-periodic conditions. For this reason, relatively very few results exist in open literature.

4.3.2 Regenerator Filler Study

The commercial CFD code Ansys Fluent [Ansys Fluent (2011, [81])] was used to model the entire annular regenerator test section, in order to facilitate the interpretation of the experimental data. Given the configuration of the test section, axi-symmetric, two-dimensional flow was assumed. The simulated system evidently has two completely different parts (a pure single phase fluid and a porous medium). For the open (purely fluid) parts, the steady state mass, momentum and energy equations solved by Fluent are shown in Equations 4.1-4.5.

All properties represent the Newtonian working fluid, helium. The above equations apply to all sections in the entire test section, except for the annular porous structure – the ErPr rare-Earth regenerator filler. The latter region is modeled as an isotropic porous medium with the local thermal equilibrium assumption. The steady-state mass, momentum, and energy equations for this region is then represented by Equations 4.6-4.8, where all of the velocities are volume-averaged physical (intrinsic) velocities.

Steady flow CFD simulations for the entire test section were performed using approximately 12,000 mesh nodes. The nodalization of the test section was done by using Gambit, a CFD meshing tool [Fluent (2003, [98])]. Once the physical 2-D drawings were generated, meshing was applied to the drawing as shown in Figure 4.5. Upon a successful meshing process, the meshed case is then imported into Ansys Fluent. At this point, the material properties and the boundary conditions are assigned to the system based on the actual problem definition. For this particular model, the imposed boundary

conditions are the mass flow rate at the inlet location and the exit location pressure, whereas the inlet location pressure was collected and matched with the experimental data.

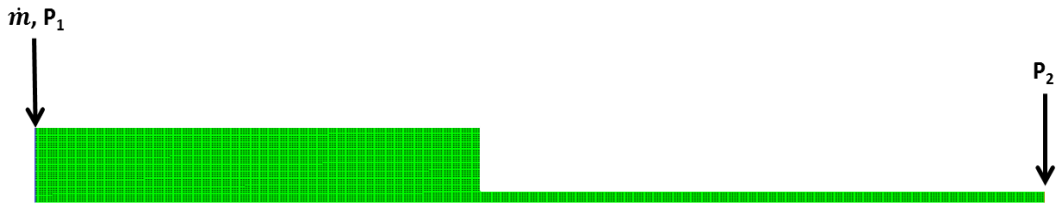

Figure 4.5. Model for steady flow simulations with meshing.

All the simulations were performed using a normalized residual convergence criterion of 1.0×10^{-6} for the mass, x-velocity, and r-velocity, and 1.0×10^{-8} for the energy. The third-order MUSCL discretization scheme and pressure-velocity coupling scheme were applied to the above mentioned continuum based conservation equations.

The physical dimensions of the radial test section for steady flow tests are summarized in Table 4.2 and in Figure 4.6 according to their component index notations.

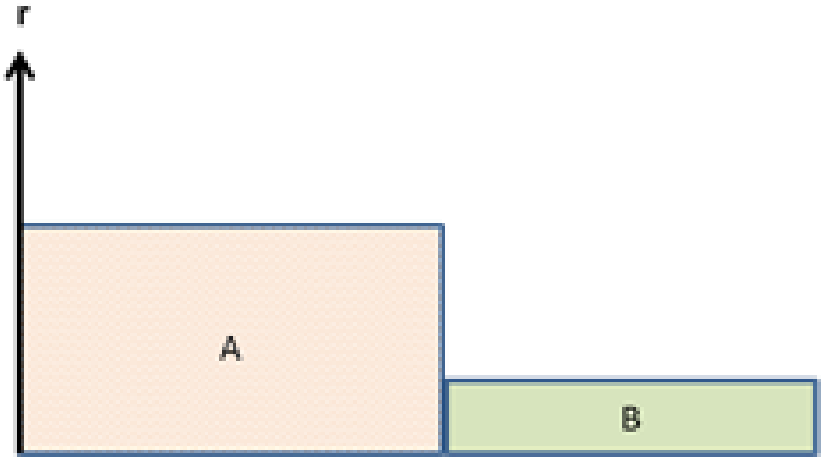

Figure 4.6. Component index notation of test section for steady flow.

Table 4.2.Component geometry of steady flow test section.

Component Index	Radius, r (cm)	Length (cm)
A (regenerator test section)	1.15	5.08
B (transfer line)	0.23	6.35

The models for oscillatory flow tests are now discussed. Experimentally measured mass flow rate values at the inlet location were imposed in the model as the boundary condition to simulate oscillatory flow conditions. Due to the transient nature of oscillatory flow, time dependent continuum based conservation equations were used to model the test apparatus. Given that the test apparatus is cylindrical and all the components are linearly aligned in series and form an axi-symmetric system, the entire test section is modeled in a two-dimensional axi-symmetric coordinate system.

Similar to the aforementioned description, the simulated system had two different parts (purely fluid part and porous medium part). For the open (purely fluid) part, Equations 4.1-4.3, which represent the mass, momentum, and energy conservation equations, respectively, were used. For the porous region, Equations 4.6-4.8, which represent the single phase volume-averaged mass, momentum, and energy conservation equations, respectively, were used.

The boundary conditions for the tests, as well as the simulations included a known inlet time-dependent mass flow rate, known outlet time-dependent pressure, and isothermal and impermeable walls (at room temperature, 300 K). The initial operating pressure for each simulation was the corresponding experimental charge pressure for that particular simulation case.

As mentioned earlier, the user defined function (UDF) feature in Fluent provides capability of imposing time dependent flow and heat transport properties such as pressure, temperature, density, velocity, mass flow rate, etc, at any desired boundary of the meshed model. In this investigation a transient mass flow rate and pressure UDF was developed, and was coupled with the main CFD code in order to impose time dependent mass flow rate inlet boundary conditions and pressure outlet boundary conditions. Before the aforementioned UDF was hooked and compiled to the code, experimentally measured pressure and mass flow rate data were first transformed to the frequency domain form by Fast Fourier Transformation (FFT) and were represented as Fourier Sine Series. Using the first harmonic of magnitude and phase, actual measured pressure waveforms were replicated. The transformed mass flow rates and pressures were then represented using the following expressions,

$$P_i(t) = \sum_{n=1}^{\infty} P_n \sin(n\omega t + \varphi_n), \omega = 2\pi f, i = 1,2 \quad (4.15)$$

$$\dot{m}_i(t) = \sum_{n=1}^{\infty} \dot{m}_n \sin(n\omega t + \varphi_n), \omega = 2\pi f, i = 1 \quad (4.16)$$

Using a UDF, the exact mathematical function represented by Equations 4.15-4.16 could be imposed at the inlet and exit of the regenerator to simulate the mass flow and pressure oscillations. Detailed description of this UDF code is shown in Appendix A.

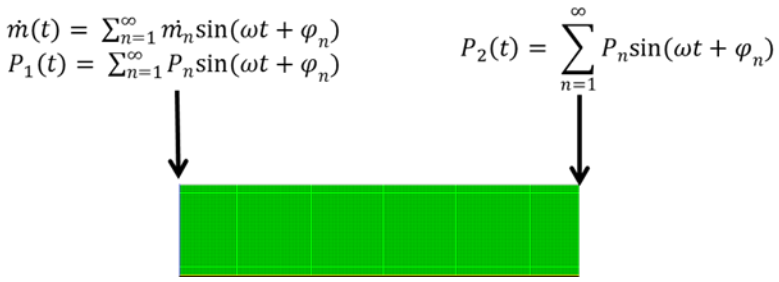

Figure 4.7. Model for oscillatory flow simulations with meshing.

CFD simulations for the annular test section were performed using approximately 9,600 mesh nodes. The grid and meshing representation of the model is shown in Figure 4.7.

The third-order MUSCL discretization scheme and pressure–velocity coupling scheme were used in all the simulations. A normalized residual convergence criterion of 1.0×10^{-6} for the mass, x-velocity, and r-velocity, and 1.0×10^{-8} for the energy, were used.

Twenty four oscillatory flow CFD simulations were performed using this model. Each simulation represented a specific oscillation frequency and piston amplitude. The

simulated frequencies were in the range of 30-70 Hz, these frequencies of course represented the experiments.

The solution time increment plays a crucial role in obtaining fully converged solutions in any numerical analysis. Larger time steps are always desired for the purpose of minimizing the computation time. However, large time steps can lead to code divergence. Thus optimum time step must be found for each simulation. A near-optimal time step of 1.5×10^{-5} seconds was found by trial and error. The finest time step, which is typically reserved for the lowest frequency case, was used for all of the simulations.

The physical dimensions of the model and component notations are shown in Table 4.3 and in Figure 4.8. Figure 4.8 is shown in the cylindrical coordinate system.

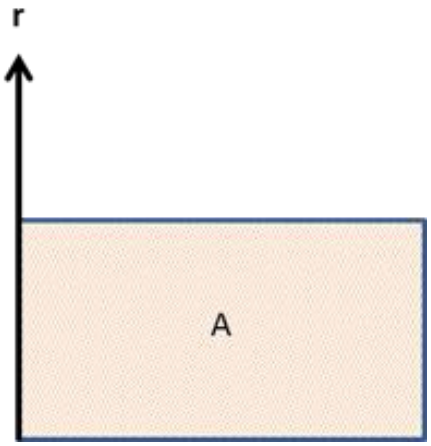

Figure 4.8. Component index notation of test section for oscillatory flow.

Table 4.3. Component geometry of test section for oscillatory flow.

Component Index	Radius, r (cm)	Length (cm)
A (regenerator test section)	1.15	5.08

CHAPTER 5

RESULTS AND DISCUSSION

This chapter describes the results and provides the associated discussion for the dissertation investigation. Specifics of the steady flow and periodic flow experimental test results are first discussed. Using the experimental measurements, furthermore, the steady and oscillatory hydrodynamic parameters, namely, the Darcy permeability and Forchheimer's inertial coefficients of ErPr rare-Earth regenerator filler are calculated and presented. These hydrodynamic parameters are calculated using the CFD analysis methods described in Chapter 4. Then correlations for the experimental data pertaining to steady flow and periodic flow are presented. The chapter concludes with the results and discussion of the pore-level study, which include the calculation of steady and oscillatory hydrodynamic and thermal parameters including the Darcy permeability, Forchheimer's inertial coefficient, and Nusselt number.

5.1 Steady Flow Experiments

Using helium as the working fluid, steady-state pressure drops were measured over a wide range of flow rates in the test section that contained regenerator filler. The tests were performed in the apparatus described in Chapter 3, and the experimental data was analyzed using CFD simulations according to Chapter 4. The aforementioned hydrodynamic parameters were then obtained by comparing the data with the results of CFD calculations that simulated the test section. CFD simulations of the experiments were performed iteratively, whereby permeability and Forchheimer coefficients that brought about agreement between data and simulation results were calculated.

For steady flow a total of fifty nine tests were conducted, with each test representing a fixed charge pressure and mass flow rate. CFD simulations were performed for all the measured data using the methodology described in the previous section. Excellent agreement between data and simulation results were obtained using the β and C (or, alternatively, K and c_f) values summarized in Table 5.1.

Table 5.1. Steady flow parameters and results.

Case	P_{charge}(Pa)	P_{in} (Pa)	P_{out} (Pa)	$\dot{m}$(kg/s)	P^*	Re_K	c_f
1	3.45E+05	3.40E+05	3.07E+05	4.33E-05	0.345	0.023	539.8
2	3.45E+05	3.41E+05	2.60E+05	8.66E-05	0.345	0.046	341.5
3	3.45E+05	3.40E+05	1.55E+05	1.73E-04	0.345	0.091	195.1
4	3.45E+05	3.40E+05	1.18E+05	1.95E-04	0.345	0.103	184.3
5	3.45E+05	3.41E+05	1.05E+05	2.08E-04	0.345	0.110	173.1
6	5.17E+05	5.20E+05	4.72E+05	8.66E-05	0.517	0.046	311.1
7	5.17E+05	5.21E+05	4.26E+05	1.73E-04	0.517	0.091	151.9
8	5.17E+05	5.19E+05	3.56E+05	2.60E-04	0.517	0.137	116.7
9	5.17E+05	5.20E+05	2.52E+05	3.46E-04	0.517	0.183	108.8
10	5.17E+05	5.20E+05	1.16E+05	4.24E-04	0.517	0.224	110.0
11	6.89E+05	7.01E+05	6.67E+05	8.66E-05	0.689	0.046	291.9
12	6.89E+05	7.01E+05	6.32E+05	1.73E-04	0.689	0.091	148.7
13	6.89E+05	7.01E+05	5.88E+05	2.60E-04	0.689	0.137	109.2
14	6.89E+05	7.01E+05	5.32E+05	3.46E-04	0.689	0.183	91.6
15	6.89E+05	7.01E+05	4.76E+05	4.33E-04	0.689	0.229	78.4
16	6.89E+05	7.01E+05	3.99E+05	5.19E-04	0.689	0.274	73.2

17	6.89E+05	7.01E+05	3.09E+05	6.06E-04	0.689	0.320	70.0
18	6.89E+05	7.01E+05	1.74E+05	6.92E-04	0.689	0.366	72.4
19	6.89E+05	7.02E+05	1.33E+05	7.10E-04	0.689	0.375	74.4
20	8.62E+05	8.71E+05	8.42E+05	8.66E-05	0.862	0.046	319.5
21	8.62E+05	8.69E+05	8.13E+05	1.73E-04	0.862	0.091	154.3
22	8.62E+05	8.70E+05	7.79E+05	2.60E-04	0.862	0.137	112.4
23	8.62E+05	8.69E+05	7.41E+05	3.46E-04	0.862	0.183	88.4
24	8.62E+05	8.71E+05	6.94E+05	4.33E-04	0.862	0.229	78.0
25	8.62E+05	8.70E+05	6.52E+05	5.19E-04	0.862	0.274	67.2
26	8.62E+05	8.69E+05	5.96E+05	6.06E-04	0.862	0.320	62.0
27	8.62E+05	8.70E+05	5.43E+05	6.92E-04	0.862	0.366	56.8
28	8.62E+05	8.70E+05	4.71E+05	7.79E-04	0.862	0.411	54.8
29	8.62E+05	8.70E+05	3.99E+05	8.66E-04	0.862	0.457	52.4
30	1.03E+06	1.06E+06	1.03E+06	8.66E-05	1.034	0.046	313.5
31	1.03E+06	1.05E+06	1.01E+06	1.73E-04	1.034	0.091	156.7
32	1.03E+06	1.05E+06	9.80E+05	2.60E-04	1.034	0.137	110.0
33	1.03E+06	1.05E+06	9.45E+05	3.46E-04	1.034	0.183	91.2
34	1.03E+06	1.06E+06	9.16E+05	4.33E-04	1.034	0.229	76.0
35	1.03E+06	1.05E+06	8.82E+05	5.19E-04	1.034	0.274	65.6
36	1.03E+06	1.06E+06	8.46E+05	6.06E-04	1.034	0.320	58.4
37	1.03E+06	1.05E+06	8.03E+05	6.92E-04	1.034	0.366	53.6
38	1.03E+06	1.06E+06	7.66E+05	7.79E-04	1.034	0.411	48.8
39	1.03E+06	1.04E+06	7.00E+05	8.66E-04	1.034	0.457	47.2
40	1.38E+06	1.41E+06	1.38E+06	8.66E-05	1.379	0.046	398.2

41	1.38E+06	1.40E+06	1.37E+06	1.73E-04	1.379	0.091	170.3
42	1.38E+06	1.40E+06	1.34E+06	2.60E-04	1.379	0.137	118.3
43	1.38E+06	1.40E+06	1.32E+06	3.46E-04	1.379	0.183	91.2
44	1.38E+06	1.40E+06	1.30E+06	4.33E-04	1.379	0.229	77.2
45	1.38E+06	1.41E+06	1.27E+06	5.19E-04	1.379	0.274	67.2
46	1.38E+06	1.40E+06	1.25E+06	6.06E-04	1.379	0.320	58.0
47	1.38E+06	1.41E+06	1.22E+06	6.92E-04	1.379	0.366	53.2
48	1.38E+06	1.40E+06	1.19E+06	7.79E-04	1.379	0.411	48.0
49	1.38E+06	1.40E+06	1.15E+06	8.66E-04	1.379	0.457	45.6
50	1.72E+06	1.76E+06	1.74E+06	8.66E-05	1.724	0.046	483.8
51	1.72E+06	1.75E+06	1.72E+06	1.73E-04	1.724	0.091	189.9
52	1.72E+06	1.76E+06	1.71E+06	2.60E-04	1.724	0.137	133.1
53	1.72E+06	1.76E+06	1.69E+06	3.46E-04	1.724	0.183	99.6
54	1.72E+06	1.76E+06	1.67E+06	4.33E-04	1.724	0.229	79.6
55	1.72E+06	1.75E+06	1.64E+06	5.19E-04	1.724	0.274	68.8
56	1.72E+06	1.75E+06	1.62E+06	6.06E-04	1.724	0.320	60.8
57	1.72E+06	1.76E+06	1.61E+06	6.92E-04	1.724	0.366	53.6
58	1.72E+06	1.75E+06	1.59E+06	7.79E-04	1.724	0.411	48.4
59	1.72E+06	1.75E+06	1.56E+06	8.66E-04	1.724	0.457	44.8

CFD simulations using the aforementioned parameters led to excellent agreement with measurements. The permeability was found to be $K=1.93\times10^{-11}$ m^2, corresponding to $\beta=1.33\times10^{-10}$ m^2, for all the cases. The simulated results for the $Er_{50}Pr_{50}$ regenerator filler are depicted in Figure 5.1, where c_f is shown as a function of Re_K.

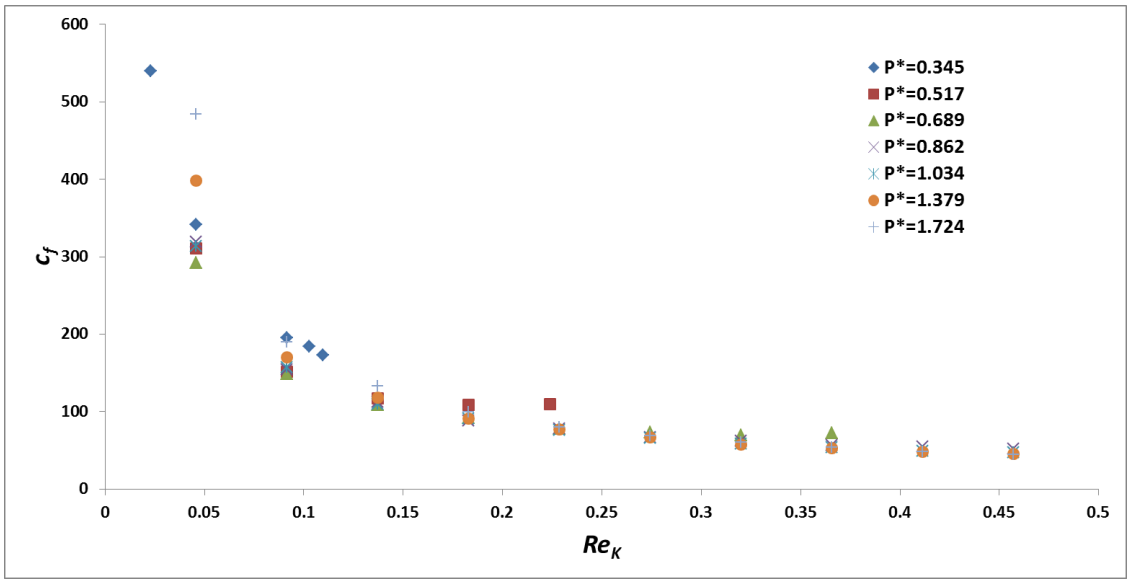

Figure 5.1. Plot of c_f as a function of Re_K for steady flow.

The results indicate that for lower flow rates, or Reynolds numbers, the effect of charge pressure on the inertial resistance exists, however this effect is mitigated at larger flow rates, where the inertial resistance coefficient essentially approaches a constant value suggesting that the Forchheimer term is constant for ErPr regenerator filler material at higher flow rates, regardless of the associated charge pressure.

It is also important to note that from a practical application point of view, the higher flow rate steady flow cases are significantly more important since in actual cryocooler operation, the regenerator is experiencing oscillating flows that are higher order of magnitude flow rates, hence making the higher Reynolds number steady flow cases more applicable to compare with actual PTC operating flows.

5.2 Periodic Flow Experiments

A total of twenty four oscillatory flow tests were conducted, with each test representing a fixed compressor frequency, charge pressure, and piston stroke. The tests covered the frequency range 30–70 Hz. CFD simulations were performed for all the measured data using the methodology described in the previous chapter. Excellent agreement between data and simulation results were obtained using the K and c_f values, which are summarized in Table 5.2.

Table 5.2. Periodic flow parameters.

Case	P_{charge} (Pa)	f (Hz)	Amp (mm)	P_{in} (Pa)	φ_{Pin} (rad)	P_{out} (Pa)	φ_{Pout} (rad)	$\dot{m}$ (kg/s)	$\varphi_{\dot{m}}$ (rad)	P^*	Re_K	c_f
1	1.03E+06	30	1.68	1.82E+04	-0.68	4.05E+02	0.07	2.52E-04	-0.49	1.034	0.133	153.7
2	1.03E+06	30	2.03	2.23E+04	0.04	5.17E+02	0.01	3.00E-04	-0.49	1.034	0.159	133.7
3	1.03E+06	30	2.43	2.70E+04	0.12	6.11E+02	0.09	3.61E-04	-0.48	1.034	0.190	112.2
4	1.03E+06	30	3.16	3.57E+04	0.59	7.88E+02	0.24	4.60E-04	-0.48	1.034	0.243	92.2
5	1.03E+06	40	3.06	2.08E+04	0.16	2.48E+02	0.14	3.43E-04	-0.36	1.034	0.181	93.2
6	1.03E+06	40	3.58	2.59E+04	0.03	3.32E+02	0.00	4.05E-04	-0.36	1.034	0.214	83.9
7	1.03E+06	50	3.07	4.78E+04	0.17	2.80E+02	0.14	7.02E-04	-0.17	1.034	0.371	53.3
8	1.72E+06	30	1.27	2.06E+04	0.15	6.91E+02	-0.10	2.67E-04	-0.68	1.724	0.141	277.7
9	1.72E+06	30	1.54	2.57E+04	0.08	8.57E+02	0.17	3.46E-04	-0.67	1.724	0.183	206.9
10	1.72E+06	30	1.77	3.01E+04	0.16	1.03E+03	0.13	4.19E-04	-0.67	1.724	0.221	163.8
11	1.72E+06	30	2.29	4.00E+04	0.17	1.36E+03	0.15	5.64E-04	-0.66	1.724	0.298	119.8
12	1.72E+06	30	2.83	5.01E+04	0.09	1.69E+03	0.17	7.02E-04	-0.65	1.724	0.371	97.1
13	1.72E+06	40	2.19	2.12E+04	0.11	4.08E+02	0.09	3.30E-04	-0.45	1.724	0.174	186.3

14	1.72E+06	40	2.46	2.54E+04	0.08	5.08E+02	0.27	4.03E-04	-0.45	1.724	0.213	149.7
15	1.72E+06	40	2.83	3.08E+04	-0.19	5.80E+02	0.11	4.93E-04	-0.44	1.724	0.260	121.1
16	1.72E+06	40	3.51	4.07E+04	-0.24	7.84E+02	0.29	6.40E-04	-0.44	1.724	0.338	95.2
17	1.72E+06	50	1.96	3.46E+04	0.00	2.93E+02	-0.02	5.50E-04	-0.25	1.724	0.290	115.1
18	1.72E+06	50	2.34	4.17E+04	0.05	3.29E+02	0.24	6.58E-04	-0.25	1.724	0.347	94.1
19	1.72E+06	50	3.10	5.54E+04	0.14	5.16E+02	0.12	8.66E-04	-0.25	1.724	0.457	72.3
20	1.72E+06	50	3.88	6.91E+04	0.11	6.41E+02	0.09	1.06E-03	-0.24	1.724	0.561	60.0
21	1.72E+06	70	1.89	3.42E+04	0.17	2.93E+02	0.08	6.10E-04	-0.05	1.724	0.322	89.6
22	1.72E+06	70	2.48	4.48E+04	0.21	3.68E+02	0.12	8.02E-04	-0.05	1.724	0.424	68.0
23	1.72E+06	70	3.05	5.52E+04	0.18	4.48E+02	0.08	9.82E-04	-0.05	1.724	0.518	56.0
24	1.72E+06	70	3.62	6.57E+04	0.12	5.50E+02	0.13	1.16E-03	-0.04	1.724	0.611	48.0

Typical simulated results for the $Er_{50}Pr_{50}$ regenerator filler under periodic flow conditions are depicted in Figure 5.2-5.13 (where each plot corresponds to the associated case number in Table 5.2). These figures display the measured and predicted inlet pressure, and measured mass flow rate and outlet pressures for the different operating frequencies, piston strokes, and charge pressures associated with the periodic flow simulations. Careful review of these and other simulation results indicated that the flow field in the entire tested regenerator was predominantly one-dimensional, as expected. The figures also show that while there is near-perfect agreement between simulations and measurements with respect to the magnitude of pressure at inlet, a slight discrepancy between measurements and simulations with respect to the oscillation phase shift angles.

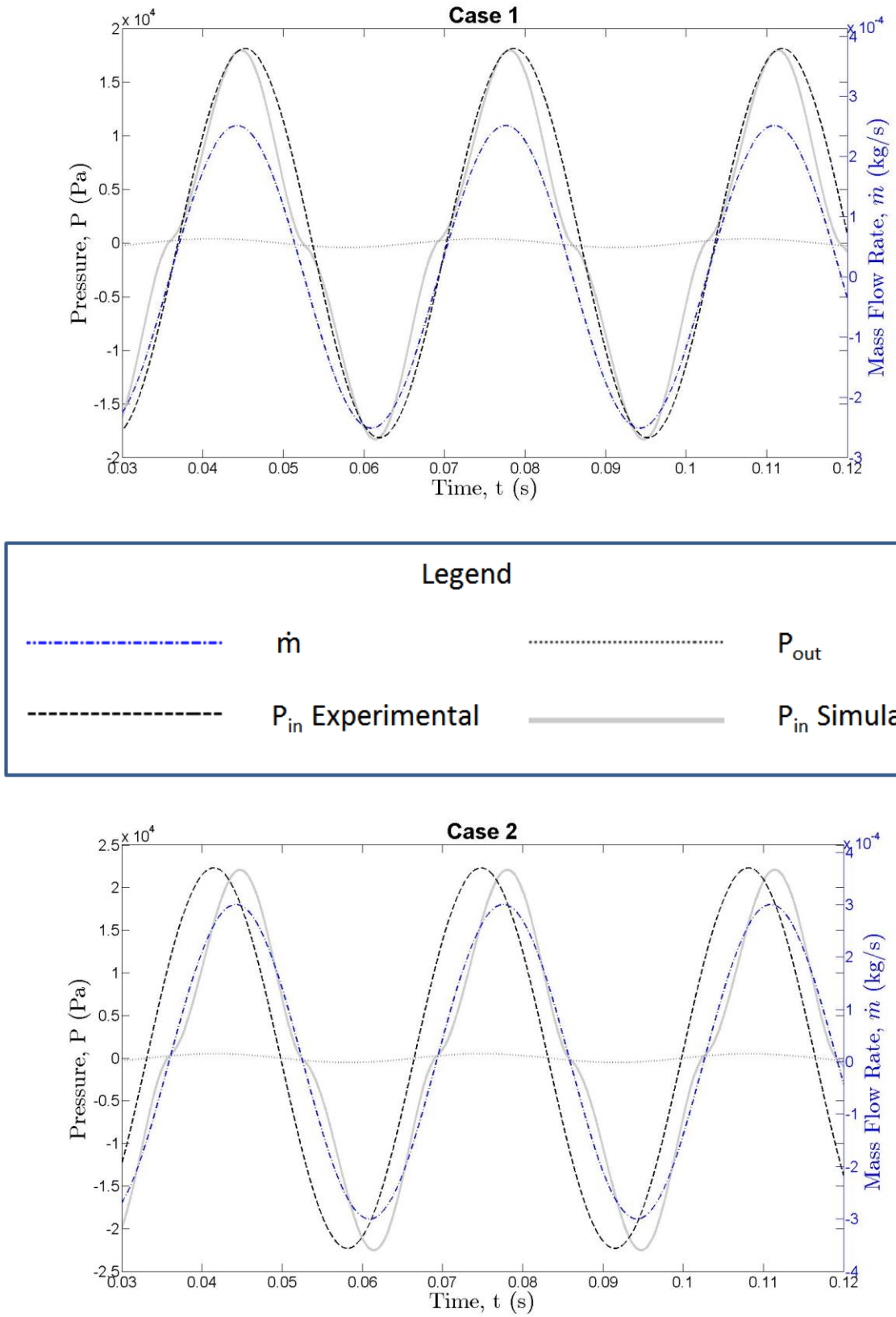

Figure 5.2. Imposed and predicted P_1, P_2, and $\dot{m}$ for periodic flow cases, Case 1-2.

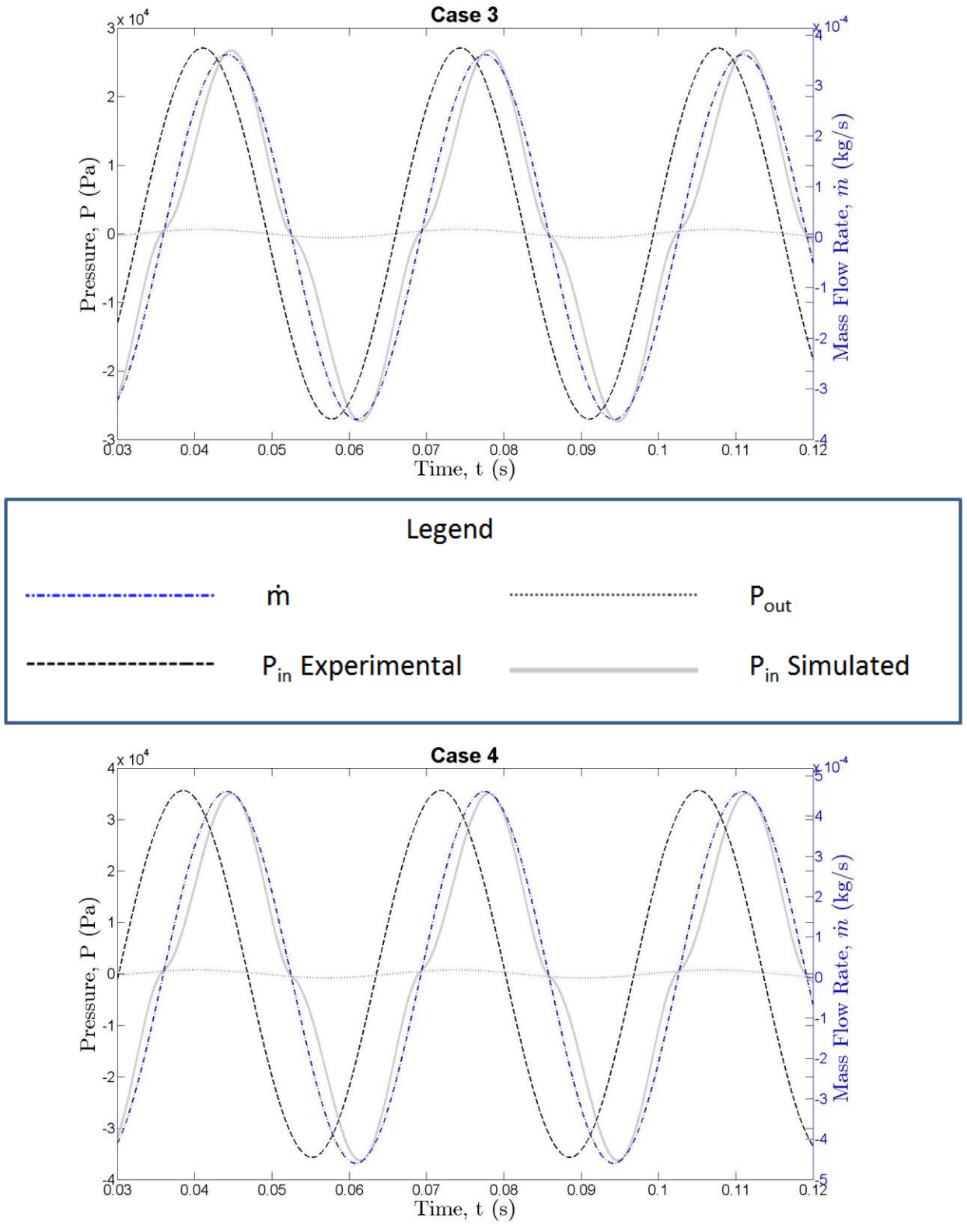

Figure 5.3. Imposed and predicted P_1, P_2, and $\dot{m}$ for periodic flow cases, Case 3-4.

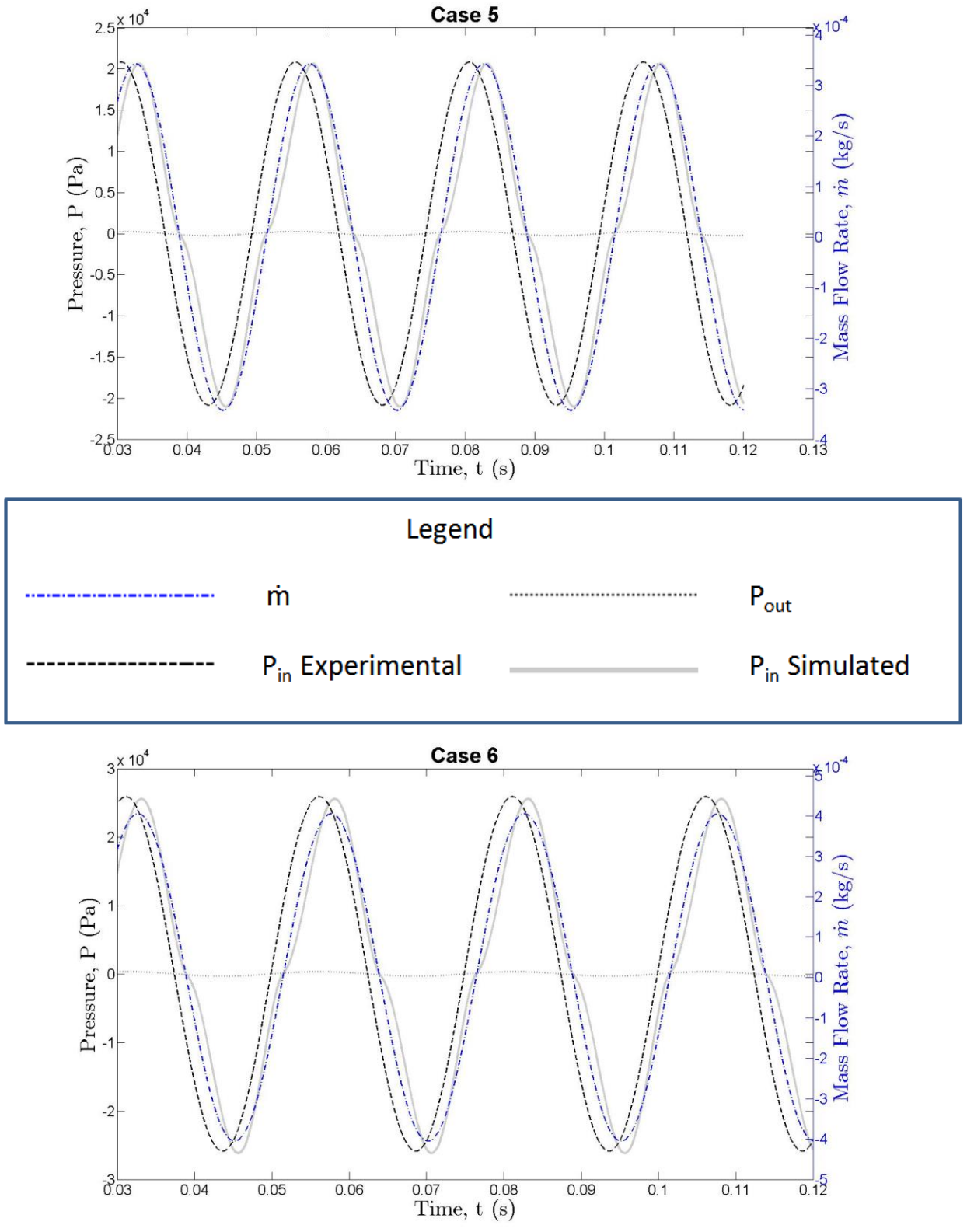

Figure 5.4. Imposed and predicted P_1, P_2, and $\dot{m}$ for periodic flow cases, Case 5-6.

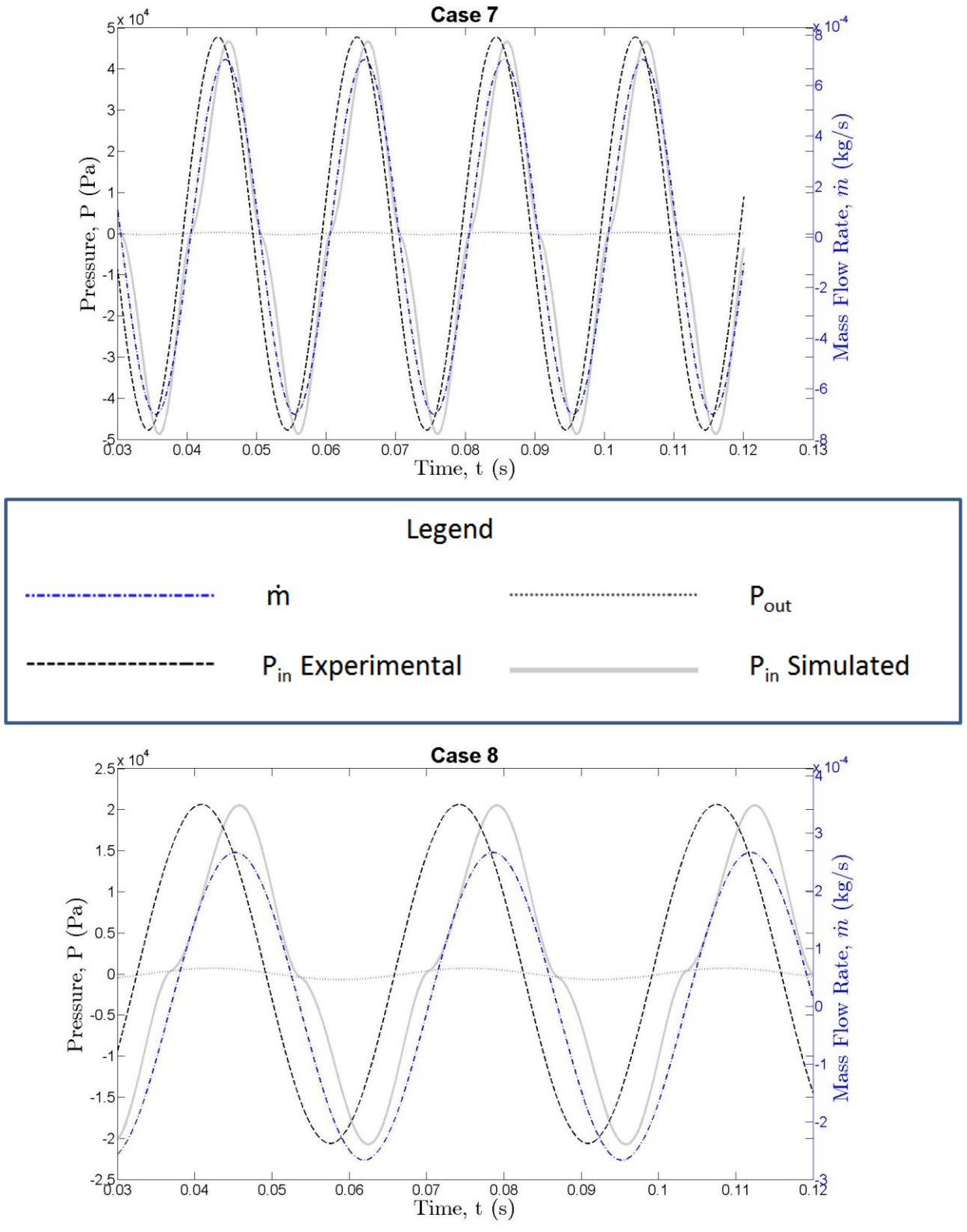

Figure 5.5. Imposed and predicted P_1, P_2, and $\dot{m}$ for periodic flow cases, Case 7-8.

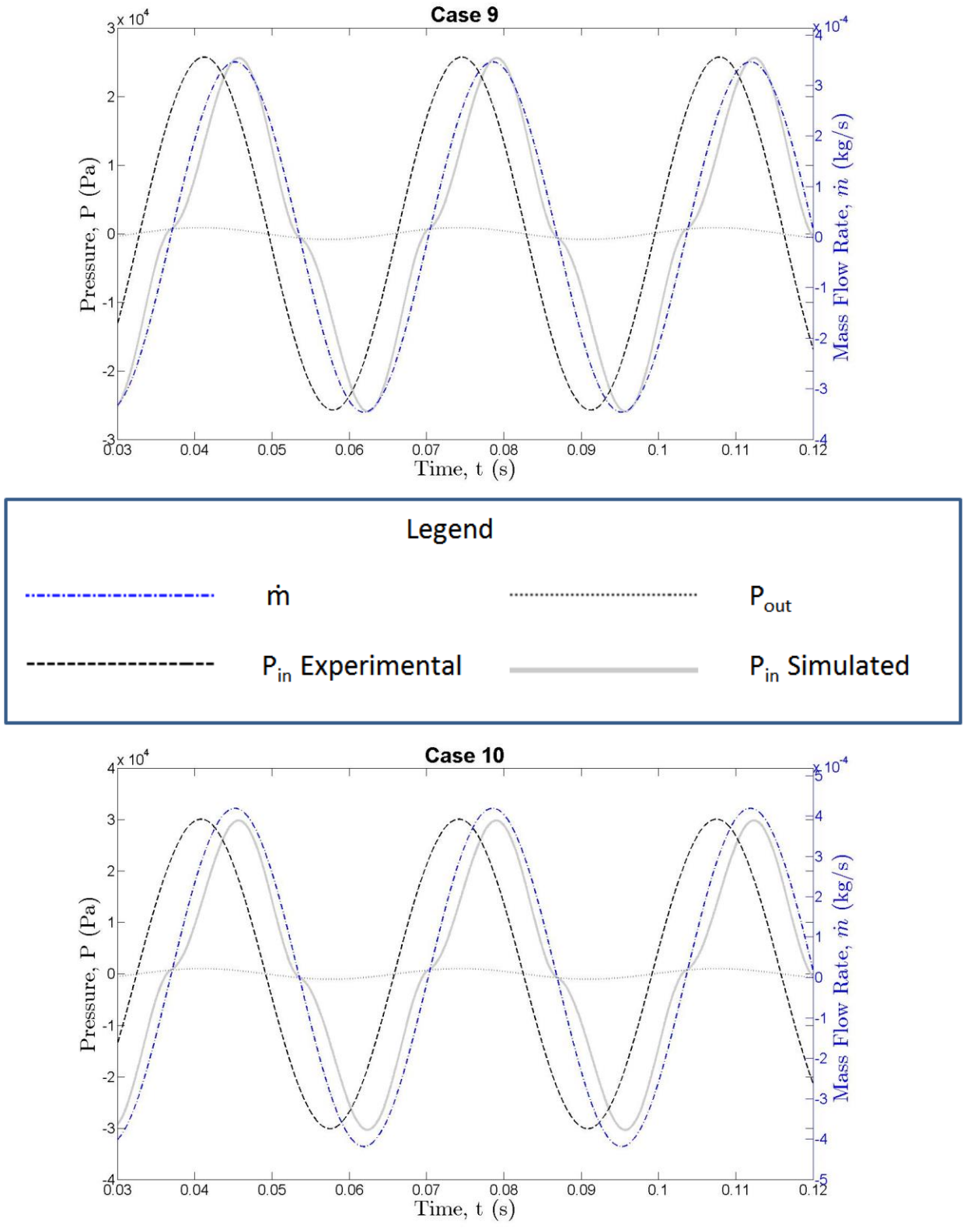

Figure 5.6. Imposed and predicted P_1, P_2, and $\dot{m}$ for periodic flow cases, Case 9-10.

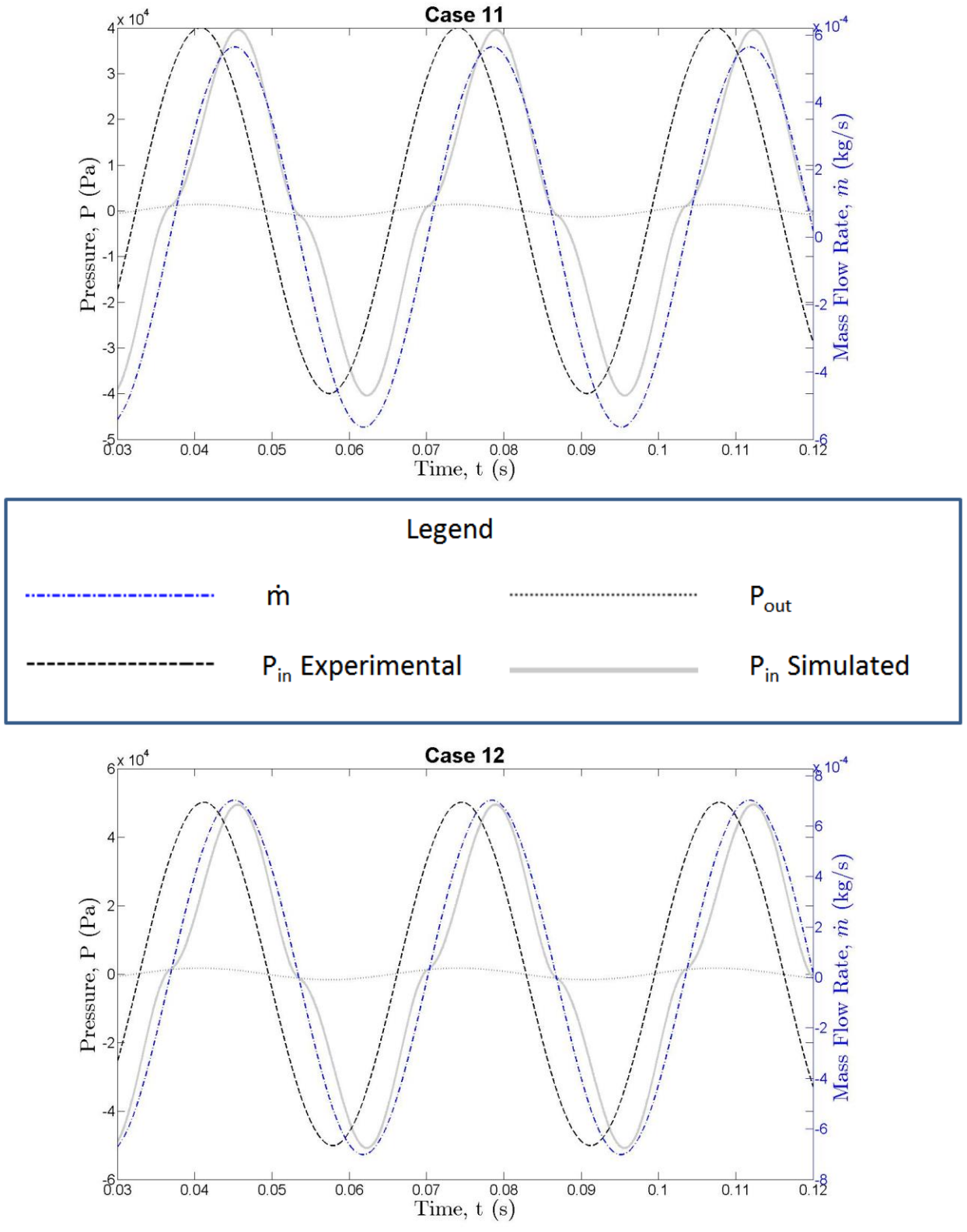

Figure 5.7. Imposed and predicted P_1, P_2, and $\dot{m}$ for periodic flow cases, Case 11-12.

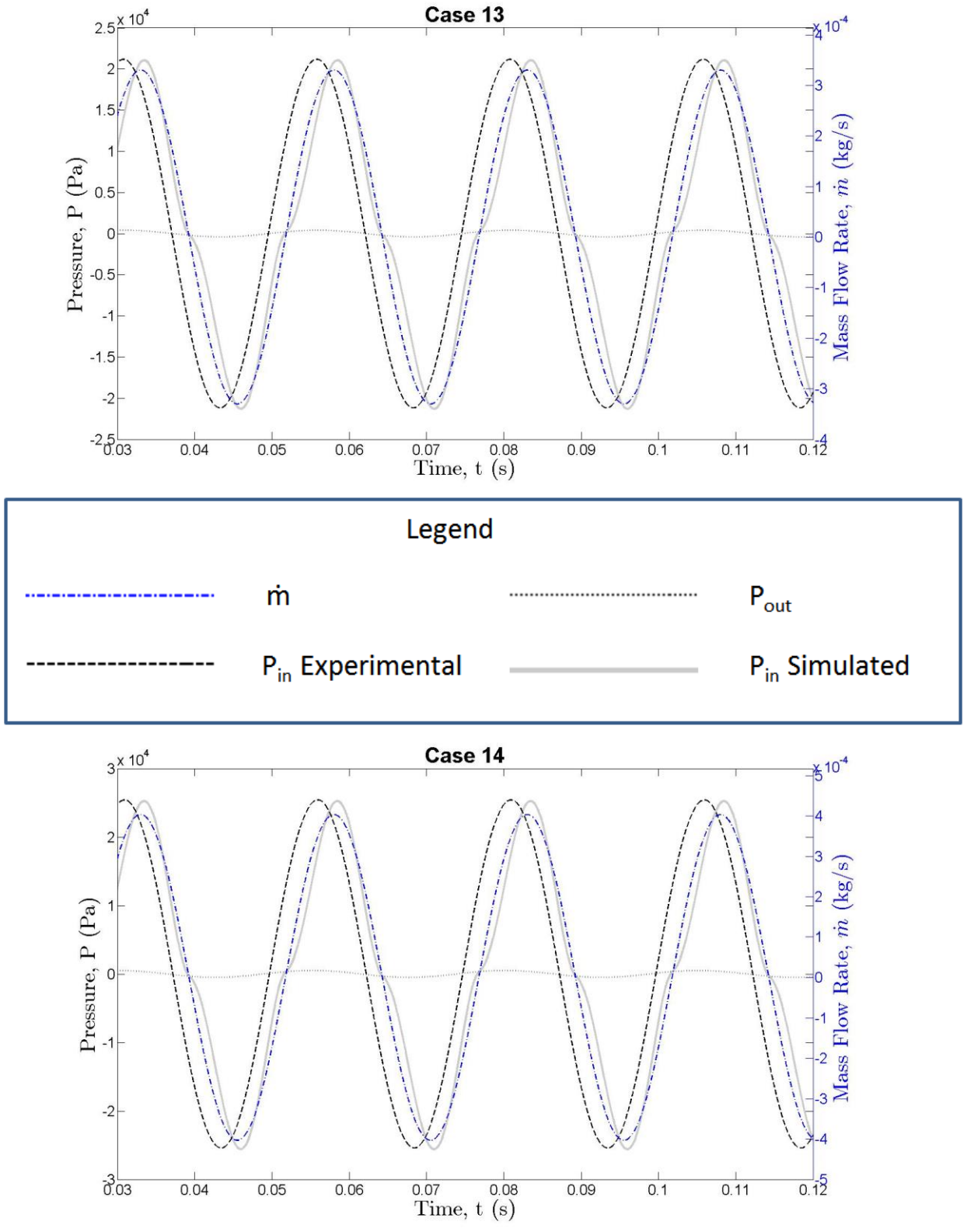

Figure 5.8. Imposed and predicted P_1, P_2, and $\dot{m}$ for periodic flow cases, Case 13-14.

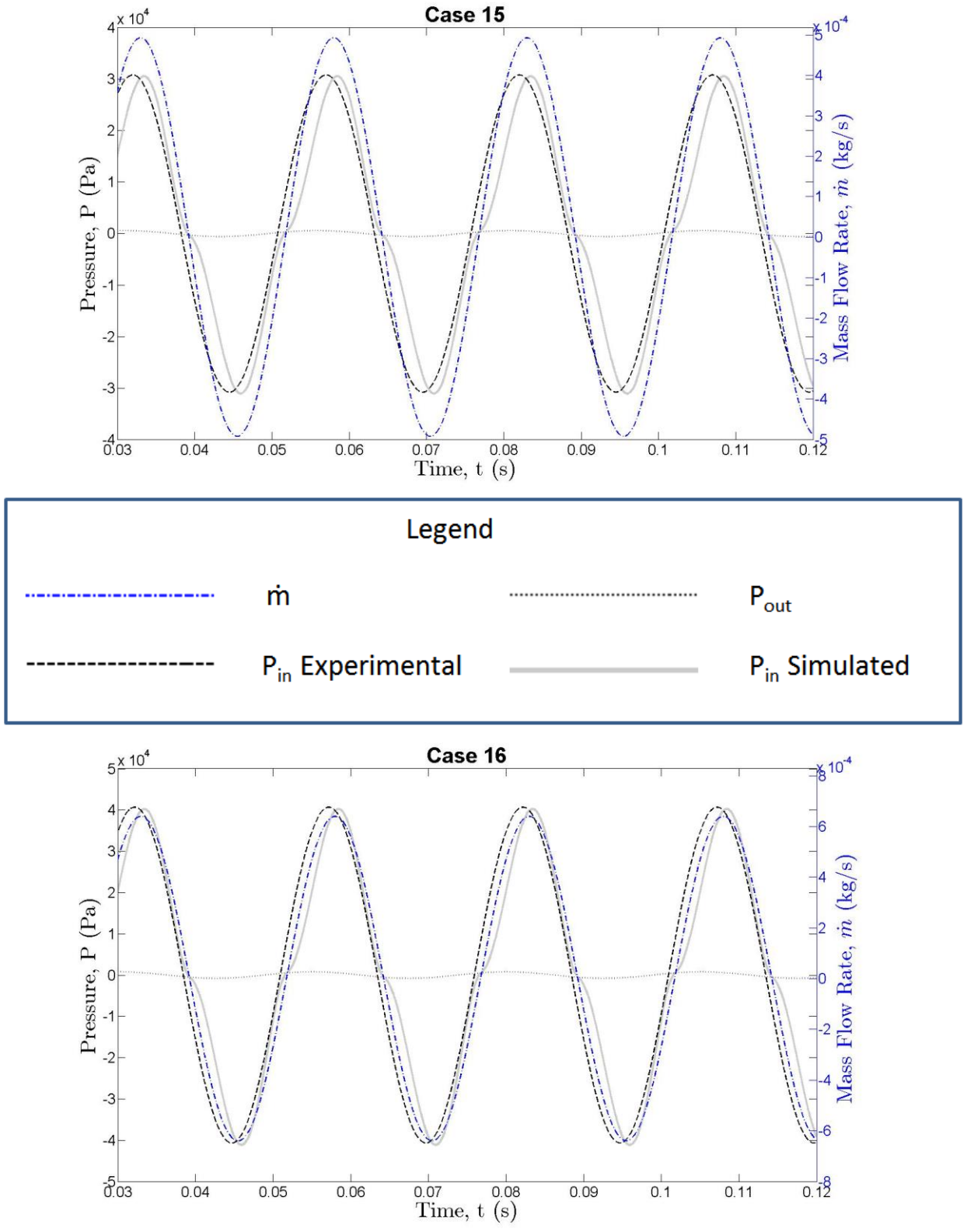

Figure 5.9. Imposed and predicted P_1, P_2, and $\dot{m}$ for periodic flow cases, Case 15-16.

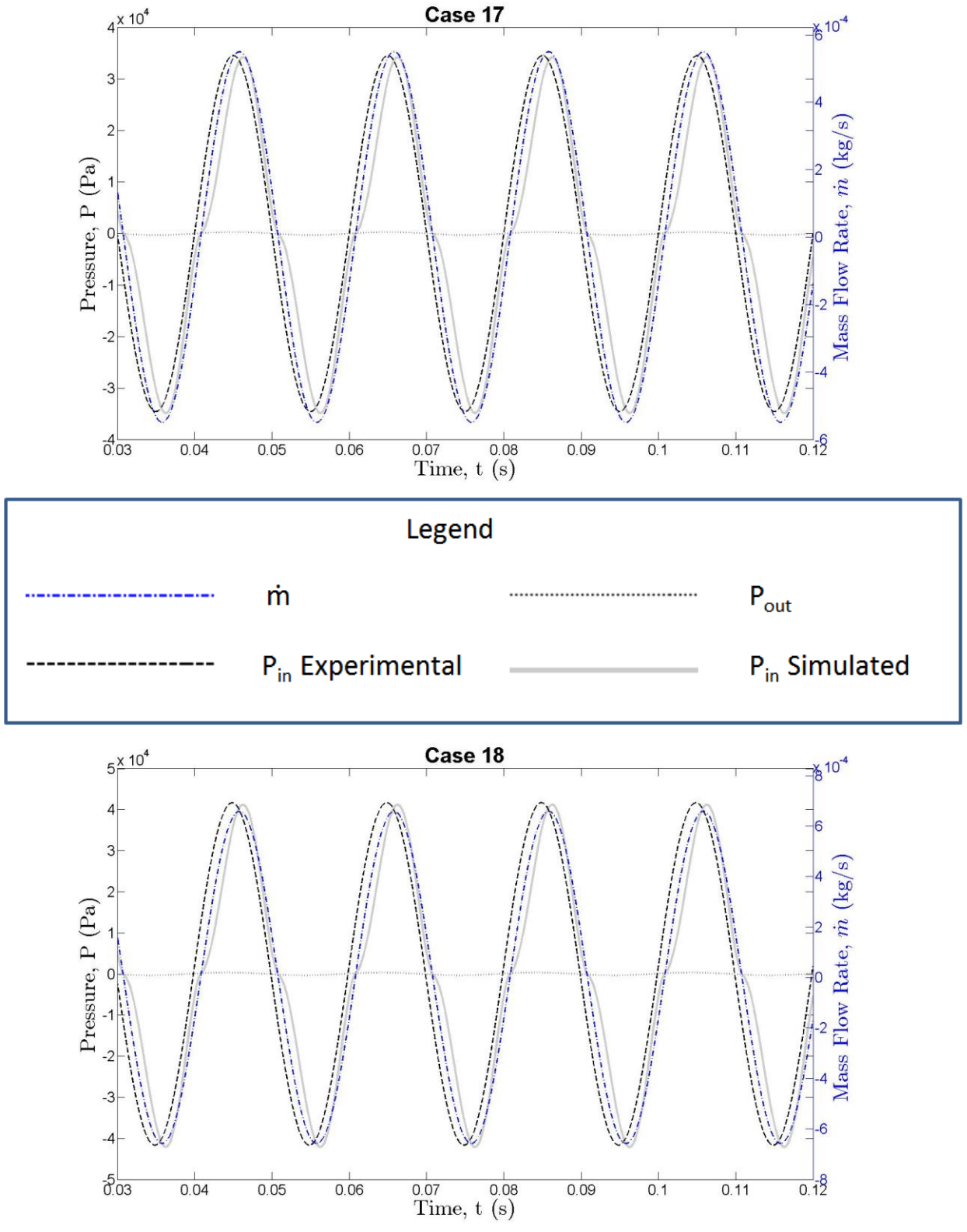

Figure 5.10. Imposed and predicted P_1, P_2, and $\dot{m}$ for periodic flow cases, Case 17-18.

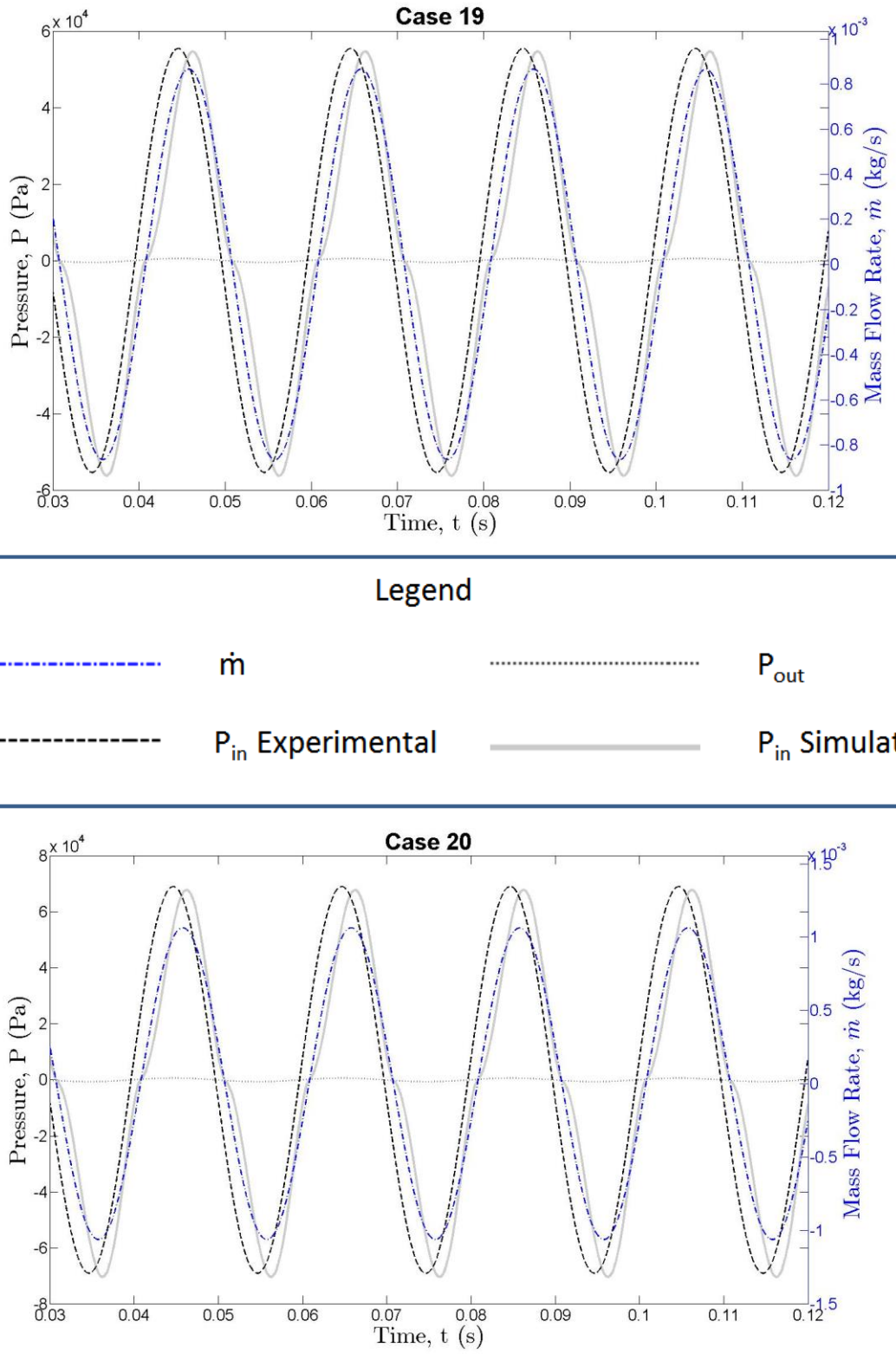

Figure 5.11. Imposed and predicted P_1, P_2, and $\dot{m}$ for periodic flow cases, Case 19-20.

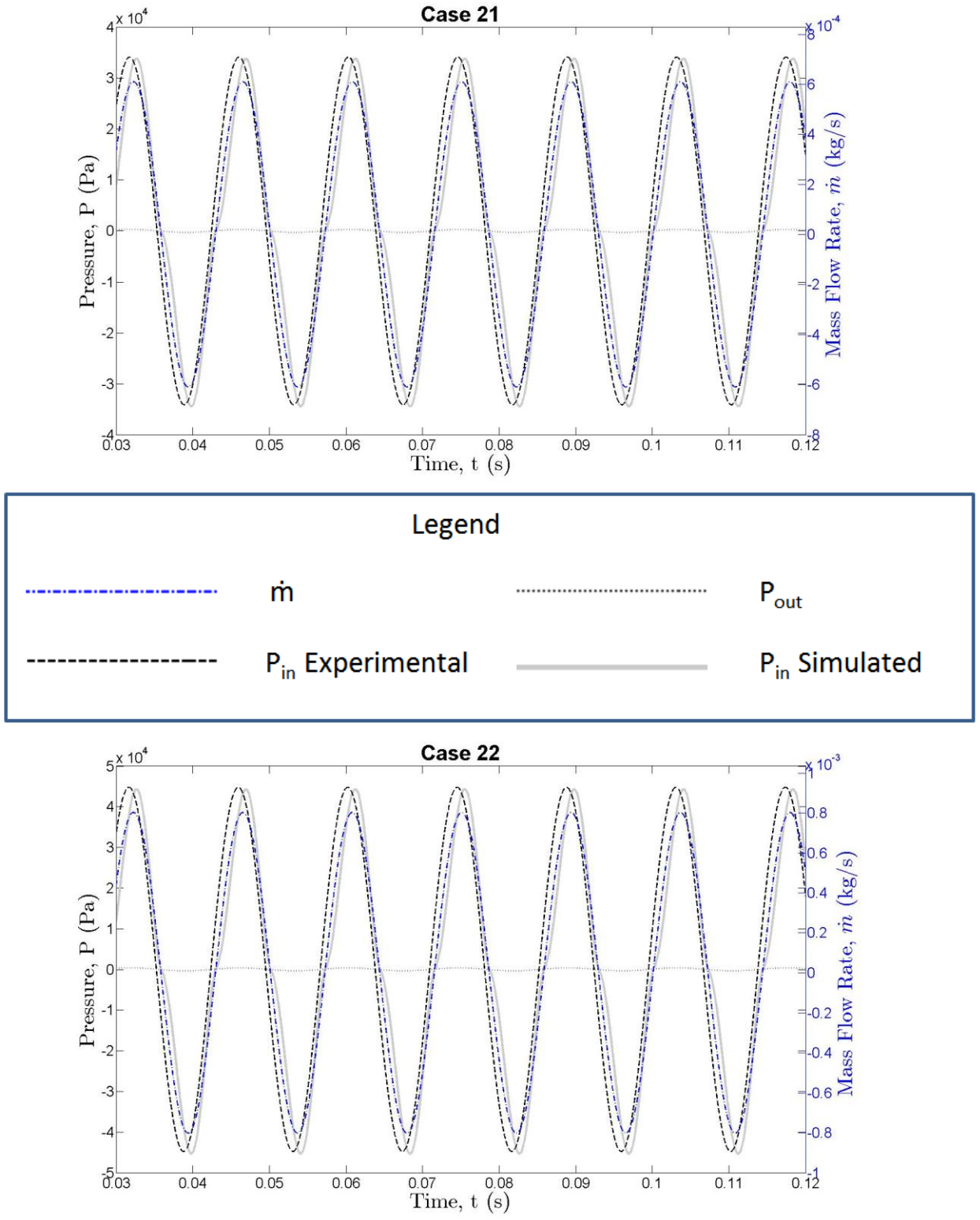

Figure 5.12. Imposed and predicted P_1, P_2, and $\dot{m}$ for periodic flow cases, Case 21-22.

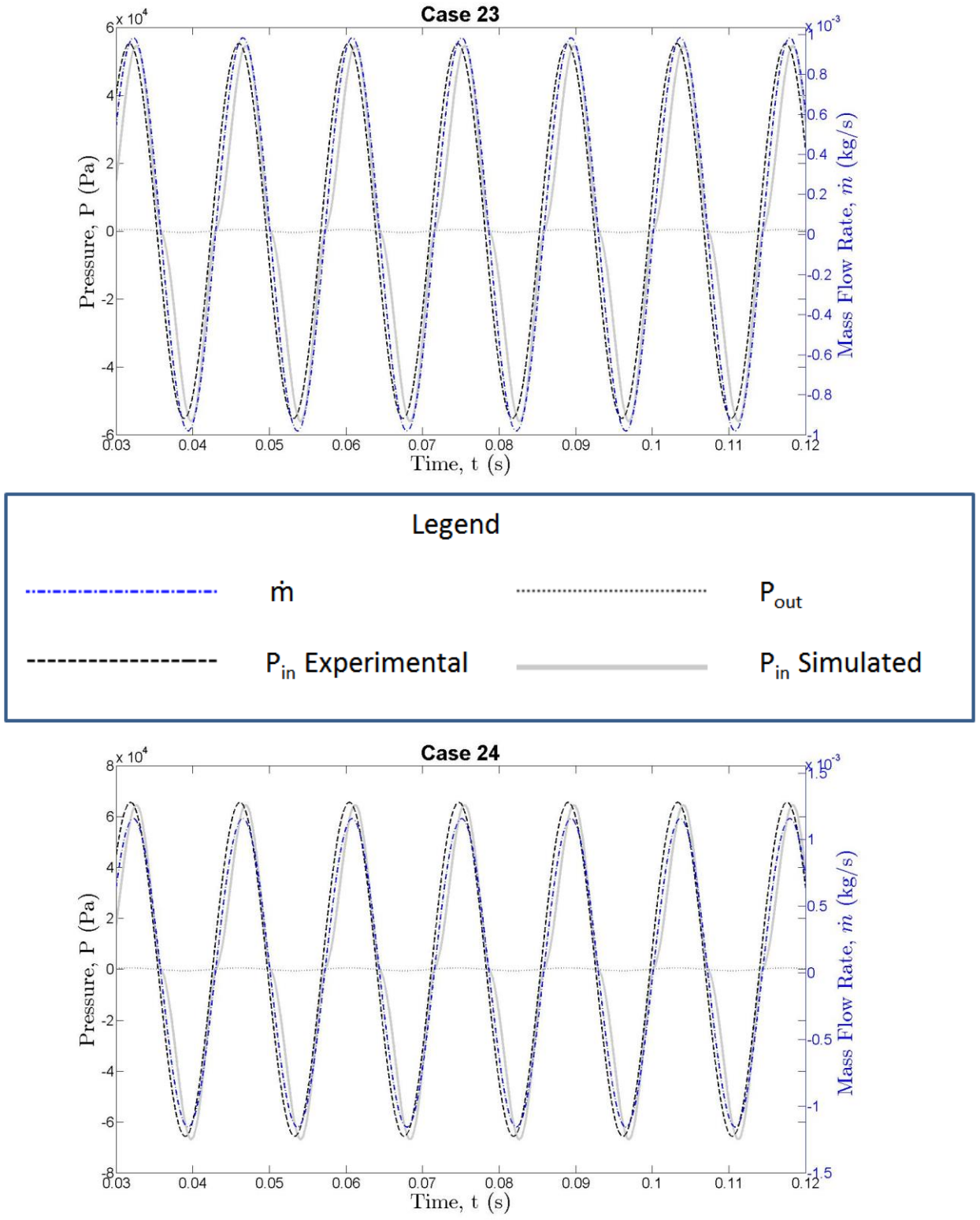

Figure 5.13. Imposed and predicted P_1, P_2, and $\dot{m}$ for periodic flow cases, Case 23-24.

CFD simulations using the aforementioned parameters led to excellent agreement with measurements. The permeability was found to be $K=1.93\times10^{-11}$ m^2, corresponding to $\beta=1.33\times10^{-10}$ m^2, for all the cases. These were identical to the values found for steady flow tests. Figure 5.14 shows the resulting c_f's as a function of Re_K.

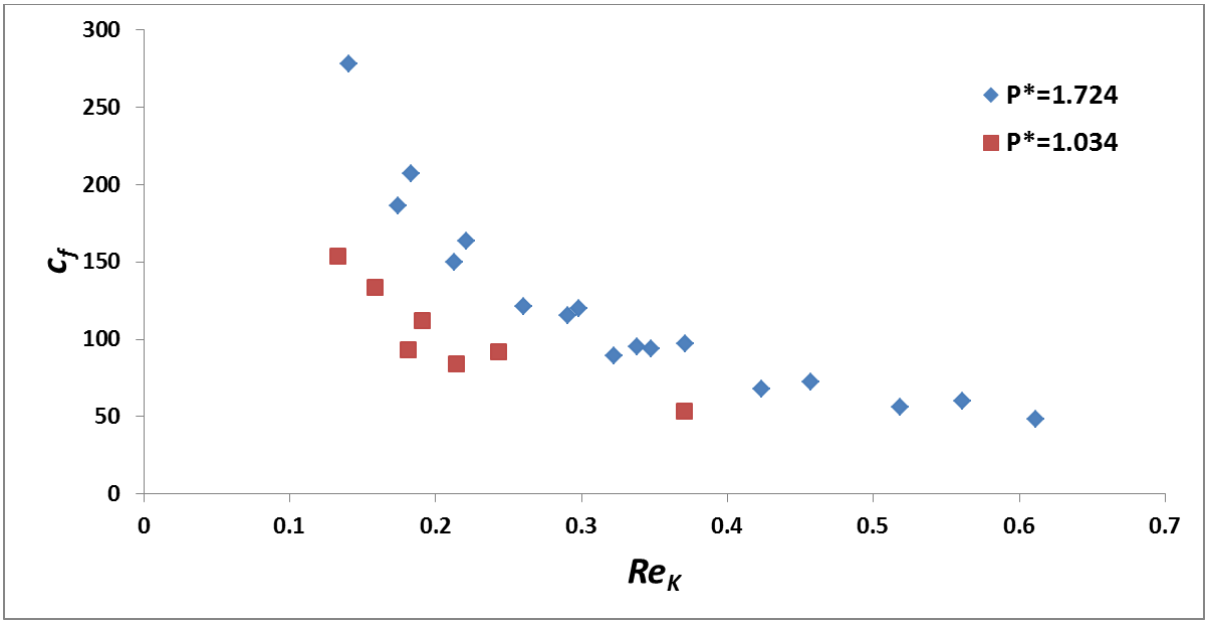

Figure 5.14. Plot of c_f as a function of Re_K for periodic flow.

The results indicate that the Forchheimer term decreases as the Reynolds number increases. Also, the magnitude of the Forchheimer term is larger for higher charge pressures. This suggests that the inertial resistance term is more significant for the flow through the ErPr regenerator filler when the mass flow rate is relatively lower in magnitude. Also, a distinct difference is seen between the steady flow and periodic flow Forchheimer terms, suggesting that the industry norm of applying the steady flow inertial resistance parameters to periodic flow models is not valid. Also, it is important to note

that the permeability term for ErPr lies within a similar range to other regenerator filler materials. The Forchheimer term, on the other hand, tends to be typically an order of magnitude or two higher than the other studied regenerator filler materials, namely, by Landrum and Cha.

5. 3 Correlations for Experimental Data

As mentioned earlier, for both the steady flow and periodic flow results, $K = 1.93 \times 10^{-11}$ m^2 was a constant. The function describing c_f was well approximated by a power correlation (found using MATLAB [Matlab (2009, [100])] as a function of the Reynolds number, of the form shown in Equation 5.1, with the determined coefficients presented in Table 5.3.

$$c_f = a \cdot {Re_K}^b + c \tag{5.1}$$

For the periodic flow cases and certain steady flow cases, where P^* (which is defined as the system charge pressure divided by a reference pressure of 1 MPa) was greater than 0.7 and Re_K was greater than 0.2, the exponent b in Equation 5.1 was a constant value of -1.4. The values of a and c, for these cases, are shown in Table 5.3.

Table 5.3. Correlation values for periodic flow cases and steady flow cases (P*>0.7 and Re_K>0.2).

Case	a	c
Periodic Flow, P*=1.034	16.2	20.6
Periodic Flow, P*=1.724	7.7	25.4
Steady Flow, P*>0.7 and Re_K>0.2	6.2	28.8

The remaining steady flow cases also followed a power function relationship, however, each curve was independently fit with unique constants as shown in Table 5.4.

Table 5.4. Correlation values for steady flow cases (P*>0.7 and Re_K<0.2, and P*<0.7 and all Re_K).

P*	a	b	c
0.345	91.9	-0.52	-119.4
0.517	0.4	-2.05	98.1
0.689	3.4	-1.38	56.4
0.862	4.7	-1.32	45.8
1.034	5.5	-1.26	43.4
1.379	3.1	-1.53	50.8
1.724	2.2	-1.71	63.4

A comparison between the actual c_f values and those predicted based on the derived correlations are presented in Figures 5.15-5.17. As seen from the figures, the correlations perform quite well relative to the experimentally determined values. Using these correlations in industry practice, can more confidently produce accurate periodic flow regenerator models compared to the state-of-the-art models used today which typically employ steady flow parameters even for oscillatory flow operating conditions.

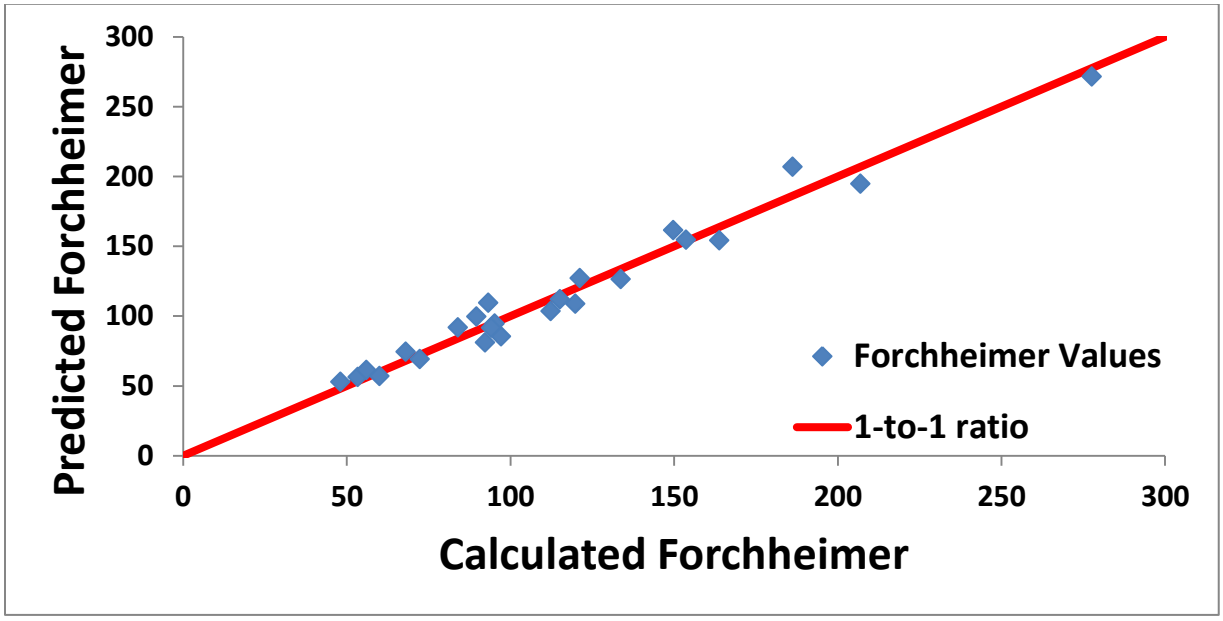

Figure 5.15. Comparison of actual and predicted correlation results for periodic flow.

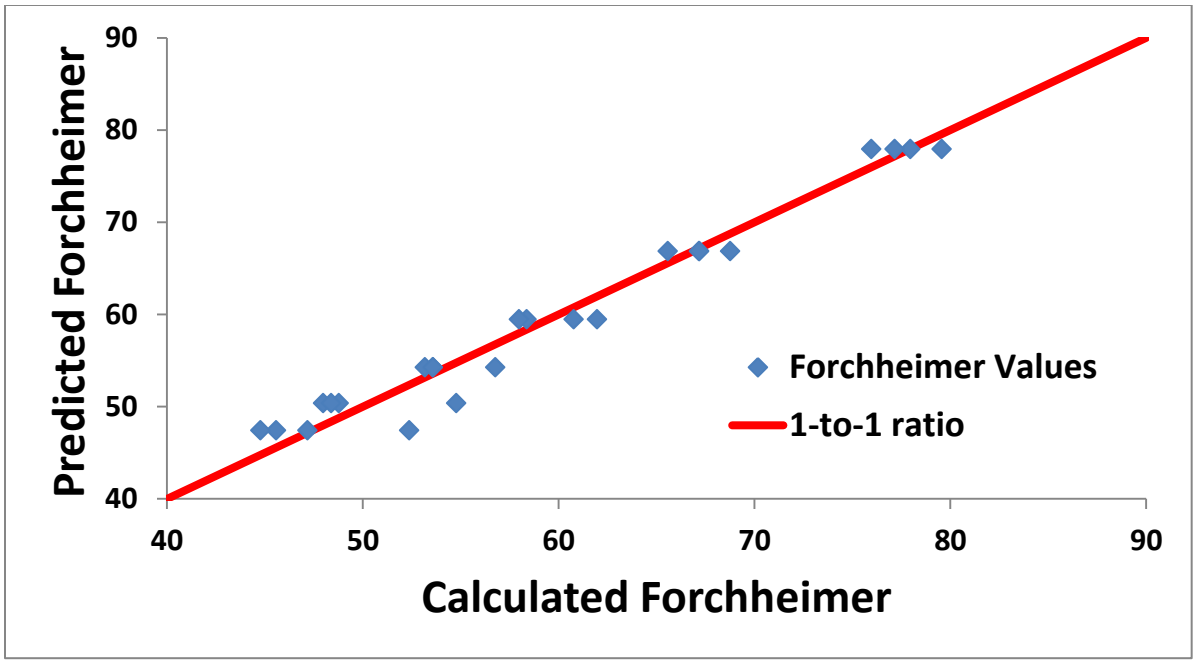

Figure 5.16. Comparison of actual and predicted correlation results for steady flow where P^*>0.7 and Re_K>0.2.

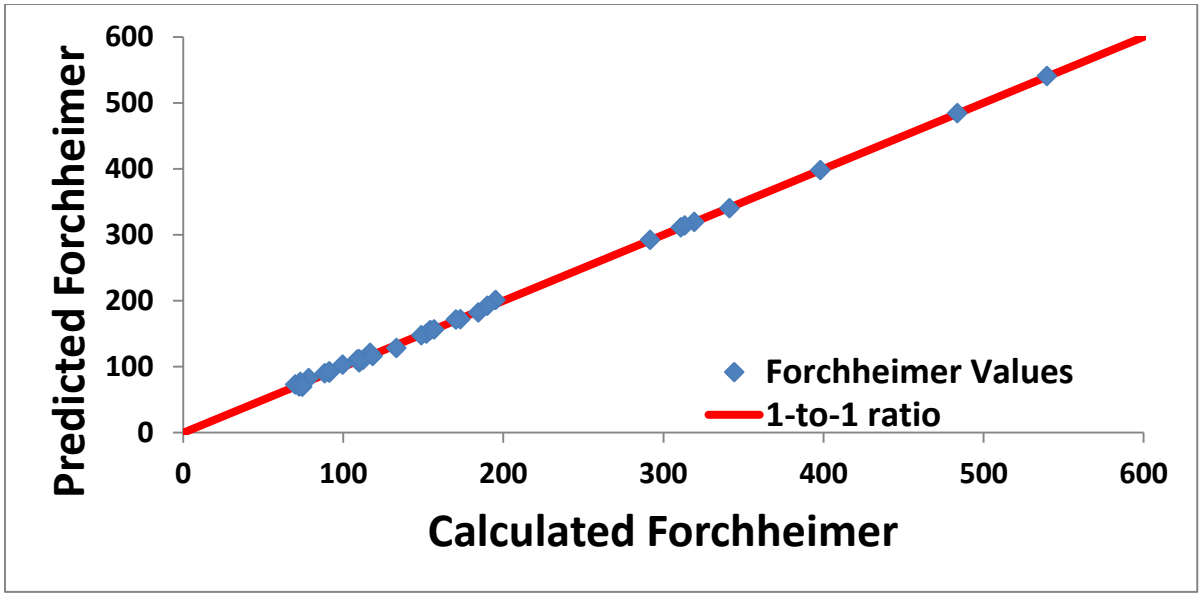

Figure 5.17. Comparison of actual and predicted correlation results for steady flow where P^*>0.7 and Re_K<0.2, and P^*<0.7 and all Re_K(bottom).

In order to compare the steady flow and periodic flow Forchheimer values, the aforementioned correlations were implemented. It was found that for the higher flow Reynolds numbers (0.2 to 0.7), the ratio of periodic flow Forchheimer value to that of steady flow, ranged from value of 2 to 1.2 respectively.

5.4 Pore-Level Phenomena

Using helium as the working fluid in the theoretical study, simulations were performed using CFD simulations according to Chapter 4. The aforementioned hydrodynamic and thermal energy parameters were then obtained, whereby the Darcy permeability, Forchheimer coefficient, and Nusselt numbers were found for both steady and oscillatory flow situations.

The micro-scale numerical calculations were continued until steady periodic conditions were reached, whereafter all calculated parameters everywhere in the simulated system were identical from one cycle to the next. Figure 5.18 shows the development of steady-periodic conditions for a typical case.

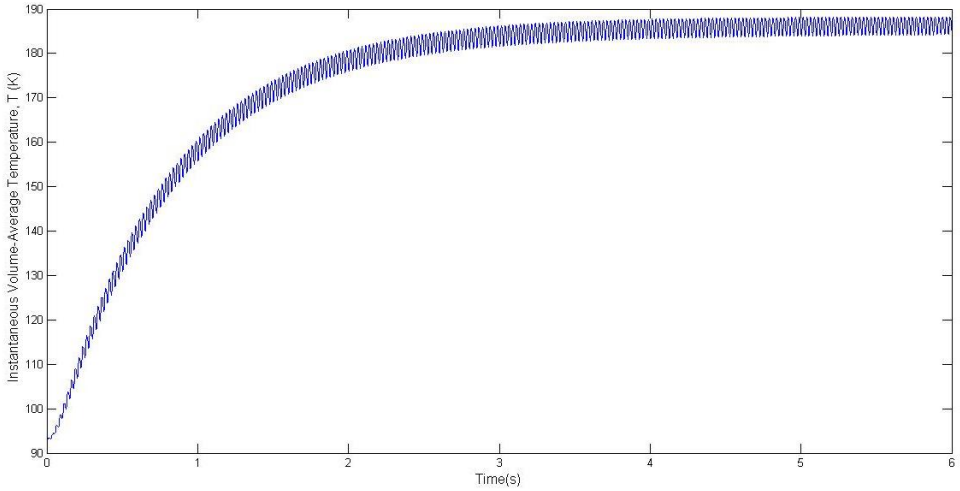

Figure 5.18. Development of steady-periodic conditions in a 40 Hz simulation in unit cell 4.

Table 5.5 is a sample summary of all the simulated runs for both steady and periodic flows, with all combinations of all parameters taken into account for the computational cases. In what follows, the hydrodynamic and thermal aspects of the investigation are discussed

.

Table 5.5. Summary of pore-level simulation results.

Case*			Steady Flow			Oscillatory Flow		
#	Amplitude	Frequency (Hz)	L^2/K	c_f	Nu_L	L^2/K	c_f	max ($Nu_L/2$)
1	Low	20	111.39	0	1.113E-03	101.59	0	0.0077
2	Low	40	93.17	0	1.124E-03	101.59	0	0.01465
3	Low	60	93.17	7.622E-01	1.135E-03	101.59	3.162E-04	0.0208
4	High	20	93.17	5.676E-01	3.457E-04	101.59	6.420E-03	0.0212
5	High	40	93.17	3.691E-01	3.707E-04	101.59	6.723E-03	0.0353
6	High	60	93.17	2.539E-01	3.965E-04	101.59	3.750E-03	0.0353

* For the definition of high and low amplitudes, see Section 4.3.1.

It is clear that the hydrodynamic and thermal parameters associated with steady flow differ from those associated with oscillatory flow. The permeability term is similar for both flow cases, however the Forchheimer term varies by a factor of 10^2. Also the Nusselt number drastically varies between the two flow conditions. This study qualitatively agrees with the experimental results obtained from the investigation discussed in the previous section, thus reaffirming the validity of the results.

In oscillatory flow, the phase difference between pressure and mass flow rate greatly affects the overall hydrodynamics and hence the thermal attribute of the system. In fact, this phase lag is the crucial phenomenon that makes pulse tube cryocooling possible. Figures 5.19 – 5.30, display the phase differences for all of the simulated cases, where each plot corresponds to a case number shown in Table 5.5. The plots suggest that the heat transfer and temperature are approximately in phase, whereas the heat transfer and velocity seem to be almost out of phase. The phase difference between pressure and

velocity, and velocity and temperature greatly impact the performance of cryogenic regenerators and heat exchangers.

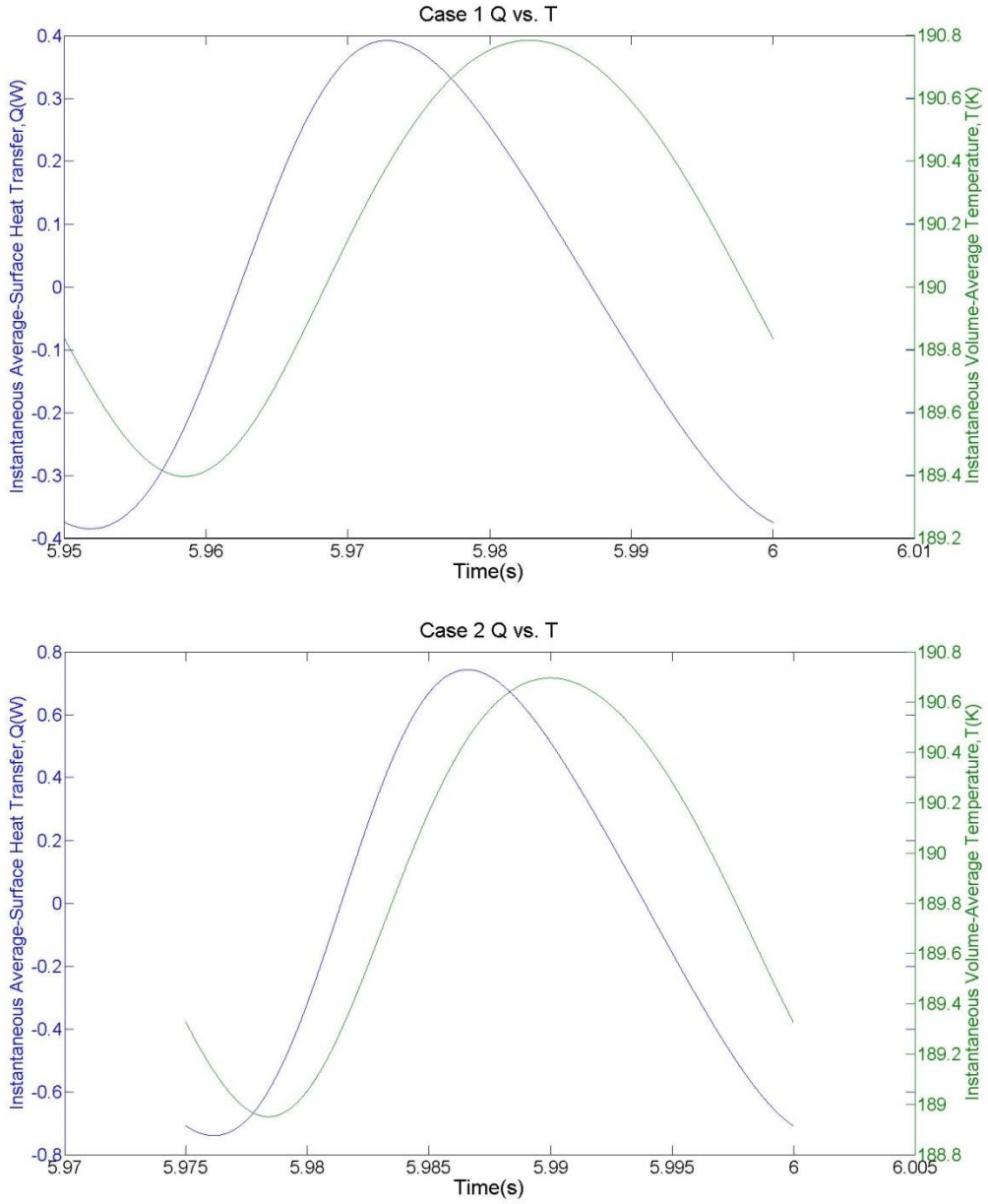

Figure 5.19. Profiles of heat transfer and temperature – Case 1-2.

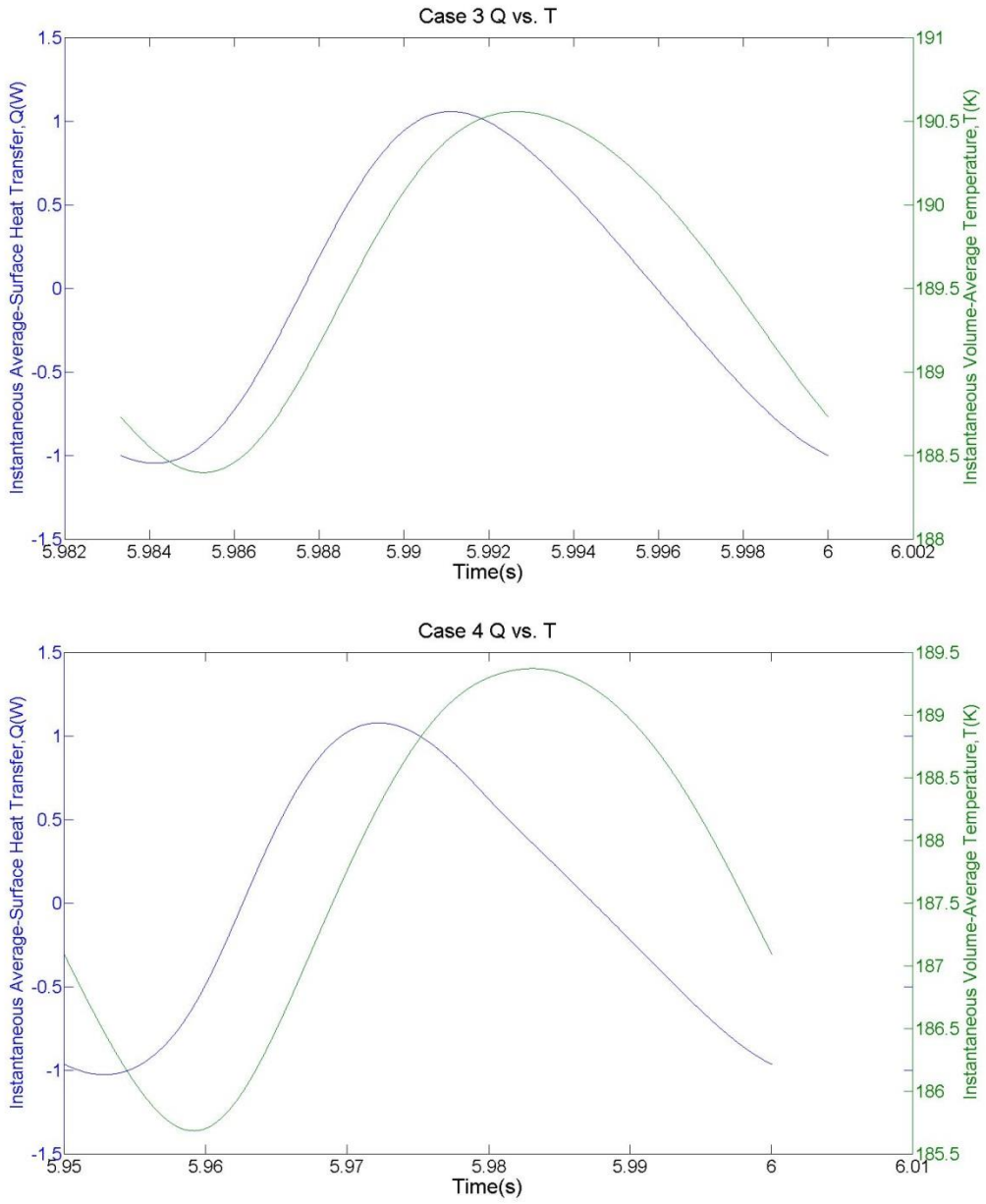

Figure 5.20. Profiles of heat transfer and temperature – Case 3-4.

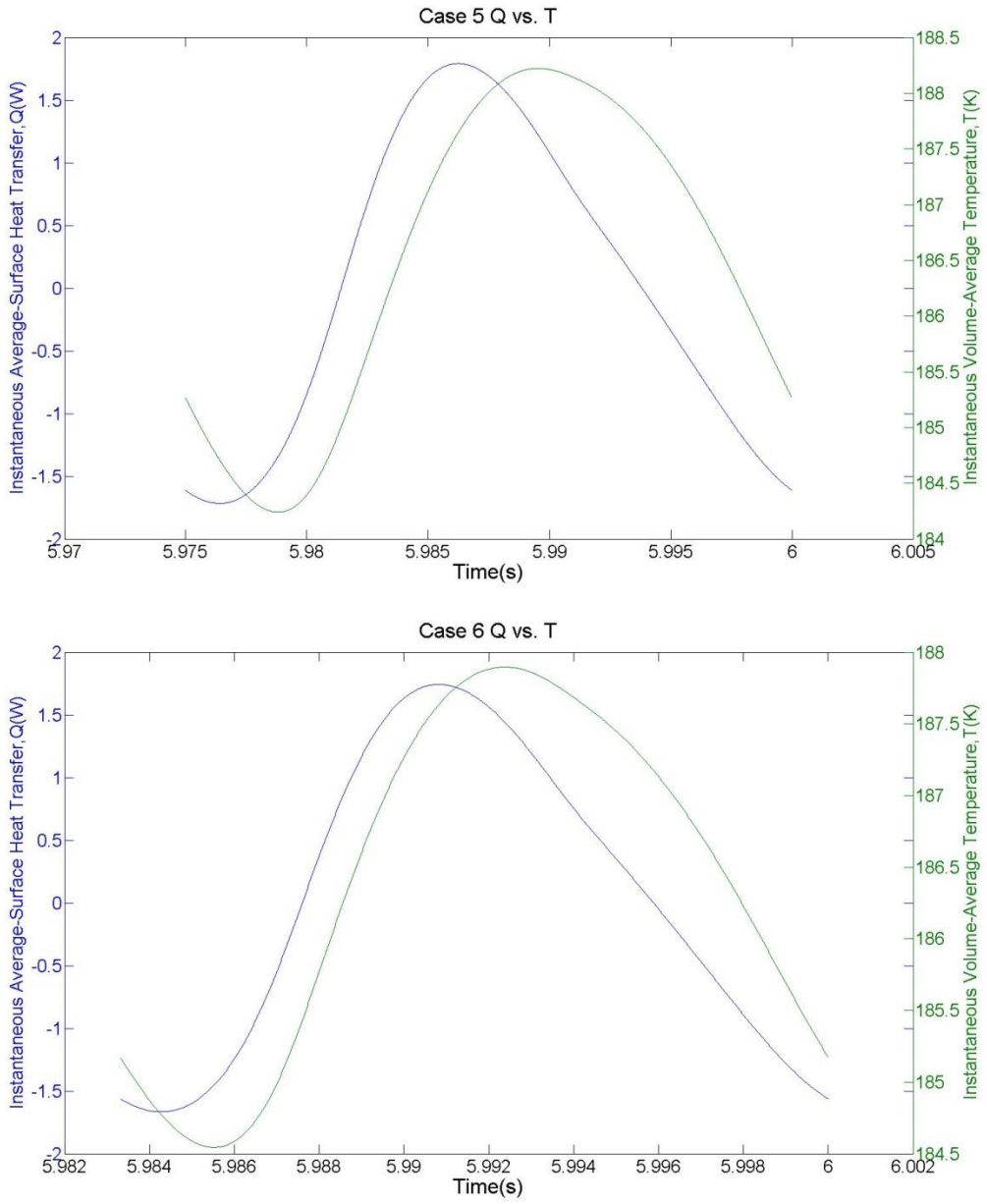

Figure 5.21. Profiles of heat transfer and temperature – Case 5-6.

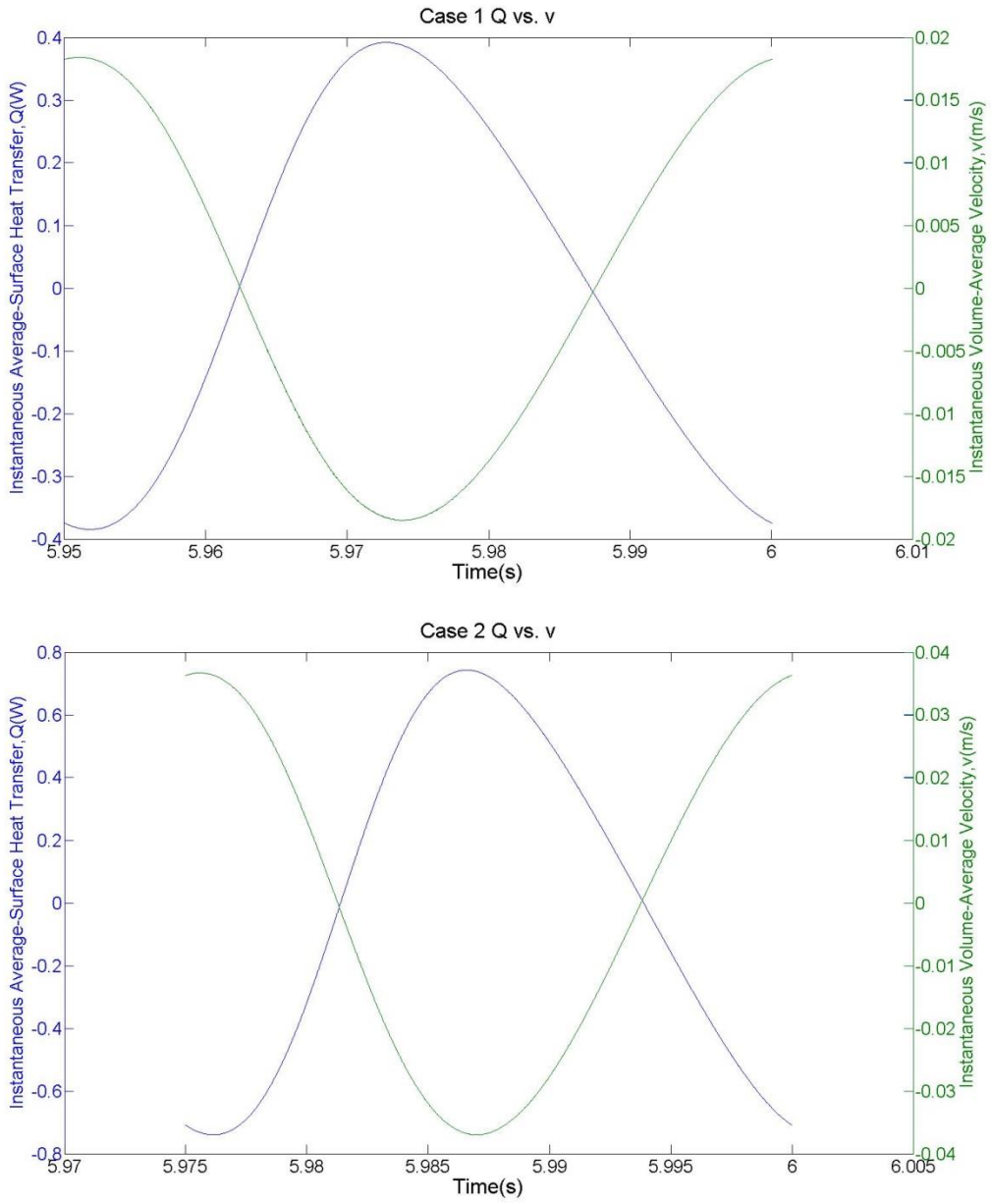

Figure 5.22. Profiles of heat transfer and velocity – Case 1-2.

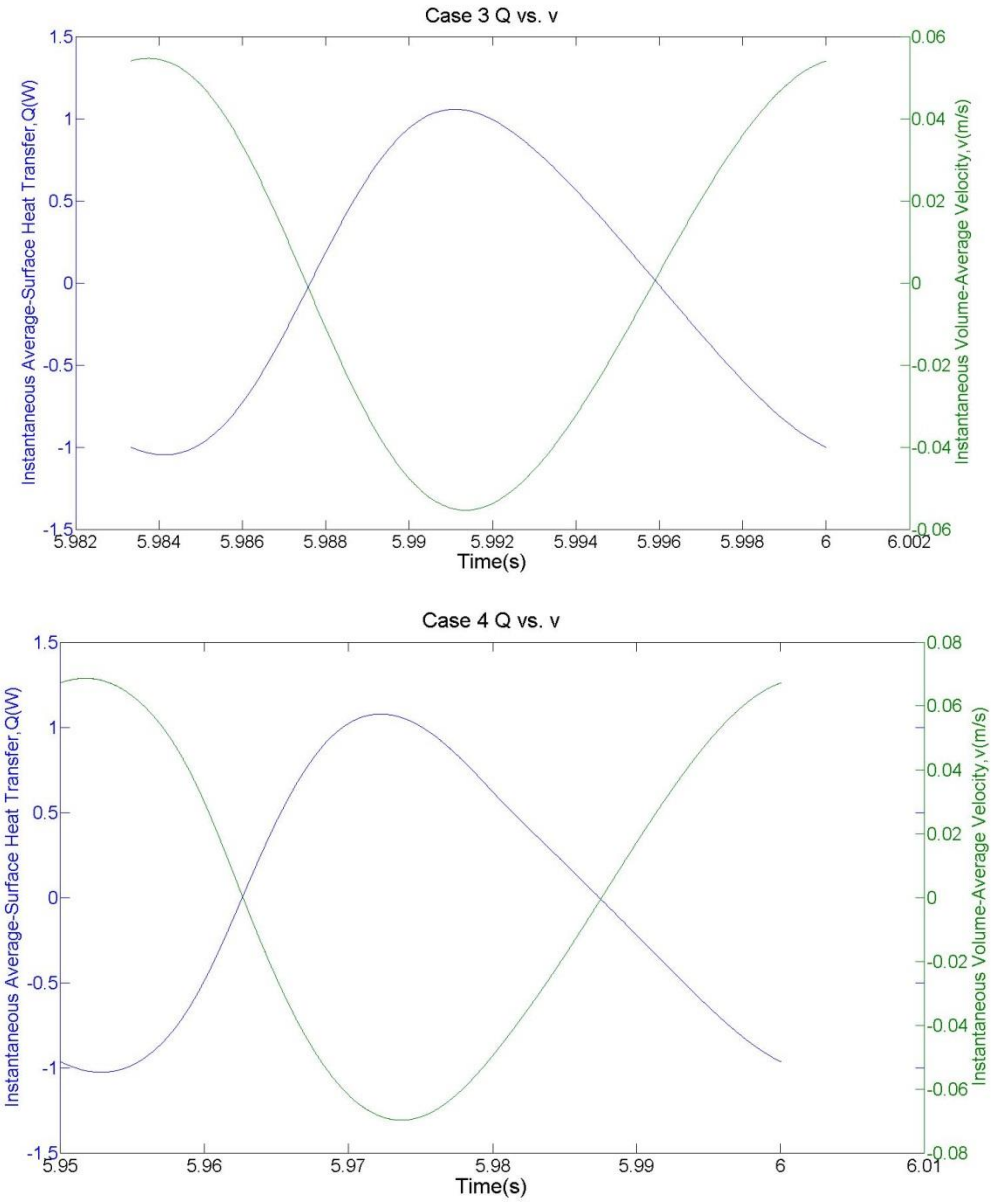

Figure 5.23. Profiles of heat transfer and velocity – Case 3-4.

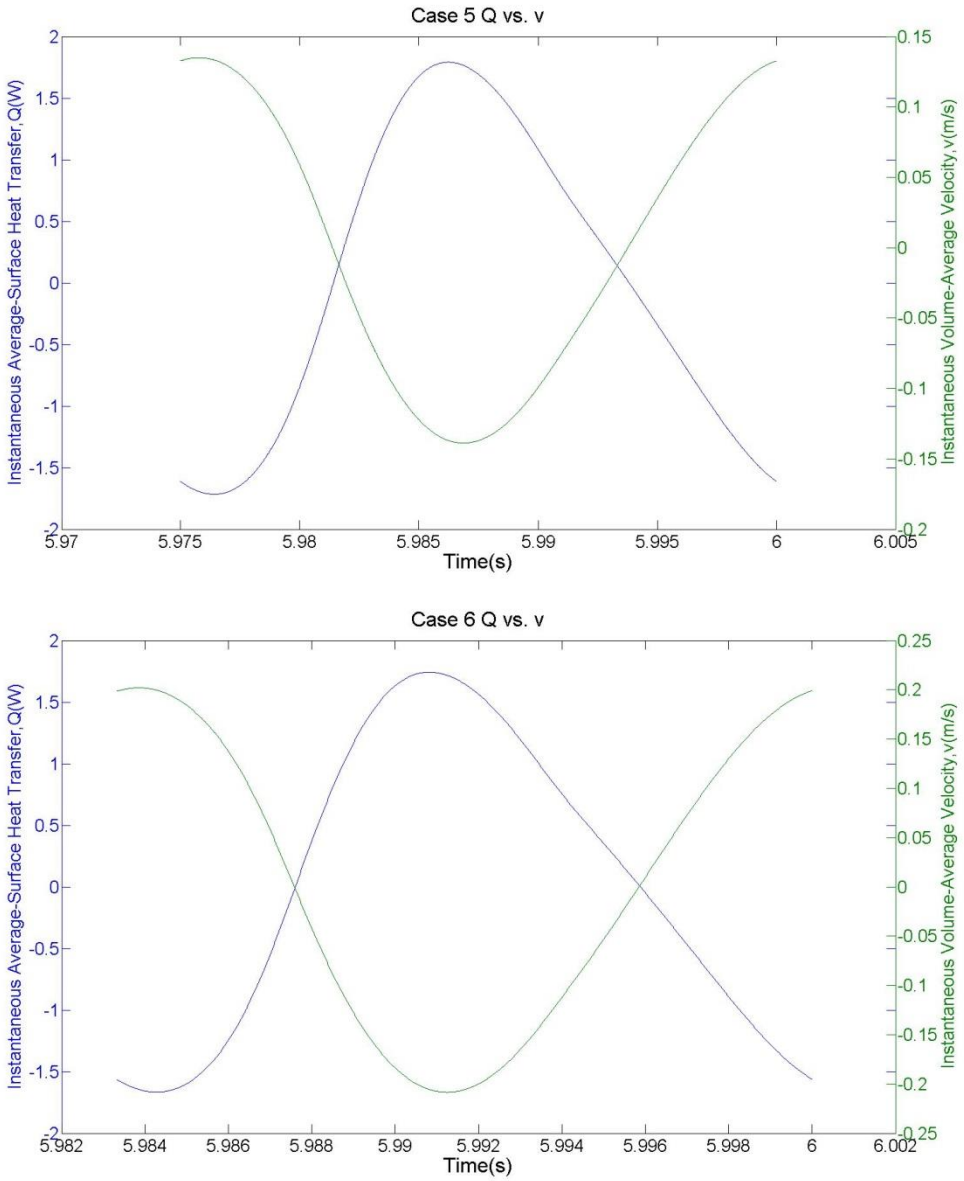

Figure 5.24. Profiles of heat transfer and velocity – Case 5-6.

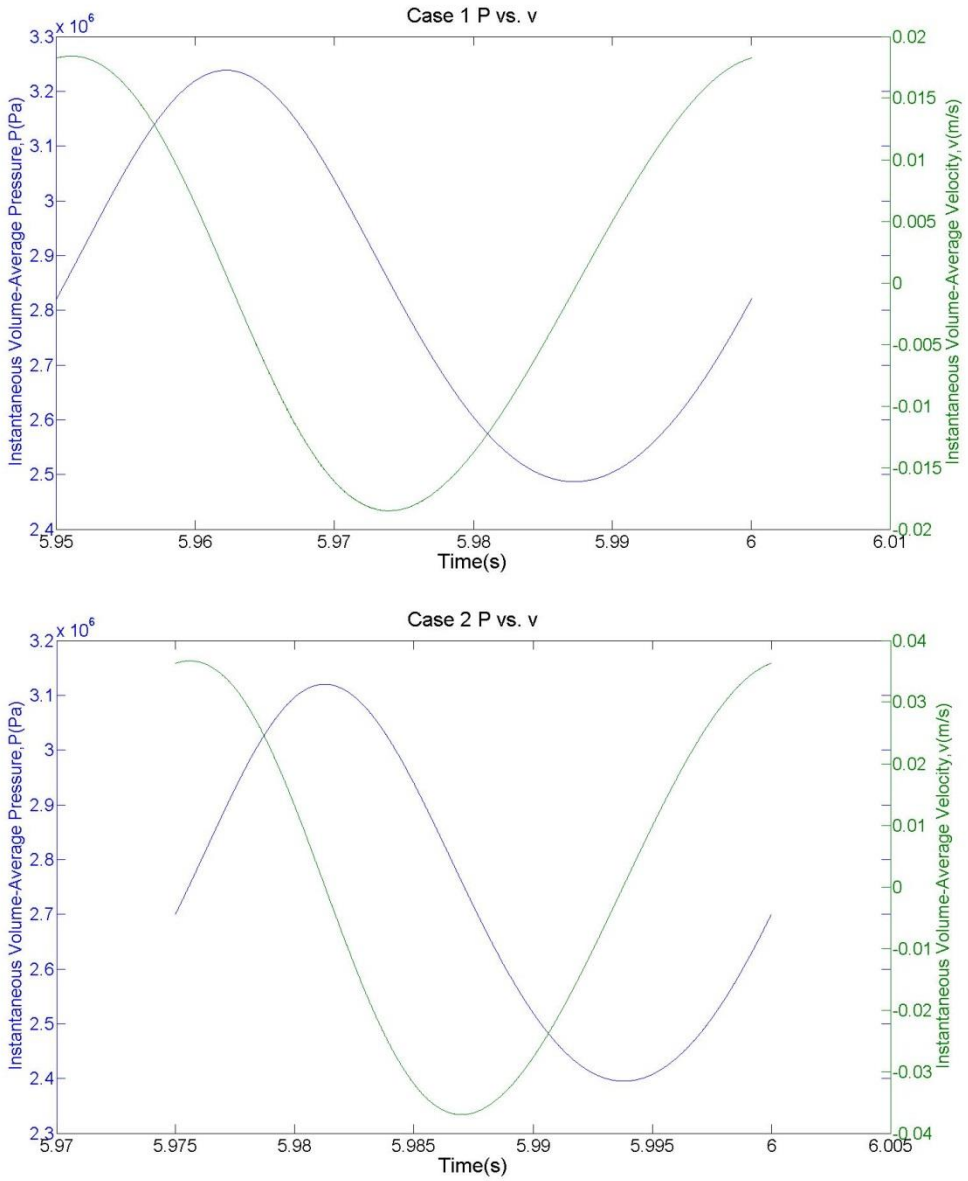

Figure 5.25. Profiles of pressure and velocity – Case 1-2.

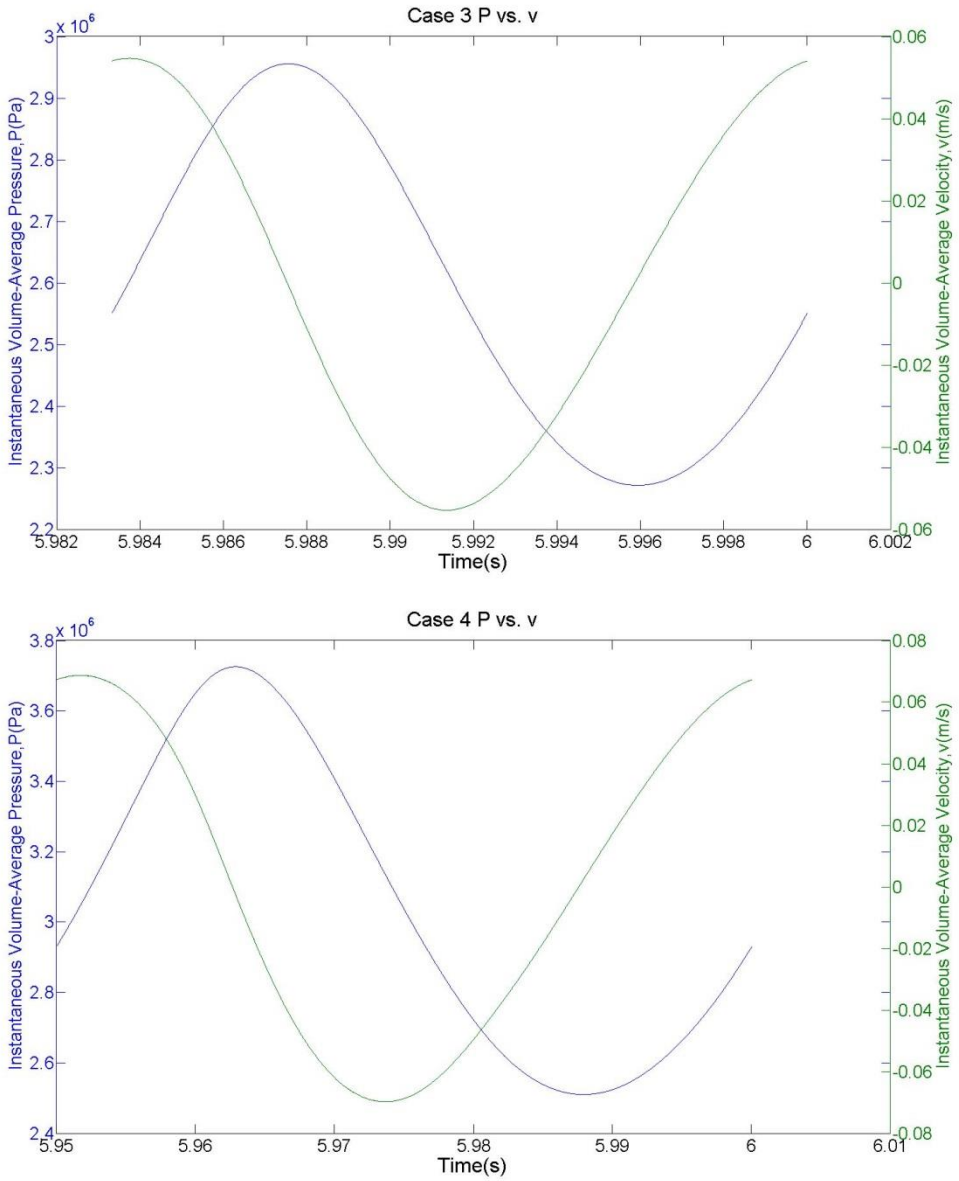

Figure 5.26. Profiles of pressure and velocity – Case 3-4.

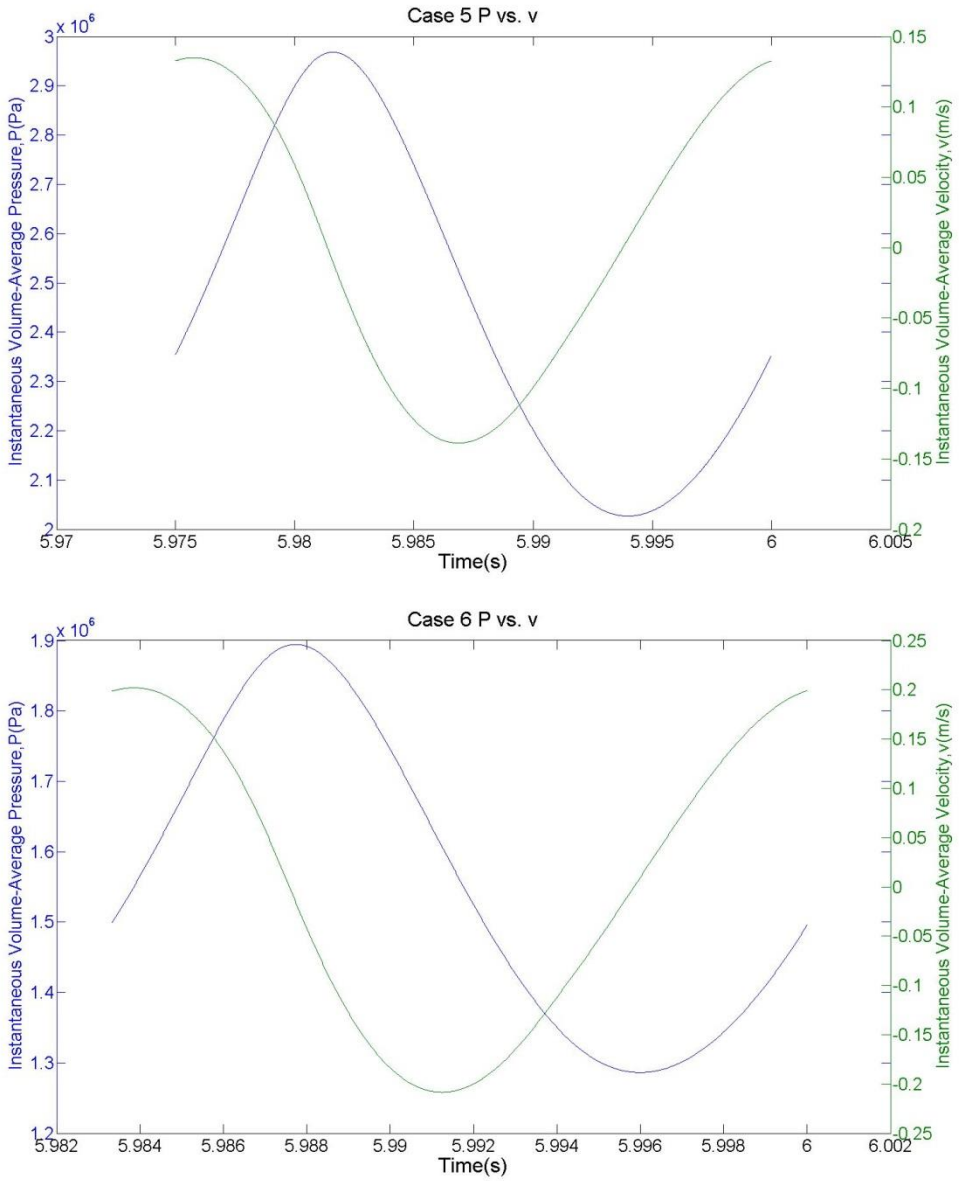

Figure 5.27. Profiles of pressure and velocity – Case 5-6.

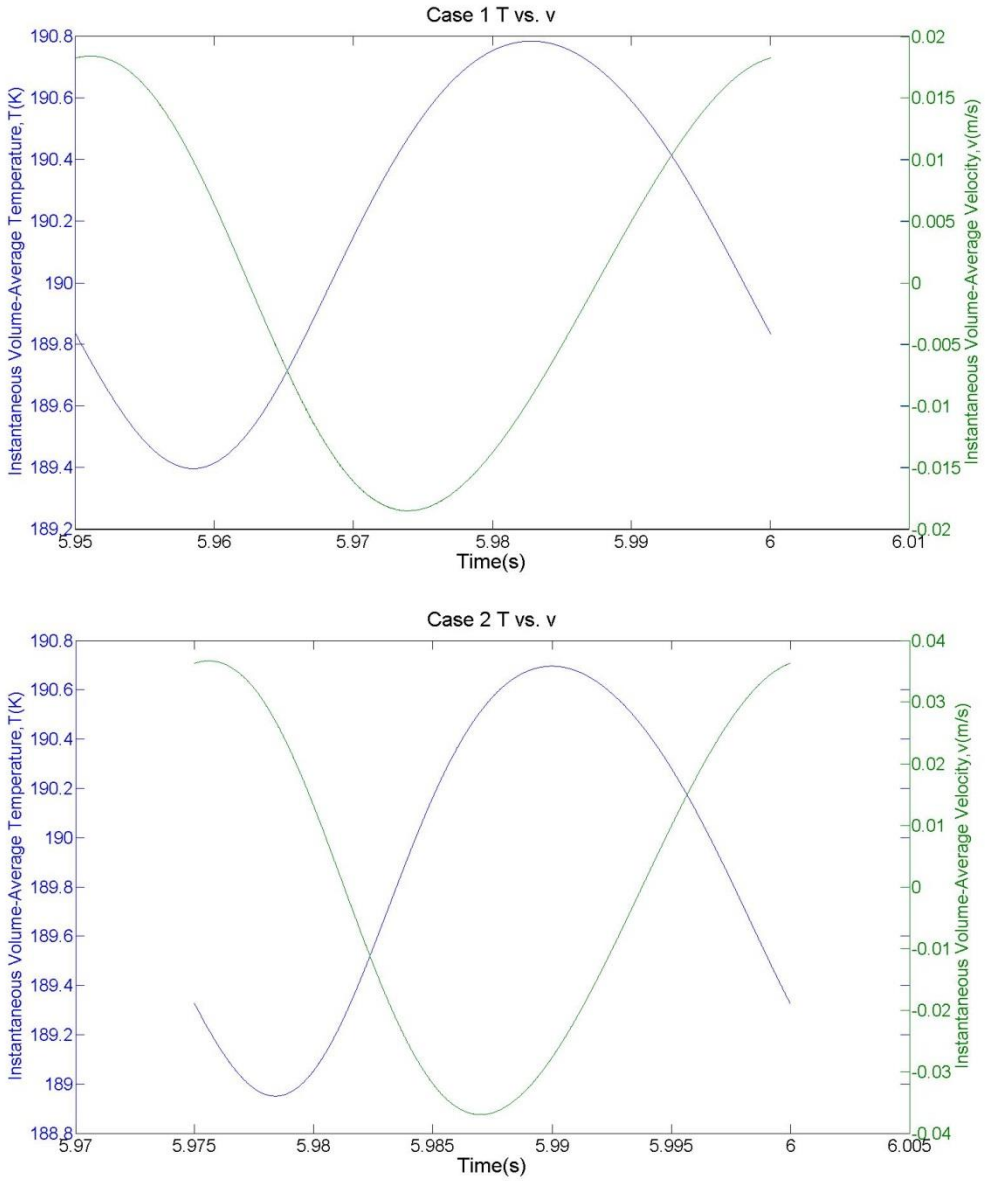

Figure 5.28. Profiles of temperature and velocity – Case 1-2.

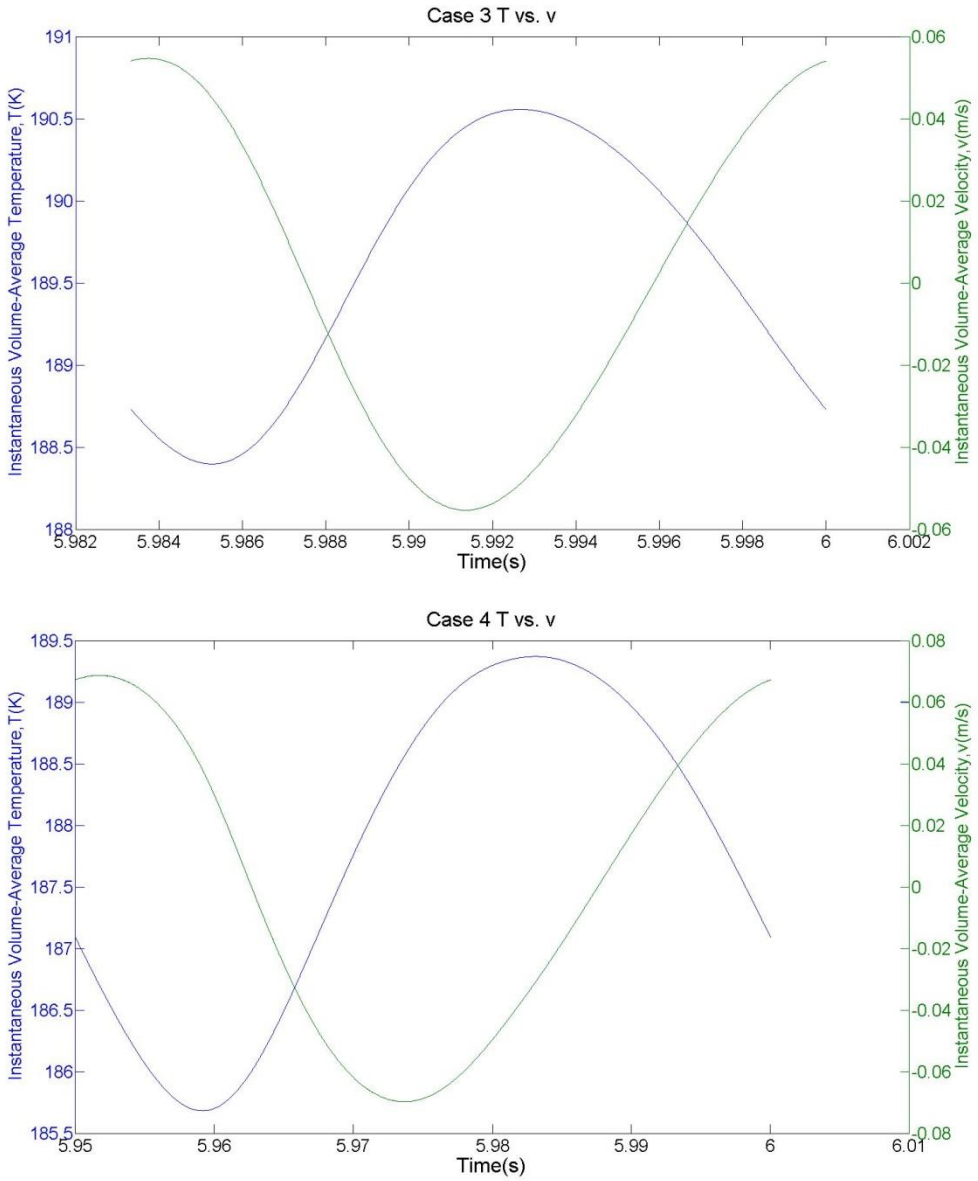

Figure 5.29. Profiles of temperature and velocity – Case 3-4.

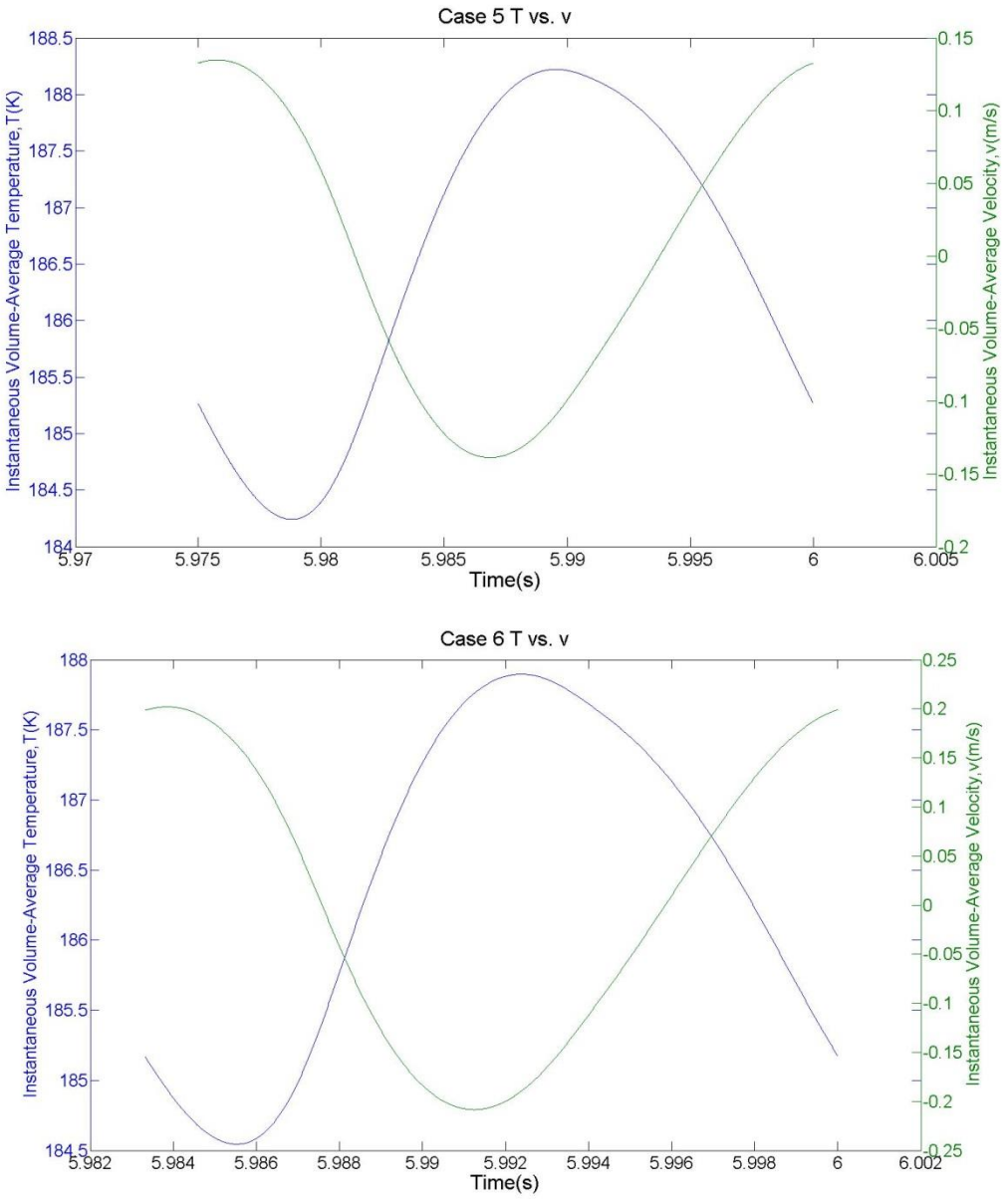

Figure 5.30. Profiles of temperature and velocity – Case 5-6.

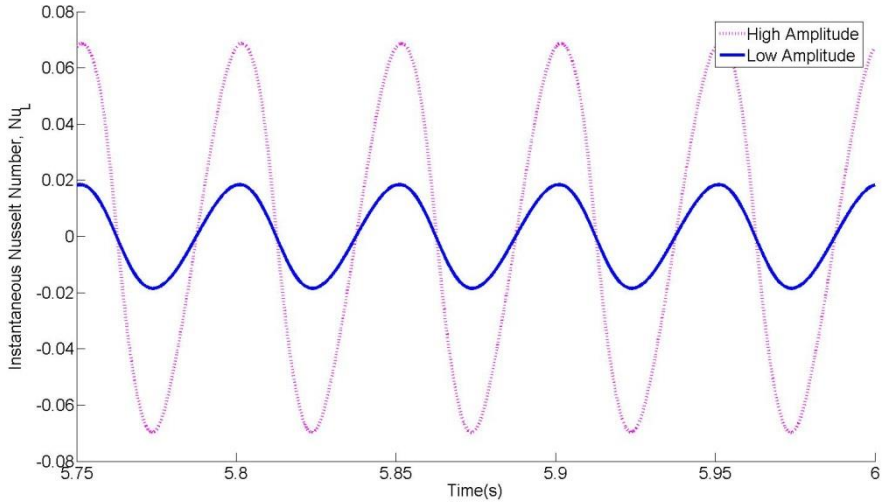

Figure 5.31. Nusselt numbers for 20 Hz.

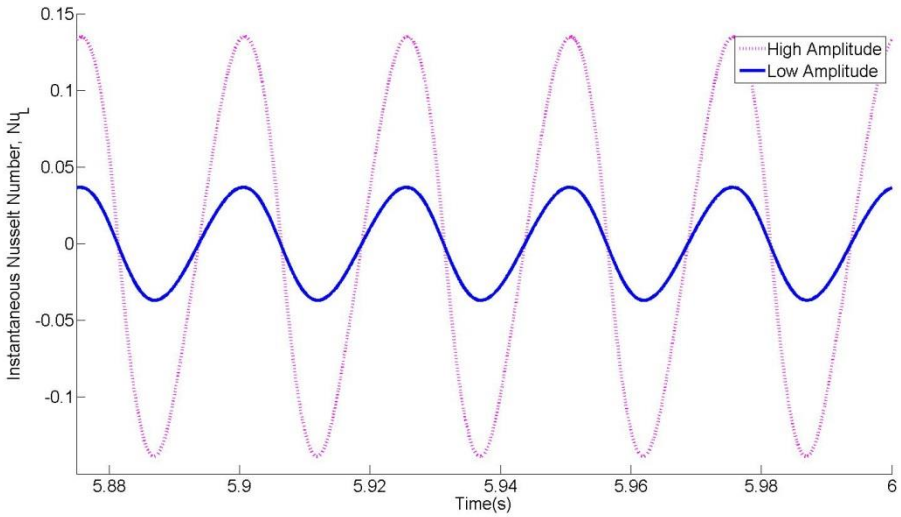

Figure 5.32. Nusselt numbers for 40 Hz.

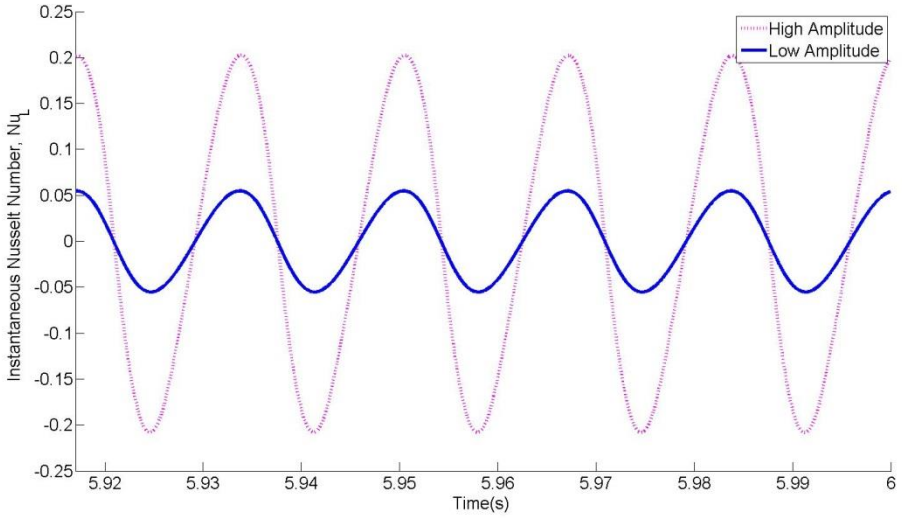

Figure 5.33. Nusselt numbers for 60 Hz.

The resulting instantaneous volume-average Nusselt numbers are shown in Figures 5.31-5.33. At higher frequencies the Nusselt number experiences higher amplitudes for both high amplitude and low amplitude flow cases. As the Reynolds number increases, the Nusselt number also increases except for the highest amplitude and highest frequency case. This is thought to have happened because of the phase relationship for the highest Reynolds case. Similar effects are also seen for the Forchheimer term.

From these results it is clear that the steady flow hydrodynamic and thermal parameters greatly differ from that of periodic flow, particularly the Forchheimer inertial term and the Nusselt number. This observation is consistent with the results of the experimental investigation discussed in the previous sections.

CHAPTER 6

CONCLUSIONS AND RECOMMENDATIONS

This final chapter concludes the dissertation investigation and provides the resulting conclusions from both the pore-level theoretical study and the experimental regenerator filler study. The associated contributions from this work are then discussed. The chapter concludes with suggestions for future work associated with this investigation.

6.1 Conclusions

A systematic experimental and CFD-based study for the quantification of Darcy permeability and Forchheimer's coefficients for porous structures that appear in the volume-averaged porous media momentum transport equation, under steady and periodic flow conditions, was carried out. In the investigation, the hydrodynamic resistance flow parameters for $Er_{50}Pr_{50}$ rare-earth powder regenerator filler material, which is useful for pulse tube and Stirling cryocoolers at low temperature, high heat load capacity applications, was found.

The porous regenerator filler was made of spherical particles with an average diameter of 69 μm and a porosity of 38%. In the periodic flow tests the time variations of pressures were measured in an apparatus that consisted of a modular regenerator housing containing a porous regenerator, for inlet pressure oscillations with 30–70 Hz frequencies at various charge pressures and piston strokes. Also, the pressure drop across the regenerator was collected for steady flow tests for a variety of charge pressures and mass flow rates.

By systematic and iterative CFD simulations, the aforementioned hydrodynamic parameters were optimized leading to excellent agreement between simulations and experimental measurements for the tested regenerator filler, yielding useful correlations. The correlations followed a power function, with varying coefficients based on the type of flow and the flow conditions. The results showed that the Darcy permeability term was constant for both steady flow and periodic flow cases and with the exception of the low flow rate, low charge pressure steady-flow cases. The Forchheimer coefficient, however, varied based on the flow conditions and followed a consistent power model correlation as a function of the pore based Reynolds number.

A pore-level numerical investigation of the hydrodynamics and thermal energy associated with steady and periodic flow in porous media was also conducted in this investigation. Two-dimensional, laminar flow in a generic porous medium consisting of a periodic array of square cylinders with conjugate heat transfer conditions was simulated using Ansys Fluent CFD code.

These simulations were based on fine nodalization and the resolution of pore-scale phenomena, and covered frequencies of 0 ~ 60 Hz at two distinct piston amplitudes. The detailed numerical data were used for the calculation of unit cell and cycle-average Darcy permeability, Forchheimer term, and Nusselt number, which appear in the standard volume-average momentum and thermal energy transport equations for flow in porous media. These terms, under periodic conditions, were sensitive to frequency and amplitude, and were significantly different from their counterparts that represented steady flow.

Both the numerical pore-level theoretical investigation and the experimental regenerator filler study yielded similar results proving that steady flow parameters could not be substituted into periodic flow models without significant associated errors.

6.2 Contributions

Three significant contributions have been made in this research. One particular significant contribution of this investigation was the successful measurement and correlation of the hydrodynamic resistance parameters under steady and oscillatory flow conditions using a CFD-assisted methodology. The proposed methodology simulates the experiments using exact measured mass flow rate and pressure waveforms on ErPr rare-Earth regenerator filler material. Rare-Earth regenerator filler material is typically employed for low temperature, high heat load capacity pulse tube and Stirling cryocoolers. Prior to this investigation, only those regenerator filler materials typically employed on higher temperature cryocoolers (80 K and above) have been investigated. Also, this investigation provides empirical correlations for researchers and designers to employ more accurate hydrodynamic resistance parameters when modeling regenerative cryocoolers with ErPr rare-Earth regenerator filler material.

The second significant contribution is the numerical periodic flow pore level conjugate heat transfer model, which is a first of its kind. Previous work dealing with direct simulation of flow in porous media has been limited to steady flow modeling or pulsating flow modeling, which do not take into account the intricacies associated with oscillatory flow that occurs within regenerative cryocoolers. With the development of similar periodic flow models, further explorations can be made to better understand the pore-level physics phenomena, specifically the thermal-energy phenomena, under such conditions.

Finally, the third significant contribution was quantifying the differences between the steady flow porous media hydrodynamic resistance parameters and the corresponding oscillatory flow counterparts. The regenerator filler experimental study and the numerical pore-level study were consistent with respect to this observation.

6.3 Future Work

All of the hydrodynamic resistance simulations associated with the regenerator filler experimental study shown in this investigation assumed local thermal equilibrium between the gas and solid matrix in the regenerator. In other words, the model assumed no heat transfer resistance between the gas and the solid matrix in the regenerator. The potential thermal non-equilibrium in real regenerators should be considered in CFD models to more accurately predict the performance of component-level regenerator models and system-level cryocooler models. Little is known about the details of solid-fluid thermal non-equilibrium interactions in regenerator fillers, however, in particular for periodic flows. Experimental and computational investigations aimed at understanding the solid-fluid thermal interactions in micro-porous filler structures under periodic flow are therefore are recommended.

With respect to the aforementioned solid-fluid thermal interactions in periodic flow, direct simulation at a pore level of the regenerator fillers can be a promising and helpful technique, since direct experimental measurements are very difficult. The feasibility of this approach has been demonstrated for steady flow, pulsating flow, and for the first time periodic flow (in this investigation), and simulations at the pore level have already been conducted. However, these were only limited to incompressible flow conditions, whereas direct simulations using compressible periodic flow conditions are needed in order to understand the differences in gas compressibility behavior. Such simulations will further enhance the fundamental theory about porous media. Specifically, as a follow-up for the periodic flow pore-level work performed in this investigation, the calculation and understanding of the role of thermal dispersion is a future project that will entail intensive levels of computation time and resources. Also, different generic porous geometries should be studied, including 3-D structures. The Georgia Tech Cryo Lab will soon be able to access supercomputing resources, making it

possible for this work to be conducted. Massive computational resources are needed for this task because there will be the need for the calculation of local, instantaneous properties, including velocity and temperature, for each node in the finely discretized porous media model over a period of several oscillation periods.

The test apparatus built in this investigation was designed to be modular and relatively easy to modify or enhance. Modification of the experiment test apparatus for further validation of this investigation, and testing other relevant phenomena is strongly recommended. Some ideas in this line are as follows. Constant current anemometers can be incorporated in the test apparatus to measure the transient temperatures at both ends of the regenerator. The additions of these sensors would completely characterize the thermal fluid properties of the regenerator.

An experimental investigation essentially identical to that reported in this dissertation should be repeated at cryogenic operating temperatures. The current investigation was performed at room temperatures. Repeating these experiments at cryogenic temperatures would provide hydrodynamic parameters directly applicable to cryogenic temperatures and would show whether the current porous media theory assumptions of the hydrodynamic resistance parameters are independent of operating temperature conditions.

\

APPENDIX A

USER DEFINED FUNCTIONS

UDF for regenerator filler experimental study.

```
#include "udf.h"

#define freq 40
#define M 0.000343
#define M_phi -0.3627
#define P 247.90807
#define P_phi 0.1394

DEFINE_PROFILE(unst_m_inlet, thread, position)
{
 face_t f;
 real t = CURRENT_TIME;
  real omega  = 2*M_PI*freq;
 begin_f_loop(f, thread)
  {
  F_PROFILE(f, thread, position) = (M*sin(1*omega*t+M_phi));
  }
 end_f_loop(f,thread)
}

DEFINE_PROFILE(unst_p_outlet, thread, position)
{
 face_t f;
 real t = CURRENT_TIME;
  real omega  = 2*M_PI*freq;
 begin_f_loop(f, thread)
  {
  F_PROFILE(f, thread, position) = (P*sin(1*omega*t+P_phi));
  }
 end_f_loop(f,thread)
}
```

UDF for pore level theoretical study.

```
#include "udf.h"

DEFINE_CG_MOTION(inlet_motion, dt, vel, omega, time, dtime)
{
  real freq=40;
  real w=2.0*M_PI*freq;
  real Xcomp=0.0004;

  /* reset velocities */
  NV_S (vel, =, 0.0);
  NV_S (omega, =, 0.0);

  vel[0] = w*Xcomp*cos(w*time);
}


DEFINE_CG_MOTION(outlet_motion, dt, vel, omega, time, dtime)
{
  real freq = 40;
  real w = 2.0*M_PI*freq;
  real Xcomp=0.0004;

  /* reset velocities */
  NV_S (vel, =, 0.0);
  NV_S (omega, =, 0.0);

  vel[0] = w*Xcomp*cos(w*time);
}
```

APPENDIX B

MATLAB CODE

Code for data analysis written in Matlab

```
% Inputs
type = input('HighAmp or LowAmp?\n', 's');
freq = input('Freqency:\n');
freqs = num2str(freq);
freqs = strcat(freqs, 'Hz\');

timestep= 1.5e-5;
Period = 1/freq;
dataPeriod = Period ./ timestep;
threeC = 400000 - dataPeriod .* 3;

folder = '';
name= {'p_3.out', 'p_4.out', 'p_5.out', 'v_3.out', 'v_4.out', 'v_5.out'};

% Capturing Raw Data

filename = strcat(folder,type,'\',freqs,name{1});
filename = char(filename);
p3 = textread(filename, '', 'headerlines',2);

filename = strcat(folder,type,'\',freqs,name{2});
filename = char(filename);
p4 = textread(filename, '', 'headerlines',2);

filename = strcat(folder,type,'\',freqs,name{3});
filename = char(filename);
p5 = textread(filename, '', 'headerlines',2);

filename = strcat(folder,type,'\',freqs,name{4});
filename = char(filename);
v3 = textread(filename, '', 'headerlines',2);

filename = strcat(folder,type,'\',freqs,name{5});
filename = char(filename);
v4 = textread(filename, '', 'headerlines',2);

filename = strcat(folder,type,'\',freqs,name{6});
filename = char(filename);
v5 = textread(filename, '', 'headerlines',2);

% Extracting Three Cycles
p3n = p3(threeC+1:end,2);
```

```
p4n = p4(threeC+1:end,2);
p5n = p5(threeC+1:end,2);
v3n = v3(threeC+1:end,2);
v4n = v4(threeC+1:end,2);
v5n = v5(threeC+1:end,2);
time = p4(threeC+1:end,1);

% Constants
rho = 5.0045;
mu = 1.4615e-5;
cond = .1154;
E = .75;
dx = 100e-6;
dt = timestep;

% Calc v4_dt term
v4t = v4(threeC:end,2);
v4dt=v4n;
[s ~] = size(v4t);
for ind = 2:s
    v4dt(ind-1)=v4t(ind) - v4t(ind-1);
end

% K Algorithm Method 1
term1 = rho.*(( v4dt./dt ) + ( v4n .*(v5n -v3n)./(2.*dx) ));
term2 = mu.* ( v5n - 2 .* v4n + v3n)./ dx.^2 ;
term3 = (p5n-p3n)./(2.*dx);
term4 = E*mu*v4n ;

k = -term4./(term1 + term3 - term2);

h=figure;
plot(time, k)
xlabel('Time(s)')
ylabel('Instantaneous Volume-Average Darcy Term (m^2)')
ttl = strcat('C:\Users\gth714q\Desktop\plots\', 'darcy_t');
ttl = char(ttl);
saveas(h, ttl)

% K Algorithm Method 2

Bconst = 0;

startval = input('Start test value: \n');
endval = input ('Last value: \n');
numPoints = input ('Number of data points: \n');
testvec = linspace(startval, endval, numPoints);

p53 = p5n - p3n;
error = zeros(numPoints,2);

for ndx= 1:numPoints
ndx
```

```
Kconst = testvec(ndx);

term1 = rho.*(( v4dt./dt ) + ( v4n .*(v5n -v3n)./(2.*dx) ));
term2 = mu.* ( v5n - 2 .* v4n + v3n)./ dx.^2 ;
term3 = E.*mu.*v4n./Kconst;
term4 = E.^2 .* rho .* Bconst .* abs(v4n) .* v4n;
term5 = 2 .* dx;

delp_exp = (term1 - term2 + term3 + term4).* - term5;
diff = p53 - delp_exp;

diff = abs(diff);
avgdiff = mean(diff);
error(ndx,2) = avgdiff;
error(ndx,1) = Kconst;
end

[mindiff, indc]=min(error(:,2));
actualKval=error(indc,1);
actualKval

term1 = rho.*(( v4dt./dt ) + ( v4n .*(v5n -v3n)./(2.*dx) ));
term2 = mu.* ( v5n - 2 .* v4n + v3n)./ dx.^2 ;
term3 = E.*mu.*v4n./actualKval;
term4 = E.^2 .* rho .* Bconst .* abs(v4n) .* v4n;
term5 = 2 .* dx;

delp_exp = (term1 - term2 + term3 + term4).* - term5;
plot(time,delp_exp,'-m');
hold on
plot(time,p53, 'g');
hold off

% B Algorithm

Kconst= 0.000000000098436;


startval = input('Start test value: \n');
endval = input ('Last value: \n');
numPoints = input ('Number of data points: \n');
testvec = linspace(startval, endval, numPoints);

p53 = p5n - p3n;
error = zeros(numPoints,2);

for ndx= 1:numPoints
ndx
Bconst = testvec(ndx);

term1 = rho.*(( v4dt./dt ) + ( v4n .*(v5n -v3n)./(2.*dx) ));
term2 = mu.* ( v5n - 2 .* v4n + v3n)./ dx.^2 ;
term3 = E.*mu.*v4n./Kconst;
```

```
term4 = E.^2 .* rho .* Bconst .* abs(v4n) .* v4n;
term5 = 2 .* dx;

delp_exp = (term1 - term2 + term3 + term4).* - term5;
diff = p53 - delp_exp;

diff = abs(diff);
avgdiff = mean(diff);
error(ndx,2) = avgdiff;
error(ndx,1) = Bconst;
end

[mindiff, indc]=min(error(:,2));
actualBval=error(indc,1);
actualBval

term1 = rho.*(( v4dt./dt ) + ( v4n .*(v5n -v3n)./(2.*dx) ));
term2 = mu.* ( v5n - 2 .* v4n + v3n)./ dx.^2 ;
term3 = E.*mu.*v4n./Kconst;
term4 = E.^2 .* rho .* actualBval .* abs(v4n) .* v4n;
term5 = 2 .* dx;

delp_exp = (term1 - term2 + term3 + term4).* - term5;
plot(time,delp_exp,'-m');
hold on
plot(time,p53, 'g');
hold off

% B * sqrt(k)
Kconst = 0.000000000098436;

term1 = rho.*(( v4dt./dt ) + ( v4n .*(v5n -v3n)./(2.*dx) ));
term2 = mu.* ( v5n - 2 .* v4n + v3n)./ dx.^2 ;
term3 = (p5n-p3n)./(2.*dx);
term5 = E.*mu.*v4n./Kconst;
term4 = E^2.*rho.*abs(v4n).*v4n;

B = (term1 + term3 - term2 + term5)./ term4;

C = B .* sqrt(Kconst);

h=figure;
plot(time, C)
xlabel('Time(s)')
ylabel('Instantaneous Volume-Average Forchheimer Term')
ttl = strcat('C:\Users\gth714q\Desktop\plots\', 'Forchheimer_t');
ttl = char(ttl);
saveas(h, ttl)
```

```
function nu = nuDX(amp, freqq)

% primary
folder = '';

type = {'HighAmp', 'LowAmp'};

if strcmp(amp, 'High')
    ndx = 1;
elseif strcmp(amp, 'Low')
    ndx = 2;
end

freq= [20, 40, 60];
freqs= {'20hz\', '40hz\', '60hz\'};

if freqq == 20
    ind = 1;
elseif freqq == 40
    ind = 2;
elseif freqq == 60
    ind = 3;
end

name= {'q_4.out', 't_4.out', 't_4_surf.out'};

L= 100e-6;
A= .0001;
dt= 220;
K_f= .1154;
K = 0.000000000098436;

% Function method

timestep= 1.5e-5;
Period = 1/freq(ind);
dataPeriod = Period ./ timestep;
threeC = 400000 - dataPeriod .* 3;

filename = strcat(folder,type{ndx},'\',freqs{ind},name{1});
filename = char(filename);
q4= textread(filename, '', 'headerlines',2);

q4 = q4(threeC:end, :);

q4(:,3)=(q4(:,2) .* L)./(A .* dt .* K_f);

nu(:,1) = q4(:,1);
nu(:,2) = q4(:,3);

plot(nu(:,1), nu(:,2), 'm');
xlabel('Time(s)')
```

```
ylabel('Instantaneous Nusselt Number, Nu_L')
end
```

```
function nu = nuK(amp, freqq)

% primary
folder = '';


type = {'HighAmp', 'LowAmp'};

if strcmp(amp, 'High')
    ndx = 1;
elseif strcmp(amp, 'Low')
    ndx = 2;
end

freq= [20, 40, 60];
freqs= {'20hz\', '40hz\', '60hz\'};

if freqq == 20
    ind = 1;
elseif freqq == 40
    ind = 2;
elseif freqq == 60
    ind = 3;
end

name= {'q_4.out', 't_4.out', 't_4_surf.out'};

L= 100e-6;
A= .0001;
dt= 220;
K_f= .1154;
K = 0.000000000098436;

% Function method

timestep= 1.5e-5;
Period = 1/freq(ind);
dataPeriod = Period ./ timestep;
threeC = 400000 - dataPeriod .* 3;

filename = strcat(folder,type{ndx},'\',freqs{ind},name{1});
filename = char(filename);
q4= textread(filename, '', 'headerlines',2);

q4(:,3)=(q4(:,2) .* sqrt(K))./(A .* dt .* K_f);

nu(:,1) = q4(:,1);
```

```
nu(:,2) = q4(:,3);


end
```

```
% Plot Generating defaults

clc
clear

file1 = input('file one\n', 's');
file2 = input('file two\n', 's');

folder = '';

timestep= 1.5e-5;

Period = 1/20;
dataPeriod = Period ./ timestep;
oneC20 = 400000 - dataPeriod;

Period = 1/40;
dataPeriod = Period ./ timestep;
oneC40 = 400000 - dataPeriod;

Period = 1/60;
dataPeriod = Period ./ timestep;
oneC60 = 400000 - dataPeriod;


% data capture file 1
if strcmp(file1, 'NuL')

f1h20 = nuDX('High', 20);
x = size(f1h20);
Period = 1/20;
dataPeriod = Period ./ timestep;
onep20 = x(1) - dataPeriod;
f1h20 = f1h20(onep20:end, :);

f1h40 = nuDX('High', 40);
y = size(f1h40);
Period = 1/40;
dataPeriod = Period ./ timestep;
onep40 = y(1) - dataPeriod;
f1h40 = f1h40(onep40:end, :);

f1h60 = nuDX('High', 60);
z = size(f1h60);
Period = 1/60;
```

```
dataPeriod = Period ./ timestep;
onep60 = z(1) - dataPeriod;
f1h60 = f1h60(onep60:end, :);

f1l20 = nuDX('Low', 20);
f1l20 = f1l20(onep20:end, :);

f1l40 = nuDX('Low', 40);
f1l40 = f1l40(onep40:end, :);

f1l60 = nuDX('Low', 60);
f1l60 = f1l60(onep60:end, :);

elseif strcmp(file1, 'NuK')

f1h20 = nuK('High', 20);
x = size(f1h20);
Period = 1/20;
dataPeriod = Period ./ timestep;
onep20 = x(1) - dataPeriod;
f1h20 = f1h20(onep20:end, :);

f1h40 = nuK('High', 40);
y = size(f1h40);
Period = 1/40;
dataPeriod = Period ./ timestep;
onep40 = y(1) - dataPeriod;
f1h40 = f1h40(onep40:end, :);

f1h60 = nuK('High', 60);
z = size(f1h60);
Period = 1/60;
dataPeriod = Period ./ timestep;
onep60 = z(1) - dataPeriod;
f1h60 = f1h60(onep60:end, :);

f1l20 = nuK('Low', 20);
f1l20 = f1l20(onep20:end, :);

f1l40 = nuK('Low', 40);
f1l40 = f1l40(onep40:end, :);

f1l60 = nuK('Low', 60);
f1l60 = f1l60(onep60:end, :);

else
%high
filename = strcat(folder, 'RawData\', 'HighAmp','\','20hz\',file1);
filename = char(filename);
f1h20 = textread(filename, '', 'headerlines',2);

filename = strcat(folder,'RawData\','HighAmp','\','40hz\',file1);
filename = char(filename);
```

```
f1h40 = textread(filename, '', 'headerlines',2);

filename = strcat(folder,'RawData\','HighAmp','\','60hz\',file1);
filename = char(filename);
f1h60 = textread(filename, '', 'headerlines',2);

%low
filename = strcat(folder,'RawData\','LowAmp','\','20hz\',file1);
filename = char(filename);
f1l20 = textread(filename, '', 'headerlines',2);

filename = strcat(folder,'RawData\','LowAmp','\','40hz\',file1);
filename = char(filename);
f1l40 = textread(filename, '', 'headerlines',2);

filename = strcat(folder,'RawData\','LowAmp','\','60hz\',file1);
filename = char(filename);
f1l60 = textread(filename, '', 'headerlines',2);
end

% data capture file 2
%high
filename = strcat(folder,'RawData\','HighAmp','\','20hz\',file2);
filename = char(filename);
f2h20 = textread(filename, '', 'headerlines',2);

filename = strcat(folder,'RawData\','HighAmp','\','40hz\',file2);
filename = char(filename);
f2h40 = textread(filename, '', 'headerlines',2);

filename = strcat(folder,'RawData\','HighAmp','\','60hz\',file2);
filename = char(filename);
f2h60 = textread(filename, '', 'headerlines',2);

%low
filename = strcat(folder,'RawData\','LowAmp','\','20hz\',file2);
filename = char(filename);
f2l20 = textread(filename, '', 'headerlines',2);

filename = strcat(folder,'RawData\','LowAmp','\','40hz\',file2);
filename = char(filename);
f2l40 = textread(filename, '', 'headerlines',2);

filename = strcat(folder,'RawData\','LowAmp','\','60hz\',file2);
filename = char(filename);
f2l60 = textread(filename, '', 'headerlines',2);

% one cycle
if strcmp(file1, 'NuL')
f2h20 = f2h20(oneC20:end, :);
f2h40 = f2h40(oneC40:end, :);
f2h60 = f2h60(oneC60:end, :);
```

```
f2l2O = f2l2O(oneC2O:end, :);
f2l4O = f2l4O(oneC4O:end, :);
f2l6O = f2l6O(oneC6O:end, :);

elseif strcmp(file1, 'NuK')

f2h2O = f2h2O(oneC2O:end, :);
f2h4O = f2h4O(oneC4O:end, :);
f2h6O = f2h6O(oneC6O:end, :);

f2l2O = f2l2O(oneC2O:end, :);
f2l4O = f2l4O(oneC4O:end, :);
f2l6O = f2l6O(oneC6O:end, :);

else
f1h2O = f1h2O(oneC2O:end, :);
f1h4O = f1h4O(oneC4O:end, :);
f1h6O = f1h6O(oneC6O:end, :);

f1l2O = f1l2O(oneC2O:end, :);
f1l4O = f1l4O(oneC4O:end, :);
f1l6O = f1l6O(oneC6O:end, :);

f2h2O = f2h2O(oneC2O:end, :);
f2h4O = f2h4O(oneC4O:end, :);
f2h6O = f2h6O(oneC6O:end, :);

f2l2O = f2l2O(oneC2O:end, :);
f2l4O = f2l4O(oneC4O:end, :);
f2l6O = f2l6O(oneC6O:end, :);
end

% max

[f1h2Om f1h2Oi] = max(f1h2O(:,2));
[f1h4Om f1h4Oi] = max(f1h4O(:,2));
[f1h6Om f1h6Oi] = max(f1h6O(:,2));

[f1l2Om f1l2Oi] = max(f1h2O(:,2));
[f1l4Om f1l4Oi] = max(f1l4O(:,2));
[f1l6Om f1l6Oi] = max(f1l6O(:,2));

[f2h2Om f2h2Oi] = max(f2h2O(:,2));
[f2h4Om f2h4Oi] = max(f2h4O(:,2));
[f2h6Om f2h6Oi] = max(f2h6O(:,2));

[f2l2Om f2l2Oi] = max(f2l2O(:,2));
[f2l4Om f2l4Oi] = max(f2l4O(:,2));
[f2l6Om f2l6Oi] = max(f2l6O(:,2));

% ylabels

if strcmp(file1, 'v_4.out')
```

```
    lab1= 'Instantaneous Volume-Average Velocity,v(m/s)';
    titl1 = ' v ';
elseif strcmp(file1, 'p_4.out')
    lab1= 'Instantaneous Volume-Average Pressure,P(Pa)';
    titl1 = ' P ';
elseif strcmp(file1, 't_4.out')
    lab1= 'Instantaneous Volume-Average Temperature,T(K)';
    titl1 = ' T ';
elseif strcmp(file1, 'q_4.out')
    lab1= 'Instantaneous Average-Surface Heat Transfer,Q(W)';
    titl1 = ' Q ';
elseif strcmp(file1, 'NuL')
    lab1= 'Instantaneous Volume-Average Cell Length-Based Nusselt Number';
elseif strcmp(file1, 'NuK')
    lab1= 'Instantaneous Volume-Average Darcy-Based Nusselt Number';
end

if strcmp(file2, 'v_4.out')
    lab2= 'Instantaneous Volume-Average Velocity,v(m/s)';
    titl2 = ' v ';
elseif strcmp(file2, 'p_4.out')
    lab2= 'Instantaneous Volume-Average Pressur,P(Pa)';
    titl2 = ' P ';
elseif strcmp(file2, 't_4.out')
    lab2= 'Instantaneous Volume-Average Temperature,T(K)';
    titl2 = ' T';
elseif strcmp(file2, 'q_4.out')
    lab2= 'Instantaneous Average-Surface Heat Transfer,Q(W)';
    titl2 = ' Q ';
elseif strcmp(file2, 'NuL')
    lab2= 'Instantaneous Volume-Average Cell Length-Based Nusselt Number';
elseif strcmp(file2, 'NuK')
    lab2= 'Instantaneous Volume-Average Darcy-Based Nusselt Number';
end

% calculating phase difference
val = zeros(6,1);

h=figure;
[haxes,hline1,hline2] = plotyy(f1h2O(:,1),f1h2O(:,2),f2h2O(:,1),f2h2O(:,2));
h2O = f1h2O(f1h2Oi,1) - f2h2O(f2h2Oi,1);
val(1) = h2O .* 360 ./ 2O;
Theta = num2str(val(1));
ttl = strcat('Case 4 ', ' ', titl1, ' vs.', titl2);
% ttl = char(ttl);
title(ttl);
xlabel('Time(s)')
axes(haxes(1))
ylabel(lab1)
axes(haxes(2))
ylabel(lab2)
ttl2 = strcat(folder, '\Results\Plots\newPhase\', titl1, '_', titl2,'_Case4');
ttl2 = char(ttl2);
```

```
saveas(h, ttl2)


h=figure;
[haxes,hline1,hline2] = plotyy(f1h4O(:,1),f1h4O(:,2),f2h4O(:,1),f2h4O(:,2));
h4O = f1h4O(f1h4Oi,1) - f2h4O(f2h4Oi,1);
val(2) = h4O .* 36O .* 4O;
Theta = num2str(val(2));
ttl = strcat('Case 5 ', ' ', titl1, ' vs.', titl2);
% ttl = char(ttl);
title(ttl);
xlabel('Time(s)')
axes(haxes(1))
ylabel(lab1)
axes(haxes(2))
ylabel(lab2)
ttl2 = strcat(folder, '\Results\Plots\newPhase\', titl1, '_', titl2,'_Case5');
ttl2 = char(ttl2);
saveas(h, ttl2)

h=figure;
[haxes,hline1,hline2] = plotyy(f1h6O(:,1),f1h6O(:,2),f2h6O(:,1),f2h6O(:,2));
h6O = f1h6O(f1h6Oi,1) - f2h6O(f2h6Oi,1);
val(3) = h6O .* 36O .* 6O;
Theta = num2str(val(3));
ttl = strcat('Case 6 ', ' ', titl1, ' vs.', titl2);
% ttl = char(ttl);
title(ttl);
xlabel('Time(s)')
axes(haxes(1))
ylabel(lab1)
axes(haxes(2))
ylabel(lab2)
ttl2 = strcat(folder, '\Results\Plots\newPhase\', titl1, '_', titl2,'_Case6');
ttl2 = char(ttl2);
saveas(h, ttl2)

h=figure;
[haxes,hline1,hline2] = plotyy(f1l2O(:,1),f1l2O(:,2),f2l2O(:,1),f2l2O(:,2));
l2O = f1l2O(f1l2Oi,1) - f2l2O(f2l2Oi,1);
val(4) = l2O .* 36O .* 2O;
Theta = num2str(val(4));
ttl = strcat('Case 1 ', ' ', titl1, ' vs.', titl2);
% ttl = char(ttl);
title(ttl);
xlabel('Time(s)')
axes(haxes(1))
ylabel(lab1)
axes(haxes(2))
ylabel(lab2)
ttl2 = strcat(folder, '\Results\Plots\newPhase\', titl1, '_', titl2,'_Case1');
ttl2 = char(ttl2);
saveas(h, ttl2)
```

```
h=figure;
[haxes,hline1,hline2] = plotyy(f1l4O(:,1),f1l4O(:,2),f2l4O(:,1),f2l4O(:,2));
l4O = f1l4O(f1l4Oi,1) - f2l4O(f2l4Oi,1);
val(5) = l4O .* 36O .* 4O;
Theta = num2str(val(5));
ttl = strcat('Case 2 ', ' ', titl1, ' vs.', titl2);
% ttl = char(ttl);
title(ttl);
xlabel('Time(s)')
axes(haxes(1))
ylabel(lab1)
axes(haxes(2))
ylabel(lab2)
ttl2 = strcat(folder, '\Results\Plots\newPhase\', titl1, '_', titl2,'_Case2');
ttl2 = char(ttl2);
saveas(h, ttl2)

h=figure;
[haxes,hline1,hline2] = plotyy(f1l6O(:,1),f1l6O(:,2),f2l6O(:,1),f2l6O(:,2));
l6O = f1h6O(f1l6Oi,1) - f2h6O(f2l6Oi,1);
val(6) = l6O .* 36O .* 6O;
Theta = num2str(val(6));
ttl = strcat('Case 3 ', ' ', titl1, ' vs.', titl2);
% ttl = char(ttl);
title(ttl);
xlabel('Time(s)')
axes(haxes(1))
ylabel(lab1)
axes(haxes(2))
ylabel(lab2)
ttl2 = strcat(folder, '\Results\Plots\newPhase\', titl1, '_', titl2,'_Case3');
ttl2 = char(ttl2);
saveas(h, ttl2)
```

Periodic Flow

```
fl= ?;
ttl= '?';


names = {'\inlet_p.out','\outlet_p.out', '\mass_flow.out'};
filename = strcat(folder, '\FM Cal Extended_1O');
Exceldata = xlsread(filename,'sheet4');

EXdata = Exceldata(fl-1,:);
folder1 = strcat(folder, '\P_charge_1723700\');
pathname = uigetdir(folder1);

filename=strcat(pathname, names{1});
PinSim = textread(filename, '', 'headerlines',2);
```

```
filename=strcat(pathname, names{2});
PoutSim = textread(filename, '', 'headerlines',2);

filename=strcat(pathname, names{3});
massSim = textread(filename, '', 'headerlines',2);

t = PinSim(:,1);
PinEX = EXdata(4).* sin(2.*pi.*EXdata(2)*t + EXdata(5));
PoutEX = EXdata(6).* sin(2.*pi.*EXdata(2)*t + EXdata(7));
massEX = EXdata(8).* sin(2.*pi.*EXdata(2)*t + EXdata(10));

X1 = PinSim(2000:8000,1);

YMatrix1(:,1)=PinSim(2000:8000,2);
YMatrix1(:,2)=PinEX(2000:8000,1);
YMatrix1(:,3)=PoutEX(2000:8000,1);

Y1(:,1)=massEX(2000:8000,1);

% X1=[t t t];
% % Y1=[PinSim(2000:8000,2) PoutSim(2000:8000,2) PinEX(2000:8000,1) PoutEX(2000:8000,1)];
%
% X2=[t];
% % Y2=[massSim(2000:8000,2) massEX(2000:8000,1)];


% Create figure
figure1 = figure('Color',...
    [0.800000011920929 0.800000011920929 0.800000011920929]);
colormap('winter');

% Create axes
%,'YTick',[-20000 -10000 0 10000 20000]
axes1 = axes('Parent',figure1);
box(axes1,'on');
hold(axes1,'all');

% Create multiple lines using matrix input to plot
plot1 = plot(X1,YMatrix1,'Parent',axes1,'LineWidth',2);
set(plot1(1),'LineWidth',3,...
    'Color',[0.800000011920929 0.800000011920929 0.800000011920929]);
set(plot1(2),'LineStyle','--','Color',[0 0 0]);
set(plot1(3),'LineStyle',':',...
    'Color',[0.313725501298904 0.313725501298904 0.313725501298904]);

% Create xlabel
xlabel('Time, t (s)','Interpreter','latex','FontSize',20);

% Create ylabel
ylabel('Pressure, P (Pa)','Interpreter','latex','FontSize',20);

% Create axes
```

```
%'YTick',[-0.0004 -0.0002 0 0.0002 0.0004],
%'ColorOrder',[0 0.75 0.75;0.75 0 0.75;0.75 0.75 0;0.25 0.25 0.25;0 0 1;0 0.5 0;1 0
0],...
axes2 = axes('Parent',figure1,...
    'YAxisLocation','right',...
    'YColor',[0 0 1],...
    'Color','none');

hold(axes2,'all');

% Create plot
plot(X1,Y1,'Parent',axes2,'LineWidth',2,'LineStyle','-.','Color',[0 0 1]);

% Create ylabel
ylabel('Mass Flow Rate, $\dot{m}$ (kg/s)','VerticalAlignment','cap',...
    'Interpreter','latex',...
    'Rotation',90,...
    'FontSize',20,...
    'Color',[0 0 1]);

title(ttl,'FontWeight','bold','FontSize',30);

if file == 1
    t = data(:,1);
    P = EXdata(4).* sin(2.*pi.*EXdata(2)*t + EXdata(5));
    plot(t, data(:,2),'m')
    hold on
    plot(t, P,'b')
    hold off

elseif file == 2
    t = data(:,1);
    P = EXdata(6).* sin(2.*pi.*EXdata(2)*t + EXdata(7));
    plot(t, data(:,2),'m')
    hold on
    plot(t, P,'b')
    hold off

elseif file == 3
    t = data(:,1);
    P = EXdata(8).* sin(2.*pi.*EXdata(2)*t + EXdata(10));
    plot(t, data(:,2),'m')
    hold on
    plot(t, P,'b')
    hold off
end
```

```
function Code2

z= 1;
```

```
fl=49;

filename = strcat(folder, '\FM Cal Extended_10');
Exceldata = xlsread(filename,'sheet4');

EXdata = Exceldata(fl-1,:);

folder1 = strcat(folder, '\Non Ideal Gas\');


pathname = uigetdir(folder1);
filename=strcat(pathname, '\inlet_p.out');
data = textread(filename, '', 'headerlines',2);

timestep= 1.5e-5;
freq = EXdata(2);
Period = 1/freq;
dataPeriod = Period ./ timestep;
[totSteps, ~]= size(data);
OneC = totSteps-dataPeriod;

t = data(:,1);
C = data(:,2);
EX = EXdata(4).* sin(2.*pi.*EXdata(2)*t + EXdata(5));

maxC = max(C(OneC:totSteps));
minC = min(C(OneC:totSteps));
hC = maxC-minC;

maxEX = max(EX(OneC:totSteps));
minEX = min(EX(OneC:totSteps));
hEX = maxEX - minEX;

Diff = hEX - hC;

if z == 1
    plot(t, C,'m')
    hold on
    plot(t, EX,'b')
    title(pathname(end-5:end))
    legend('Computational', 'Experimental')
    hold off
elseif z == 2
    Periods = totSteps./dataPeriod;
    errArr = zeros(Periods-1,1);
    for ind= 1:Periods-1
        diffEX = (max(EX(ind*dataPeriod:(ind+1)*dataPeriod))-
min(EX(ind*dataPeriod:(ind+1)*dataPeriod)));
        diffC = (max(C(ind*dataPeriod:(ind+1)*dataPeriod)))-
min(C(ind*dataPeriod:(ind+1)*dataPeriod));
        errArr(ind) = diffEX - diffC;
    end
    plot(errArr)
```

```
end

end
```

```
file = ?;
fl=?;


names = {'\inlet_p.out','\outlet_p.out', '\mass_flow.out'};
filename = strcat(folder, '\FM Cal Extended_10');
Exceldata = xlsread(filename,'sheet4');

EXdata = Exceldata(fl-1,:);
pathname = uigetdir(folder1);
filename=strcat(pathname, names{file});
data = textread(filename, '', 'headerlines',2);




if file == 1
    t = data(:,1);
    P = EXdata(4).* sin(2.*pi.*EXdata(2)*t + EXdata(5));
    plot(t, data(:,2),'m')
    hold on
    plot(t, P,'b')
    hold off

elseif file == 2
    t = data(:,1);
    P = EXdata(6).* sin(2.*pi.*EXdata(2)*t + EXdata(7));
    plot(t, data(:,2),'m')
    hold on
    plot(t, P,'b')
    hold off

elseif file == 3
    t = data(:,1);
    P = EXdata(8).* sin(2.*pi.*EXdata(2)*t + EXdata(10));
    plot(t, data(:,2),'m')
    hold on
    plot(t, P,'b')
    hold off
end
```

APPENDIX C

CONDITIONS FOR COMPUTATIONAL STUDY

Initial and boundary conditions.

"Inlet/Exit" Conditions

Helium as working fluid

Periodic Flow $U = \omega a \cos(\omega t)$

Temperature 80 K & 300 K

Initial Condition

Solution to Steady Flow

Boundary Conditions

- Symmetry at Top and Bottom Surfaces
- No Slip Condition at Walls
- Conjugate Heat Transfer

Numerical Method

- 2D Meshes made in GAMBIT
- Finite-Volume Method
- Laminar flow

REFERENCES

[1] G. W. Swift, *Thermoacoustics*, Acoustical Society of America, 200

[2] R. Radebaugh, "Development of the Pulse Tube Refrigerator as an Efficient and Reliable Cryocooler," *Proc. Institute of Refrigeration,* 1999.

[3] G. Walker, and E.R. Bingham, *Low-Capacity Cryogenic Refrigeration*, Oxford University Press, 1994.

[4] E. C. Landrum, "Anisotropic parameters of mesh fillers relevant to miniature cryocoolers," *Master's Thesis*, Georgia Institute of Technology, Atlanta, Georgia, 2009.

[5] R. Radebaugh, and W. Gully, "Foundations of Cryocoolers Short Course," *Presented at 15th International Cryocooler Conference*, 2008.

[6] M.G. Pathak, "Thermal dispersion and convective heat transfer during laminar pulsating flow in porous media," *Master's Thesis*, Georgia Institute of Technology, Atlanta, Georgia, 2010.

[7] A. J. Organ, *Thermodynamics & Gas Dynamics of the Stirling Cycle Machine,* Cambridge University Press, 1992, pp. 1-92.

[8] R. Radebaugh, 2011, Personal communication.

[9] J. Olson, et al., "Development of a Space-Type 4-Stage Pulse Tube Cryocooler for Very Low Temperature," *Adv. in Cryogenic Eng*., vol. 51, 2006, pp. 623-631.

[10] R. Radebaugh, "Pulse Tube Cryocoolers for Cooling Infrared Sensors," *Proceedings of SPIE,* vol. 4130, 2000, pp. 363-379.

[11] J.S. Cha, "Hydrodynamic parameters of micro-porous media for steady and oscillatory flow: application to cryocooler regenerators," *Ph.D. Dissertation*, Georgia Institute of Technology, Atlanta, Georgia, 2007.

[12] W.E. Gifford, and R.C. Longsworth, "Pulse-Tube Refrigeration," *ASME*, 1997.

[13] G. Popescu, V. Radcenco, E. Gargalian, and P. Ramay Bala, “A Critical Review of Pulse Tube Cryogenerator Research,” *International Journal of Refrigeration*, vol. 24, 2001, pp. 230-237.

[14] J.P. Harvey, “Parametric study of cryocooler regenerator performance,” Master’s Thesis, Georgia Institute of Technology, Atlanta, Georgia, 1999.

[15] T. Conrad, “Miniaturized Pulse Tube Refrigerators,” *Ph.D. Dissertation*, Georgia Institute of Technology, Atlanta, Georgia, 2011.

[16] E.I. Mikulin, A.A. Tarasov, and M.P. Shkrebyonock, “Low-temperature expansion pulse tubes,” *Adv. Cryo. Eng.*, vol. 31, 1984.

[17] S. Zhu, P. Wu, and Z. Chen, "Double inlet pulse tube refrigerators: an important improvement," *Cryogenics*, vol. 30, 1990, pp. 514-520.

[18] S. Zhu, S. Zhou, N. Yoshimura, and Y. Matsubara, "Phase shift effect of the long neck tube for the pulse tube refrigerator," *Cryocoolers*, vol. 9, 1997, pp. 269-278.

[19] D.L. Gardner, and G.W. Swift, "Use of inertance in orifice pulse tube refrigerators," *Cryogenics*, vol. 37, 1997, pp. 117-121.

[20] P. R. Roach, and A. Kashani, “Pulse tube cryocoolers with an inertance tube: Theory, Modeling and Practice,” *Advances in Cryogenics Engineering*, vol. 43, 1998, pp. 1895-1902.

[21] I. Garaway, and G. Grossman, “A Study of a High Frequency Miniature Reservoir-Less Pulse Tube,” *AIP Conference Proceedings*, vol. 985, 2008, pp. 1547-1554.

[22] R. Radebaugh, "Cryocoolers: the state of the art and recent developments," *Journal of Physics: Condensed Matter*, vol. 21, 2009.

[23] F. Kuwahara, A. Nakayama, and H. Koyama, “A numerical study of thermal dispersion in porous media,” *ASME J. Heat Transfer*, vol. 118, 1996, pp. 756– 761.

[24] F. Kuwahara, M. Shirota, and A. Nakayama, "A numerical study of interfacial convective heat transfer coefficient in two-energy equation model for convection in porous media*," Int. J. Heat Mass Transfer,* vol. 44, 2001, pp. 1153–1159.

[25] F. Kuwahara, T. Yamane, and A. Nakayama, "Large eddy simulation of turbulent flow in porous media," *Int. Communications in Heat and Mass Transfer,* vol. 33, 2006, pp. 411–418.

[26] A. Nakayama, F. Kuwahara, T. Umemoto, and T. Hayashi, "Heat and fluid flow within an anisotropic porous medium," *ASME J. Heat Transfer,* vol. 124, 2002, pp. 746–753.

[27] A. Nakayama, F. Kuwahara, M. Sugiyama, and G. Xu, "A two-energy equation model for conduction and convection in porous media," *International Journal of Heat and Mass Transfer,* vol. 44, 2001, pp. 4375-4379.

[28] A. Nakayama, F. Kuwahara, and Y. Sano, "Concept of equivalent diameter for heat and fluid flow in porous media," *AIChE J.,* vol. 53, 2007, pp. 732–736.

[29] A. Nakayama, F. Kuwahara, and T. Hayashi, "Numerical modelling for three-dimensional heat and fluid flow through a bank of cylinders in yaw," *Journal of Fluid Mechanics,* vol. 498, 2004, pp. 139-159.

[30] A. Nakayama, F. Kuwahara, and Y. Kodama, "An equation for thermal dispersion flux transport and its mathematical modeling for heat transfer and fluid flow in a porous medium," *J. Fluid Mech.,* vol. 563, 2006, pp. 81–96.

[31] S.M. Kim, and S. M. Ghiaasiaan, "Numerical modeling of laminar pulsating flow in porous media," *Journal of Fluids Engineering* , vol. 131, 2009.

[32] M.G. Pathak, and S. M. Ghiaasiaan, "Convective heat transfer and thermal dispersion during laminar pulsating flow in porous media," *Intl. J. of Thermal Sci.,* vol. 50, 2010, pp. 440-448.

[33] T.I. Mulcahey, M.G. Pathak, and S.M. Ghiaasiaan, "The effect of flow pulsation on drag and heat transfer in an array of heated square cylinders," *International Journal of Thermal Sciences,* vol. 64, 2012, pp.105-120.

[34] M. Kaviany, *Principals of heat transfer in porous media*, 2nd ed., Springer-Veriag, 2006.

[35] S. Whitaker, "The method of volume averaging," Kluwer Academic, 1999.

[36] W. G. Grant, and K. O'Neil, "On the general equations for flow in porous media and their reduction to Darcy's law," *Water Resources Research*, vol. 12, 1976, pp. 148-154.

[37] M. Quintard, M. Kaviany, and S.Whitaker, "Two-medium treatment of heat transfer in porous media: numerical results for effective properties," *Adv. Water Res.*, vol. 20, 1997, pp. 77–94.

[38] C. Moyne, S. Didierjean, H.P. Amaral Souto, and O.T. da Silveira, "Thermal dispersion in porous media: one equation model," *Int. J. Heat Mass Transfer*, vol. 43, 2000, pp. 3853–3867.

[39] K. Vafai and C. Tien, "Boundary and inertia effects on flow and heat transfer in porous media," *International Journal of Heat and Mass Transfer*, vol. 24, 1981, pp. 195-203.

[40] K.Vafai, and A. Amiri, "Non-Darcian effects in confined forced convective flows, in: D. B. Ingham, I. Pope (Eds.)," *Transport Phenomena Porous Media*, Pergamon, New York, 1998.

[41] C.T. Hsu, H.L. Fu, and P. Cheng, "On pressure velocity correlation of steady and oscillating flows in regenerators made of wire-screens," *ASME J. Fluids Eng.*, vol. 121, 1999, pp. 52–56.

[42] J. P. Harvey, "Oscillatory Compressible Flow and Heat Transfer in Porous Media – Application to Cryocooler Regenerators," *Ph.D. Dissertation*, Georgia Institute of Technology, Atlanta, Georgia, 2003.

[43] J. Bear, *Dynamics of Fluids in Porous Media*, Dover Publications, 1972.

[44] S. Kim, "Numerical investigation on laminar pulsating flow through porous media," *Master's Thesis*, Georgia Institute of Technology, Atlanta, Georgia, 2008.

[45] C.T. Hsu, and P. Cheng, “Thermal dispersion in a porous medium,” *Int. J. Heat Mass Transfer*, vol. 32, 1990, pp.1587-1597.

[46] S. Liu, A. Afacan, and J. Masliyah, “Steady incompressible laminar flow in porous media,” *Chemical Engineering Science*, vol. 49, 1994, pp. 3565-3586.

[47] O. Coulaud, P. Morel, and J. P. Caltagirone, “Numerical modelling of nonlinear effects in laminar f1low through a porous medium,” *J. Fluid Mech*., vol. 190, 1988, pp. 393-407.

[48] M. Pedras, and M. de Lemos, "Simulation of turbulent flow in porous media using a spatially periodic array and a low Re two-equation closure," *Numerical Heat Transfer, Part A: Applications,* vol. 39, 2001, pp. 35-59.

[49] W.M. Clearman, “Measurement and Correlation of Directional Permeability and Forchheimer’s Inertial Coefficient of Micro Porous Structures Used in Pulse-Tube Cryocoolers,” *Master’s Thesis*, Georgia Institute of Technology, Atlanta, Georgia 2007.

[50] M. Sözen, and K. Vafai, “Analysis of oscillating compressible flow through a packed bed,” *Int. J. Heat Fluid Flow*, vol. 12, 1991, pp.130-136.

[51] K. Nam, and S. Jeong, “Experimental study on the regenerator under actual operating conditions,” *Adv. Cryog. Eng.*, vol. 47, 2002, pp. 977–984.

[52] S. Jeong, K. Nam, and J. Jung, “Regenerator characterization under oscillating flow and pulsating pressure,” *Cryocoolers*, vol. 12, 2002, pp. 531–537.

[53] J.S. Cha, S.M. Ghiaaisiaan, P.V. Desai, J.P. Harvey, and C.S. Kirkconnell, “Multi-dimensional flow effects in pulse tube refrigerators,” *Cryogenics*, vol. 46, 2006, pp. 658–665.

[54] W.M. Clearman, J.S. Cha, S.M. Ghiaasiaan, and C.S. Kirkconnell, “Anisotropic steady-flow hydrodynamic parameters of microporous media applied to pulse tube and Stirling cryocooler regenerator,” *Cryogenics*, vol. 48, 2008, pp. 112–121.

[55] E.M. Sparrow, and V.B. Grannis, “Pressure drop characteristics of heat exchangers consisting of arrays of diamond-shaped pin fins,” *Int. J. Heat Mass Transfer*, vol. 34, 1996, pp. 589-600.

[56] J.S. Cha, S.M. Ghiaasiaan, and C.S. Kirkconnell, "Measurement of Anisotropic Hydrodynamic Parameters of Pulse Tube or Stirling Cryocooler Regenerators," 2006, pp. 1911.

[57] N. Sahiti, A. Lemouedda, D. Stojkovic, F. Durst, and E. Franz, “Performance comparison of pin fin in-duct flow arrays with various pin cross- sections,” *Appl. Therm. Eng.*, vol. 26, 2006, pp. 1176–1192.

[58] K.S. Raju, and A. Narasimhan, “Porous medium interconnector effects on the thermohydraulics of near-compact heat exchangers treated as porous media,” *ASME J. Heat Transfer*, vol. 129, 2007, pp. 273–281

[59] D. Missirlis, S. Donnerhack, O. Seite, C. Albanakis, A. Sideridis, K. Yakinthos, and A. Goulas, “Numerical development of a heat transfer and pressure drop porosity model for a heat exchanger for aero engine applications,” *Applied Thermal Engineering*, vol. 30, 2010, pp. 1341-1350.

[60] F. Pinson, O. Gregoire, M. Quintard, M. Prat, and O. Simonin, “Modeling of turbulent heat transfer and thermal dispersion for flows in flat plate heat exchangers,” *International Journal of Heat and Mass Transfer*, vol. 50, 2007, pp. 1500-1515.

[61] E. Carluccio, G. Starace, A. Ficarella, and D. Laforgia, “Numerical analysis of a cross-flow compact heat exchanger for vehicle applications,” *Applied Thermal Engineering,* vol. 25, 2005, pp. 1995-2013.

[62] U. Imke, “Porous media simplified simulation of single- and two-phase flow heat transfer in micro-channel heat exchangers,” *Chemical Engineering Journal*, vol. 101, 2004, pp. 295-302.

[63] P. Jiang, and Z. Ren, "Numerical investigation of forced convection heat transfer in porous media using a thermal non-equilibrium model," *International Journal of Heat and Fluid Flow,* vol. 22, 2001, pp. 102-110.

[64] N. Benarji, C. Balaji, and S. Venkateshan, "Unsteady fluid flow and heat transfer over a bank of flat tubes," *Heat and mass transfer*, vol. 44, 2008, pp. 445-461.

[65] Z. Guo, S. Kim, and H. Sung, "Pulsating flow and heat transfer in a pipe partially filled with a porous medium," *International Journal of Heat and Mass Transfer*, vol. 40, 1997, pp. 4209-4218.

[66] "Fluent 6 User Manual," ed: Fluent Inc., 2006.

[67] M.G. Pathak, T.I. Mulcahey, and S.M. Ghiaasiaan, "Oscillatory laminar flow physics in porous media under conjugate heat transfer conditions," 2012, submitted.

[68] D. Gedeon, Sage User's Guide, Gedeon Associates, 2009.

[69] Conrad, T.J., Landrum, E.C., Ghiaasiaan, S.M., Kirkconnell, C.S., Crittenden, and T.,Yorish, S., "CFD Modeling of Meso-Scale and Micro-Scale Pulse Tube Refrigerators," *Proceedings of Cryocoolers 15*, 2008.

[70] P. Nika, and Y. Bailly, "Comparison of two models of a double inlet miniature pulse tube refrigerator : Part A thermodynamics," *Cryogenics*, vol. 42, 2002, pp. 593-603.

[71] J. Gary, A.O. Gallagher, R. Radebaugh, Y. Huang, and E. Marquardt, "REGEN 3.3 User Manual," National Institute of Standards and Technology, Boulder, Colorado, 2008.

[72] W.C. Ward, and G.W. Swift, "Design Environment for Low Amplitude Thermoacoustic Engines," *J. Acoustic. Soc. Am*, vol. 95, 1994, pp. 3671.

[73] A. Kashani, and P. Roach, "A Simple Modeling Program for Orifice Pulse Tube Coolers," *Cryocooler 9*, 1997.

[74] A. Kashani, and P. Roach, "An Optimization Program for Modeling Pulse Tube Cryocoolers," *Advances in Cryogenics Engineering*, vol. 43, 1998, pp. 1903.

[75] Y.L. Ju, C. Wang, and Y. Zhou, “Numerical simulation and Experimental Verification of the Oscillating Flow in Pulse Tube refrigerator,” *Cryogenics*, vol. 38, 1998, pp. 169-176.

[76] R. Taylor, G. Nellis, and S. Klein, "Optimal Pulse-Tube Design Using Computational Fluid Dynamics," *Adv. in Cryogenic Engineering*, vol. 53, 2008, pp. 1445-1453.

[77] X. Zhang, L. Qiu, Z. Gan, and Y. He, "CFD study of a simple orifice pulse tube cooler," *Cryogenics*, 2007.

[78] B. Flake, and A. Razani, "Modeling pulse tube cryocoolers with CFD," *Adv. in Cryogenic Engineering*, vol. 49, 2004, pp. 1493-1499.

[79] I. Nachman, N. Pundak, and G. Grossman, "CFD Modeling of Reciprocating Flow around a Bend in Pulse Tube Cryocoolers," *Cryocoolers*, vol. 15, 2009, pp. 251-259.

[80] J.S. Cha, S.M. Ghiaasiaan, J.P. Harvey, P.V. Desai, and C.S. Kirkconnell, "CFD simulation of multi-dimensional effects in an Inertance tube pulse tube refrigerator," *Cryocoolers 13*, 2004, pp. 285-292.

[81] ANSYS(R) Fluent, Release 13.0, Fluent Theory Guide, 2011, ANSYS, Inc.

[82] J.S. Cha, S.M. Ghiaasiaan, and C.S. Kirkconnell, "Oscillatory flow in microporous media applied in pulse-tube and Stirling-cycle cryocooler regenerators," *Experimental Thermal and Fluid Science*, vol. 32, 2008, pp. 1264-1278.

[83] Pathak, Patel, Ghiaasiaan, Mulcahey, Helvensteijn, Kashani, and Feller, “Hydrodynamic parameters for ErPr under steady and periodic flow conditions,” 2013, submitted.

[84] K. Nam, and S. Jeong, "Novel flow analysis of regenerator under oscillating flow with pulsating pressure," *Cryogenics*, vol. 45, 2005, pp. 368-379.

[85] R. Sahoo, and S. Das, "Exergy maximization in cryogenic regenerators," *Cryogenics*, vol. 34, 1994, pp. 475-482.

[86] F.Z. Guo, Y.M. Chou, S.Z. Lee, Z.S. Wang, and W. Mao, "Flow characteristics of a cyclic flow regenerator," *Cryogenics*, vol. 27, 1987, pp. 152-155.

[87] H. Erk, and M. Dudukovic, "Phase-Change Heat Regenerators-Modeling and Experimental Studies (Vol 42, Pg 791, 1996)," *AIChE Journal*, vol. 43, 1997, pp. 1189-1189.

[88] K.V. Dobrego, N.N. Gnesdilov, I.M. Kozlov, V.I. Bubnovich, and H.A. Gonzalez, "Numerical investigation of the new regenerator-recuperator scheme of VOC oxidizer," *International Journal of Heat and Mass Transfer*, vol. 48, 2005, pp. 4695-4703.

[89] M. Ogawa, R. Li, and T. Hashimoto, "Thermal conductivities of magnetic intermetallic compounds for cryogenic regenerator," *Cryogenics*, vol. 30, 1990, pp. 521-526.

[90] A. Willmott, "Digital computer simulation of a thermal regenerator," *International Journal of Heat and Mass Transfer*, vol. 7, 1964, pp. 1291-1302.

[91] X. Hua and G. Zhong, "Analytical network model on the flow and thermal characteristics of cyclic flow cryogenic regenerators," *Cryogenics*, vol. 28, 1988, pp. 762-769.

[92] R. Radebaugh, A. O'Gallagher, and J. Gary, "Regenerator behavior at 4 K: Effect of volume and porosity," 2002, p. 961.

[93] A. De Waele, and J. Zeegers, "Counterflow pulse-tube refrigerators," 2002, p. 617.

[94] H. Yuan, and L. Jing-Tao, "The effect of the regenerator and tube volume on the performance of a high frequency miniature pulse tube refrigerator," *Journal of Engineering Thermophysics*, 2002.

[95] R. Radebaugh, Y. Huang, A. O'Gallagher, and J. Gary, "Calculated Performance of Low-Porosity Regenerators at 4 K with He-4 and He-3," *Cryocoolers 15*, 2009, pp. 325-334.

[96] T.W. Wysokinski, J.A. Barclay, K.A. Gschneidner Jr., V.K. Pecharsky, A.O. Pecharsky, "Comparative evaluation of erbium and lead regenerator materials for low temperature crycoolers," *Cryogenics*, vol. 42, 2002, pp.463-467.

[97] E. Landrum, T. Conrad, S.M. Ghiaasiaan, and C.S. Kirkconnell, "Hydrodynamic Parameters of Mesh Fillers Relevant to Miniature Regenerative Cryocoolers," *Cryogenics*, vol. 50, 2009, pp. 373-380.

[98] Fluent Inc. 2003. Gambit User Manual.

[99] T.R. Ashwin, G.S.V.L. Narasimham, and S. Jacob, "Oscillatory flow and temperature fields in an open tube with temperature difference across the ends," *International Journal of Heat and Mass Transfer*, vol. 54, 2011, pp. 3357-3368.

[100] MATLAB(R) 7.8.0 (R2009a), The MathWorks, Natick, MA.

VITA

MIHIR G. PATHAK

PATHAK was born in Newark, Delaware and graduated from Kennett High School in Kennett Square, Pennsylvania. He moved to Atlanta in August 2005 to attend Georgia Tech and graduated with highest honors (*Summa Cum Laude*) in 3.5 years with a B.S. degree in Mechanical Engineering in December 2008. As a member of the Woodruff School B.S./M.S. program, he completed his M.S. in Mechanical Engineering under the advisement of Dr. S. Mostafa Ghiaasiaan in August 2010 with his thesis titled, "*Thermal Dispersion and Convective Heat Transfer during Laminar Pulsating Flow in Porous Media*". He completed his doctoral studies by August 2013, earning a Ph.D. in Mechanical Engineering under the advisement of Dr. S. Mostafa Ghiaasiaan while completing a minor in economics and finance under the guidance of Dr. Thomas "Danny" Boston. His dissertation title was, "*Periodic Flow Physics in Porous Media of Regenerative Cryocoolers*".

While a student, Pathak was heavily involved in several leadership positions on campus. He was part of the Graduate Student College of Engineering Advisory Council, Student Government Association, Senate and House of Representatives, Mechanical Engineering Graduate Student Association, Woodruff School Student Advisory Board, Pi Tau Sigma academic honor society, Order of Omega Greek honor society, Omicron Delta Kappa leadership honor society, Sigma Beta Rho Multicultural Fraternity, Global Leadership Conference, President's Council Governing Board, Georgia Tech Emerging Leaders, and several department wide and institute wide committees. He is a member of

the American Society of Mechanical Engineers, Cryogenic Society of America, Georgia Tech Student Alumni Association, Sigma Beta Rho Alumni Association, Institute of Industrial Engineers, and American Association of Physicists in Medicine. Along with leadership, Pathak served in countless service activities performing over 100 hours of community service, mentoring a number of high school, undergraduate, and graduate students, and earning the President's Gold Award for Community Service. Pathak also has researched in the Bio-Inspired Design Lab at Georgia Tech, Direct Digital Manufacturing Lab at Georgia Tech, and Nuclear Medicine/Medical Physics Lab at Emory University School of Medicine, while teaching thermal energy fluids lab, convection heat transfer, thermal fluids engineering, system dynamics and controls, and heat transfer.

Pathak's experiences are vast and diverse. He has served as a visiting fellow/scientist at the NASA/Caltech Jet Propulsion Lab, visiting fellow/scientist at the NASA Ames Research Center, visiting fellow/scientist at the NASA Goddard Space Flight Center, strategist and board member at EuQuant, president and co-founder of Mechistry Technologies, LLC, and participant in the Engineering & Science Insight Program at McKinsey & Company. Pathak has won several prestigious awards as well including the Presidential Management Fellowship (Finalist), NASA Space Technology Research Fellowship, Georgia Tech Presidential Fellowship, George W. Woodruff Presidential Fellowship, National Science Foundation Graduate Student Research Fellowship (Honorable Mention), Sandia National Laboratory Master's Fellowship (declined), Georgia Tech Pi Tau Sigma Outstanding Senior Award (Runner Up), along

with the George W. Woodruff School of Mechanical Engineering, Sidney Goldin, Grace & Ewell Barnes, and H & M Bourne scholarships.

Pathak has published, presented, or submitted several papers including:

1. Pathak, Patel, Ghiaasiaan, Mulcahey, Helvensteijn, Kashani, and Feller, Hydrodynamic parameters for ErPr under steady and periodic flow conditions, 2013 (submitted)
2. Pathak, Mulcahey, and Ghiaasiaan, Conjugate Heat Transfer during Oscillatory Laminar Flow in Porous Media, 2012, (submitted)
3. Pathak, Patel, Ghiaasiaan, Mulcahey, Helvensteijn, Kashani, and Feller, Hydrodynamic resistance parameters for ErPr rare-Earth regenerator material under steady and periodic flow conditions, Adv. in Cryogenic Eng., 2013 (submitted)
4. Mulcahey, Conrad, Ghiaasiaan, and Pathak, Investigation of gravitational effects in pulse tube cryocoolers using 3-D CFD, Adv. in Cryogenic Eng., 2013 (submitted)
5. Pathak, Ghiaasiaan, Radebaugh, Kashani, and Feller, The Design and Development of a High-Capacity Cryocooler Regenerator for Space Exploration, AIAA Space Conference, 2012
6. Mulcahey, Pathak, and Ghiaasiaan, The effect of flow pulsation on drag and heat transfer in an array of heated square cylinders, Int. J. of Thermal Science, 2012
7. Mulcahey, Pathak, and Ghiaasiaan, Drag coefficient and Nusselt number for laminar pulsating flow in porous media, *Cryocoolers 17*, 2012.

8. Pathak, Mulcahey, and Ghiaasiaan, Hydrodynamic and thermal effects of drag and heat transfer coefficients under laminar unsteady flow conditions in porous media, Advances in Cryogenic Eng., 2011
9. Conrad, Pathak, Ghiaasiaan, and Kirkconnell, The Effect of Component Junction Tapering on Miniature Cryocooler Performance, Advances in Cryogenic Eng., 2011
10. Pathak and Ghiaasiaan, Thermal Dispersion and Convective Heat Transfer during Laminar Pulsating Flow, Int.l J. of Thermal Science, 2010
11. Pathak, Thermal Dispersion and Convective Heat Transfer during Laminar Pulsating Flow, Master's Thesis, Georgia Institute of Technology, Atlanta, GA, 2010
12. Pathak and Ghiaasiaan, Thermal Dispersion and Convection Heat Transfer during Laminar Pulsating Flow, Cryocoolers 16, 2010
13. Landrum, Conrad, Pathak, Ghiaasiaan, Kirkconnell, Crittenden, Yorish, Effect of Frequency on Hydrodynamic Parameters of Mesh Fillers in Oscillatory Flow, Cryocoolers 16, 2010

He also holds a patent application for "*Domestic Lifting Dolly , U.S. 61/192,305, 2008"* and served as a technical reviewer for Engineering Applications of Computational Fluid Mechanics, International Journal of Thermal Science, Advances in Cryogenic Engineering, Cryocoolers, and International Journal of Heat and Mass Transfer.

In his spare time, Pathak enjoys sports, traveling, and spending time with his wife, family, and friends.